Development of Highly Efficient Catalysts for Acetylene Semi-hydrogenation Based on Multinary Non-Noble Alloys

(アセチレン部分水素化に有効な卑金属多元素合金触媒の開発)

馬 嘉敏

Jiamin Ma

Graduate School of Chemical Sciences and Engineering

Hokkaido University

2023

Contents

Chapter One

General Introduction

1. General Introduction

1.1 Research status of acetylene semi-hydrogenation

Ethylene is the basis for the production of plastics in the chemical industry as it is a key polymerization raw material and reaction intermediate in the production of chemicals. Ethylene can undergo a series of chemical reactions such as polymerization, oxidation, alkylation, dentition, hydration and polymerization, the most important of which is the polymerization of polyethylene. Polyethylene is a highly valued industrial product and is used in a wide range of applications in all areas of life. 97% of ethylene is produced by naphtha cracking in the petroleum industry process (light hydrocarbons from natural gas processing plants, such as ethane, as well as processed products and secondary processed oil from refineries, such as naphtha and hydrocracking gasoline) while the others are obtained by other process like methanol to olefins. In the cracking process, a trace amount of unavoidable acetylene is one of the most significant impurities, which is poisonous to the polymerization catalysts (Ziegler-Natta catalysts),[1,2]leading to a sharp decrease of the eventual quality of polyethylene. What's more, it tends to produce explosive oligomers that pose a threat to the safety of the downstream reaction systems.[3,4] Therefore, it's of great importance to diminish the concentration of acetylene to at least 5 ppm.[5]

There are several types of methods for ethylene purification, among which the most commercial method is the selective catalytic semi-hydrogenation of acetylene. This method has many advantages, such as low energy consumption, low pollution, simple operation and so on.[6] Figure 1.1 summarized the reaction schemes of acetylene semi-hydrogenation. In addition to the generation of the target product ethylene (step 1), there are also several side reactions. Hydrogenation of acetylene or ethylene to ethane (steps 2 and 3) reduces ethylene selectivity. Polymerization reactions produce long chain olefins and eventually form green oil (steps 4-6), which covers the active site of the catalyst and results in catalyst deactivation.[7]

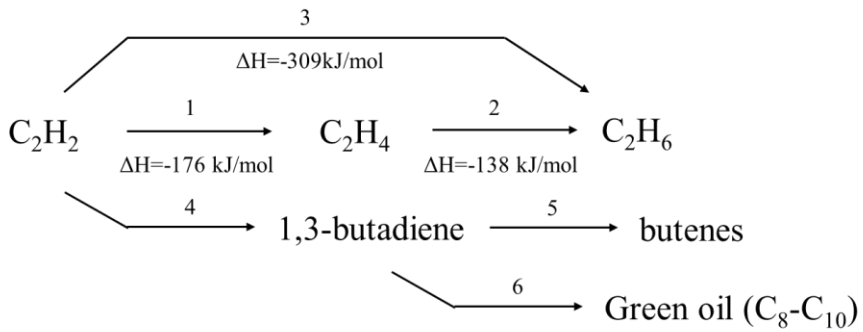

Figure 1.1. Reaction network of acetylene hydrogenation.

1.2 Noble metal catalysts for acetylene semi-hydrogenation

In industry, catalysts for the acetylene semi-hydrogenation reaction must be highly active because the concentration of acetylene in the feed gas is extremely low. Meanwhile, it is also important to prevent further hydrogenation of ethylene to ethane from product as well as from the original ethylene in the feed gas. This means that catalysts for acetylene semi-hydrogenation must also be highly selective.

As early as 1945, J. Sheridan reported that Pd demonstrated higher potential for acetylene semi-hydrogenation than Ni, Pt, Rh and Ir at low reaction temperatures.[8] From then on, researchers focused on tuning the structure of Pd-based catalysts to achieve high ethylene selectivity. It is possible to inhibit over-hydrogenation by poisoning some active sites on the Pd -based catalysts. For example, a very famous Lindlar catalyst ($Pd/CaCO_3$) was invented in 1952.[9] This catalyst was made from palladium adsorbed on a support (calcium carbonate or barium sulphate) with a small amount of inhibitor (lead acetate or quinoline). However, the lead salt was harmful to human health and caused environmental pollution. In 1957, L.K. Frevel found that the addition of Group IB metals to palladium increased the selectivity towards ethylene. This was the first paper reported Pd-Ag alloy.[10] Subsequently, a number of researchers paid attention to alloy Pd with group IB transition metals for semi-hydrogenation of acetylene. In 1958, G.C.Bond carried out a series of catalysts and summarized that their selectivity fell in the order Pd > Rh > Pt. Besides, Pd and Ag mixtures supported on Al_2O_3 showed higher initial selectivity than pure Pd while remained high activity.[11] Pd-Au alloys increased the activity in acetylene semi-hydrogenation.[11] The addition of Cu improved the stability but reduced catalytic activity. As a result, both the overall rate of C_2H_6 formation and the selectivity of C_{4+} both significantly decreased.[12] In 1985, Boitiaux, J.P. made a conclusion that the transfer of electrons from group IB transition metals to Pd was assumed to be the reason for the observed improvement in selectivity and reaction rate with addition of these metals.[13] In recent years, the doping of Pd with a second metal has been widely used in acetylene semi-hydrogenation reactions. Scientists have focused on investigating the effect of adjusting the catalyst structure on the modulation of catalytic performance. Pachulski et al. prepared Pd-Ag/Al_2O_3 catalysts with different Pd/Ag ratios and tested the catalytic performance of the catalysts for the selective hydrogenation of acetylene. The results showed that the Pd-Ag catalysts significantly inhibited the formation of green oil when the Ag/Pd ratio in the catalysts was 0.41, thus maintaining a high stability and the low concentration of Ag showed a higher stability than the high concentration of Ag.[13] Series of Au–Pd/SiO_2 bimetallic catalysts with

Au coverages ranging from 0.2 to 0.9 on the Pd surface were used for acetylene semi-hydrogenation. The results indicated that at higher Au coverage, smaller Pd aggregates were formed on the catalyst surface, where the stable adsorption configuration of acetylene was π-configuration, leading to the easy formation and desorption of ethylene, thus improving the selectivity of ethylene. On the contrary, at lower Au coverage, the Pd aggregates were larger and resembled the pure Pd surface. In this case, acetylene was strongly adsorbed on the catalyst surface in the σ-configuration so it was easily over-hydrogenated to ethane, thus reducing the ethylene selectivity.[13] Tao Zhang's group succeeded in synthesizing silica gel supported Cu-alloyed Pd SAC, over which 85% ethylene selectivity could be achieved at full acetylene conversion. The Cu-modified Pd monatomic catalysts showed the highest acetylene conversion and ethylene selectivity compared to the Au and Ag-modified Pd-based catalysts. The Cu-modified Pd catalysts significantly reduced the adsorption of ethylene on the surface, which facilitated the ethylene selectivity. Besides, the hydrogen adsorption was significantly higher than that of the pure Pd catalysts, which in turn promoted the activation of hydrogen dissociation.[13] intermetallic PdNi catalysts were prepared by various methods including co-impregnation, sol-immobilization method and LDH precursor method. The PdNi alloy catalysts synthesized by the LDH precursors method exhibited higher catalytic activity and ethylene selectivity due to smaller particle size and stronger metal-to-metal interactions, and the PdNi alloy catalysts showed better stability.[13] The catalytic activity of PdGa and Pd_3Ga_7 intermetallic compounds increased, which were assigned to the partial dissolving of surface gallium oxides. The low surface area of the conventional catalysts can be overcome by chemical etching. Even though the catalytic activity can be increased, the catalytic selectivity was decreased due to the partial destruction of crystal structure of the intermetallic compounds.[14] Another type of promising metal, alkali metals, have also been demonstrated to be promoters for acetylene semi-hydrogenation. The enhanced effect of K for Pd catalysts on the selective hydrogenation of C_2H_2 in C_2H_4 was reported by Park.Y.H in 1991.[15] Later, this group also designed some experiments to investigate the promotion effects of K on Pd/Al_2O_3 catalyst. It was found that the addition of K accelerated the conversion of acetylene and the partial hydrogenation of acetylene to ethylene while at the same time, increased the generation of oligomers. The possibility of ethylene desorption increased with the increasing of K. In contrast to the increased rate of acetylene hydrogenation, the rate of ethylene deuteration was found to decreased with K addition. All of these effects could be attributed to a weakening of hydrocarbon adsorption resulting by K due to metal-support interactions.[16] Sang H Moon's group used Si to modify Pd catalysts and obtained higher selectivity to ethylene

compared to pure Pd catalysts. In the meantime, the amount of green oil also decreased. The experimental results showed that the geometric modification of Pd by Si played a vital role in improving catalytic performance.[17] Thus, generally speaking, the role of the promoters was summarized to geometrical and electrical effects. The promoter on the Pd surface decreased the amount of the multiple Pd sites which was highly related to the reduced selectivity. This was the so-called "geometric modification". The addition of promoter can also alter the surface electrons of Pd, resulting in the modification of adsorption strength between Pd and the adsorbate. This was the so called "electrical modification".

In addition to the addition of metal to the catalysts, elemental substitution also allowed the precise tailoring of the catalytic properties to the target reaction. For example, just recent year, pseudo binary alloys were used for the first time for acetylene semi-hydrogenation, as reported by Armbruster et al. Comparable to binary $GaPd_2$, the solid solution $Ga_{1-x}Sn_xPd_2$ exhibited excellent selectivity towards ethylene (~85%). The highest catalytic activity can be obtained when the x value was optimized to 0.28.[18]

In short, the over-hydrogenation of acetylene and ethylene can be inhibited to some extent by introducing the second metal into the Pd catalysts, but the ethylene selectivity was still unsatisfactory. In addition, the introduction of the second metal may also reduce the catalytic activity and promote the formation of green oil, thereby reducing the stability of the catalysts.

1.3 Non-noble metal catalysts

Noble metal catalysts have been widely used in the acetylene hydrogenation reaction. However, the high activity of noble metals results in low selectivity for ethylene and carbon deposition. Alternatively, noble metals are scarce, expensive and environmentally unfriendly. Therefore, it's essential to focus on the search for non-noble metal alternative catalysts. There are many kinds of non-noble metal catalysts such as Ni-based catalysts, Cu-based catalysts, Fe-based catalysts, Co-based catalysts, In_2O_3, CeO_2, TiO_2, graphene and so on.

1.3.1 Research status of non-noble metal catalysts

Recently, the abundant and inexpensive non-noble metal Ni has exhibited great potential to be an alternative of noble metal for acetylene semi-hydrogenation due to its low dissociation energy barrier to H_2 because it has unfilled d electron orbitals.[19–21] Ni-based materials have been used for acetylene semi-hydrogenation but there have been a significant challenges in

developing Ni-based catalysts due to the much lower activity of Ni than Pd and the difficulty in preventing the over-hydrogenation of ethylene at near complete acetylene conversions. Besides, Ni-based catalysts were unstable and was often accompanied by carbon deposition and green oil formation, which limited their industrial applications. The addition of promoters is particularly important for Ni catalysts to achieve better performance and be potential candidates for Pd-based catalysts. Studt et al. screened the catalytic performance of more than 70 metal alloys and intermetallic compounds based on the relationship between the heats of adsorption for acetylene and ethylene on the same metal surface against that of methyl groups (CH_3-). It's found that the Ni-Zn non-noble metal catalyst has the best catalytic performance owing to weaker adsorption of ethylene.[22] (Figure 1.2) In fact, as early as the 1990s, Rodríguez et al. found that the NiZn alloy had good acetylene selective hydrogenation properties, on which the amount of coking and methane was reduced.[23] A more detailed reaction mechanism was proposed that the addition of Zn was responsible for reducing the development of oligomers to improve the selectivity of ethylene. There was little correlation between ethane production and the Zn content. According to the DFT results, the improvement in ethylene selectivity was ascribed to the lower acetylene adsorption energy of intermetallic NiZn compared to pure Ni.[21] Similarly, Chen et al prepared NiGa/SiO_2 bimetallic catalysts by introducing the main group metal element Ga into the monometallic Ni catalysts. The results showed that there were electron interactions between these two metals, resulting in the transfer of electrons from Ga to Ni. Thus, the increase of the electron cloud density weakened the adsorption strength of ethylene at the active Ni site, leading to rapid desorption of ethylene from the active Ni site, which contributed to better ethylene selectivity than the monometallic Ni/SiO_2 catalyst.[24] Further, Hu et al that the strong acetylene absorption on the monometallic Ni surface was weakened when different metals such as Au, Ag and Cu were introduced into the Ni-based catalysts. This indicated that the introduction of a second metal made C_2H_4 more prone to desorption rather than over-hydrogenation, thus improving the ethylene selectivity.[19] Moreover, the isolation of Ni sites by Mo and S to form Ni single-atom sites was other revealed to be effective in acetylene semi-hydrogenation. A heterolytic route over Ni_1MoS/Al_2O_3 played a role in the activation of H_2 molecules to enhance the reaction rate. The unique isolated $Ni^{\delta+}$ structure induced by Mo and S facilitated product desorption. The feasible way to construct isolated sites provides new ideas for fabricating an effective catalyst.

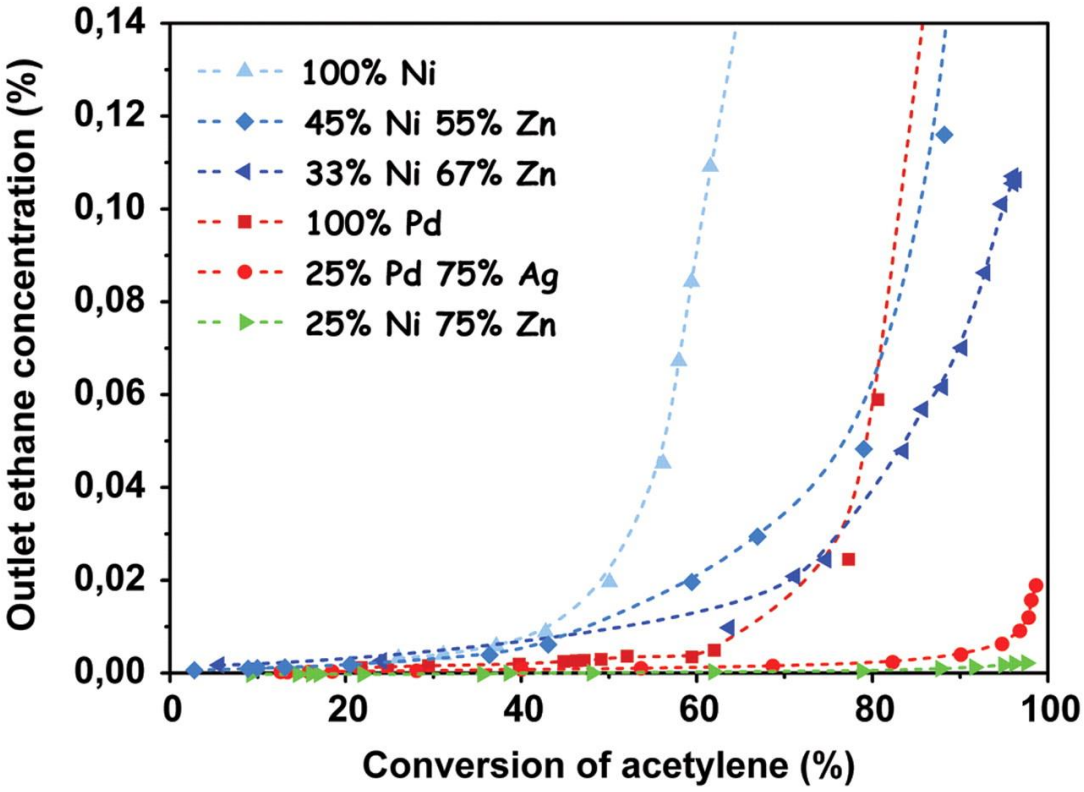

Figure 1.2. Conversion measured the concentration of ethane at the reactor outlet as a function of acetylene conversion for seven catalysts. Ethane production is a measure of the selectivity of acetylene hydrogenation, and zero ethane corresponds to the most selective catalyst. At the reactor inlet, the gas contained 1.33% ethylene, 0.0667% acetylene, and 0.67% hydrogen, with the remainder made up of Ar and N_2 in a total pressure of 1 bar. Reproduced from ref.[22]with permission. Copyright© 2008 American Association for the Advancement of Science.

Cu-based catalysts have been frequently used in the acetylene semi-hydrogenation reaction due to their high selectivity originating from unique electronic property of Cu with full 3d and half-empty 4s orbitals. Lots of studies have shown that Cu-based catalysts can be served as the main active component for the selective hydrogenation of acetylene and exhibit high ethylene selectivity and catalytic activity at higher operating temperatures (>200°C). Nevertheless, catalyst poisoning and deactivation were still unavoidable due to the easy formation of green oil on catalysts. Hence, researchers are often engaged in modifying the catalytic performance of Cu-based catalysts for the selective hydrogenation of acetylene. Lu's group found that with decreasing Cu particle size, both the ethylene selectivity and durability improved significantly gradually. (Figure 1.3) In particular, the highest ethylene selectivity (91%) even at full acetylene conversion can be observed on the Cu SAC along with outstanding long-term stability of at least 40 h. Thus, modulation of the metal particle size will alter both

the morphology and the electronic property of the metal, significantly modifying its catalytic performance.[25] The Pd/Cu single-atom alloy was successfully fabricated by kyriakou et al. by depositing Pd on a bare Cu (111) surface. Experiments and DFT calculations results showed that the energy barrier for hydrogen absorption taken on the Cu metal surface and subsequent desorption was significantly lowered by isolated Pd atoms. Thus, this facile hydrogen dissociation at the Pd atom site and weak Cu binding resulted in the selective hydrogenation of acetylene.[26] Although the introduction of Pd into Cu catalysts has improved the catalytic activity of Cu-based catalysts at low temperature, the use of the noble metal Pd is inevitable. Therefore, it is important to develop Cu-based catalysts for the selective hydrogenation of acetylene without the introduction of noble metals.

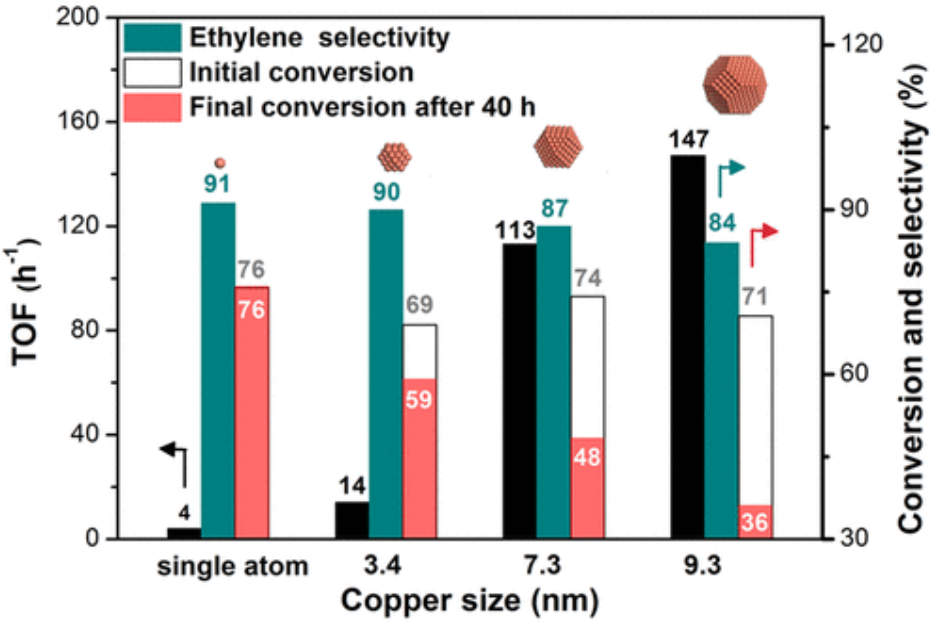

Figure 1.3. TOF, acetylene conversion and ethylene selectivity as a function of copper size. Reproduced from ref.[25] with permission. Copyright© 2020 American Chemical Society.

Aside from Ni and Cu, another 3d transition metal Co was also applied for the acetylene semi-hydrogenation reaction. A series of Co-based catalysts such as CoGa, CoSn and CoAl have been investigated for acetylene semi-hydrogenation. After reduction, the intermetallic phase can be observed over CoGe, $COGe_2$ and CoSn while only Co was presented over CoAl. Higher ethylene selectivity can be achieved over intermetallic compounds while pure Co catalyzed the complete hydrogenation to ethane. The dissociative adsorption of H_2 was suppressed owing to strong ethylene adsorption on CoGe surface, thus further hydrogenation of ethylene can be inhibited. Apart from the binary alloy, a catalysis-tunable heusler alloys was

reported for the first time in the acetylene semi-hydrogenation reaction. $Co_2Mn_xFe_{1-x}Ge$ derived from substation of Co_2MnGe and Co_2FeGe alloys showed high ethylene selectivity even at a 100% acetylene conversion. The Mn-Fe substitution accurately controlled the electronic structure (ligand effect) while Ga substitution for Ge in $Co_2FeGa_yGe_{1-y}$ was an ensemble effect. That is to say, heusler alloys can separately use the ensemble and ligand effects according to the targeted purpose.[27] (Figure 1.4) As for Fe-based catalysts, an $Al_{13}Fe_4$ intermetallic compound synthesized by the melt method was identified to be highly active and selective for the production of ethylene, which was attributed to the combination of site-isolation and the alteration of the electronic structure by the chemical bonding.

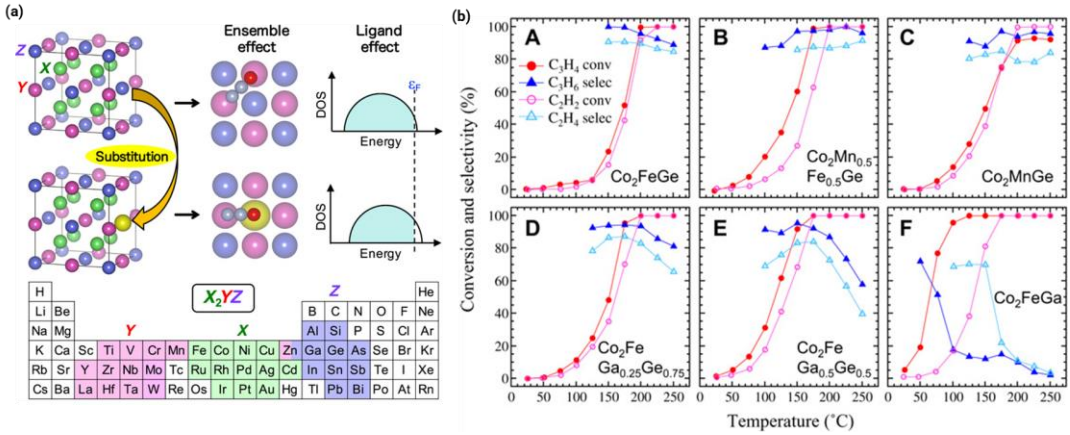

Figure 1.4. (a) Concept of this study. Effects of elemental substitution are schematically illustrated with the Heusler alloy's crystal structure ($L2_1$-type X_2YZ). Periodic table represents typical elements consisting of *X*, *Y*, and *Z* (color painted). Other elements such as lanthanoids and those in groups 1 and 2 are also possible components of Heusler alloys. (b) Results of alkyne hydrogenation in the presence of alkene. Alkyne conversions (circles) and alkene selectivity (triangles) for (A) Co_2FeGe, (B) $Co_2Mn_{0.5}Fe_{0.5}Ge$, (C) Co_2MnGe, (D) $Co_2FeGa_{0.25}Ge_{0.75}$, (E) $Co_2FeGa_{0.5}Ge_{0.5}$, and (F) Co_2FeGa. Closed and open symbols represent results for hydrogenations of C_3H_4 in C_3H_6 and C_2H_2 in C_2H_4, respectively. Reactants were [0.1% alkynes/10% alkenes/40% H_2/He balance]. Selectivity in low-conversion regions are not shown due to large errors. Reproduced from ref.[26] with permission. Copyright© 2018 American Association for the Advancement of Science.

Due to their ability to active hydrogen molecules, metal catalysts can not only be used as supports but also somewhile be utilized as catalysts for hydrogenations. As exemplified by CeO_2, high ethylene selectivity has been achieved on polycrystalline ceria. The excellent

performance of CeO_2 highly depended on its ability to stabilize highly reactive β-C_2H_2 radicals on the (111) surface by easily accommodating an electron in Ce 4f states.[28] In_2O_3 was confirmed as a novel catalyst for acetylene semi-hydrogenation, which exhibited 85% ethylene selectivity at 100% conversion even in ethylene excess. The well-defined vacancies and surrounding In_3O_5 ensembles were regarded as the key factor for this outstanding catalytic function.[29] DFT calculations demonstrated that anatase TiO_2 with oxygen vacancies (Ovs) can effectively hydrogenate acetylene to ethylene because it provided frustrated Lewis pairs (FLPs) from surface Ti and O atoms for the heterolytic dissociation of hydrogen.[30]

1.3.2 Modification of geometric and/or electronic structure of active centers

The catalytic active centers are the specific sites in a catalytic reaction that activate the reactant molecules and facilitate the progress of the reaction to proceed smoothly. Atoms, atomic groups, ions or surface defects can play the role of catalytic active centers. The structure of the active center has a crucial influence on the catalytic performance.[31–33] By tuning the catalytic performance by modulating the geometry and electronic structure of the active centers, the intrinsic link between the structure of the active centers and the catalytic performance can be more clearly revealed, which is of great significance for the elucidating the catalytic mechanism and the synergistic enhancement of catalytic activity, selectivity and stability. Thus, researchers around the world have made great effort to study on the geometry and electronic structure of catalytic active centers and have developed a number of methods to regulate the structure of catalytic active centers, which provided a wide range of ideas for the further development of efficient catalysts. In this section, strategies for modifying the geometric and/or electronic structure active sites are mainly classified into three categories: (1) the addition of other components; (2) site-isolation strategy; (3) other strategies. By doing these, a continuous arrangement of active metal sites can be achieved. The geometry and electronic of the catalytic active center can be adjusted to achieve an effective segregation of continuously arranged active metal sites, which changed the mode of reactant and product adsorption and activation, to enhance catalytic activity, selectivity, and stability.

1.3.2.1 Addition of other components

Modulation of catalyst performance by the addition of a second or third or even more metal component is widely applied in heterogeneous catalysis. However, the role of the second

component was not clear in the early studies, which was initially described as a co-catalyst to improve the dispersion, mechanical strength and thermal stability of the catalysts. With the development of catalytic characterization tools, the knowledge of catalyst structures and the establishment of “structure-catalytic performance” relationships, the effect of these additive components on catalytic performance became clearer and provided a basis for the subsequent design of efficient catalysts. In acetylene semi-hydrogenation reaction, a variety of catalyst structures have been designed and prepared based on the geometric and electronic effects to regulate their catalytic performance, and significant progress has been made in establishing the corresponding "structure-catalytic performance" relationships.

Ni has a high acetylene adsorption energy, which leads to the coverage of C2 species in the active sites, which in turn leads to the formation of C-C bonds and the generation of side reactions. In addition, acetylene adsorbed on three nickel atoms can dissociate to form ethylenediamine, and then formed ethane and carbon, ultimately leading to a reduction in catalyst selectivity and activity.[34] Recently, a large number of studies have been carried out to address these drawbacks of Ni-based catalysts. A common approach is to introduce a second metal to form intermetallic compounds. In this way, on the one hand, the electronic and geometric structures of the main active metal can be changed, which remarkably improved the catalytic performance. On the other hand, a specific highly ordered arrangement of atoms affects the adsorption conformation and surface dynamics, accounting for high selectivity. For example, higher ethylene selectivity was realized on Ni_3Ge catalyst due to facilitated geometric and electronic effects coming from intermetallic compounds.[35] Another similar example, $NiCu/CeO_2$ catalysts accelerated the desorption of ethylene and weakened the adsorption of intermediates which originated from electronic and geometric modification of Ni sites by Cu atoms.[35] Li’s group synthesized a homogenously distributed NiCu catalyst which improved selectivity and inhibited coking comparing with mono Ni catalyst. The reason was ascribed to electron transfer from Cu to Ni.[36] There are too many such examples for me to outline here.

The type of the second metal species in the intermetallic compound affected the geometry and electronic structure of the catalysts, which subsequently modulates the catalytic performance of the catalyst. For example, Song et al investigated the catalytic performance of intermetallic compounds Ni_1M_1(M=B, Al, Ga, In, Tl) for the acetylene semi-hydrogenation reaction. The results suggested that the metal species M affected the electronic structure of the catalysts which in turn affected the semi-hydrogenation activity.[37] (Figure 1.5)

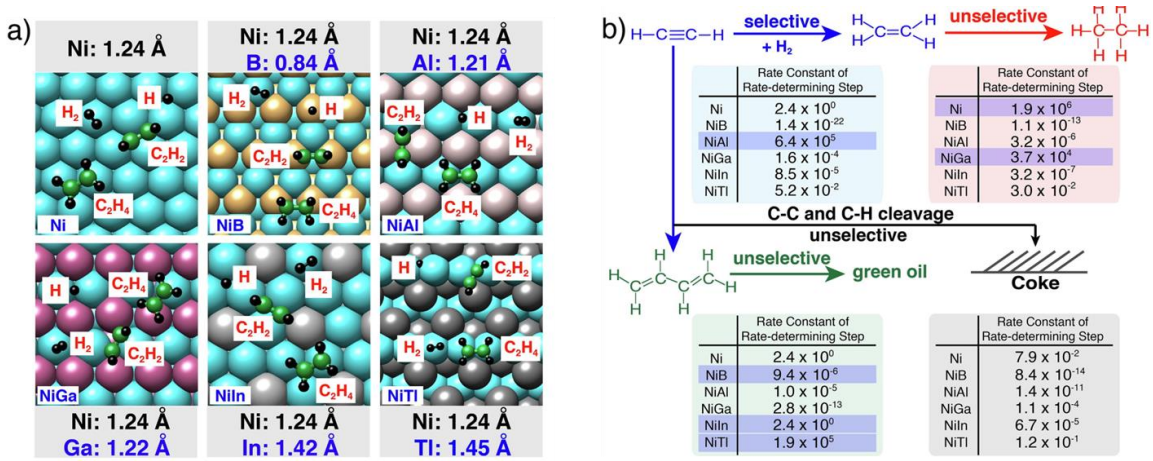

Figure 1.5. (a) illustrative model surfaces with acetylene, ethylene, molecular H_2, and atomic H adsorbed over Ni and Ni + B-group IMCs; (b) Rate constants for each reaction pathway in semi-hydrogenation of acetylene. Elements in the model figures are color coded: Ni (light blue), B (yellow), Al (light gray), Ga (magenta), In (medium gray), Tl (dark gray), C (green) and H (black). Reproduced from ref.[37] with permission. Copyright© 2008 Elsevier.

Different ratios of the second metal in intermetallic compounds lead to different, which can affect the catalytic performance of the reaction. Rao et al theoretically investigated the catalytic performance of Ni_nGa (n=1, 3) intermetallic compounds for acetylene semi-hydrogenation and found that the Ga-rich NiGa intermetallic compounds had the highest hydrogenation activity and C_2H_4 selectivity.[38] A series of bimetallic Ni_xIn/SiO_2 catalysts with various Ni/In ratios were evaluated. Ni_xIn/SiO_2 with a suitable Ni/In ratio provided much higher acetylene conversion, ethylene selectivity, and catalyst stability than Ni/SiO_2 because the charge transfer from the inert In atoms to the active Ni atoms and the geometrical isolation of the active Ni atoms with the inert In atoms. Both of them were beneficial for reducing the adsorption strength of ethylene and preventing the C-C hydrogenolysis and the polymerizations of acetylene and the intermediates.[39]

Apart from introducing a second metal to form intermetallic compounds, incorporating light elements into the lattice of the active metal is also a proven method to effectively tune the catalytic performance.[40,41] As demonstrated by Zhang's group, carbon was incorporated into the Ni_3Zn lattice. A remarkable improvement in selectivity and stability can be observed over the $Ni_3ZnC_{0.7}$ catalyst. This was because the introduction of carbon suppressed the undesired side reaction as well as regulated the electronic structure of Ni.[42] (Figure 1.6) A similar result presented by another group was carbon tailored NiGa intermetallic catalyst for acetylene semi-hydrogenation. Compared with Ni and Ni_3Ga, $Ni_3GaC_{0.5}$ exhibited higher ethylene selectivity

because ethylene tends to desorb rather than over hydrogenate. Besides, it's also pointed out that the formation of C4 products can be inhibited over $Ni_3GaC_{0.5}$, leading to the superior stability.[43]

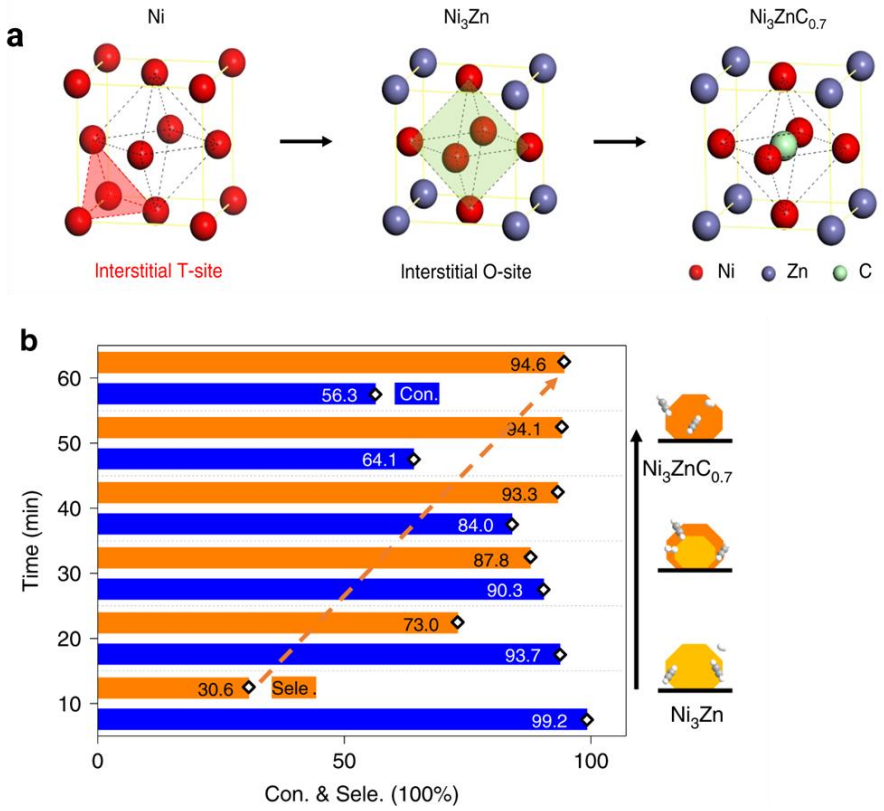

Figure 1.6. (a) Schematic of expanded interstitial sites in the unit cells of Ni, Ni_3Zn, and $Ni_3ZnC_{0.7}$. The red and black dash lines indicate the tetragonal and octahedral interstitial sites. (b) The reactivity corresponds to the structural evolution of Ni_3Zn/oCNT catalyst under reaction conditions. Reproduced from ref.[42] with permission. Copyright© 2020 Nature.

As the research evolved, researchers even added a third or fourth metal to tune the structure of the catalysts to achieve their stated goal. In 2001, J.C. Rodriguez et demonstrated that the formation of Ni-Cu and Ni-Co over the quaternary Ni (Co, Cu)-Zn-Al catalyst made great contributions to higher selectivity by inhibiting undesirable methane and ethane. Despite this, the ethylene selectivity was limited to a maximum of 40% at a lower acetylene conversion (14%).[44] Faced with the challenge of inhibiting over-hydrogenation and oligomerization, Javier Pérez-Ramírez reported a ternary Cu-Ni-Fe catalysts, in which, the H_2 coverage was increased by Ni, Fe played the role of structural promoter and Cu was the basic hydrogenation metal. The synergistic effect was responsible for acceleration of ethylene selectivity. It's worth mentioning that there is no need to add CO as promoter and high selectivity towards ethylene

can be realized at a board H_2/alkyne ratio operation window.[34] Furthermore, a novel type of alloy, heusler alloys was proposed for the first time to control the catalytic properties for acetylene semi-hydrogenation by partially element substitution. Precise tuning of the catalytic performance was realized due to the arbitrary adjustment of heusler alloys. As a consequence, even at full acetylene conversion and a very high H_2/alkyne ratio of 400, $Co_2Mn_xFe_{1-x}Ge$ catalysts remained high ethylene selectivity, which resulted from the accurately controlled electronic structure. Undoubtedly, heusler alloys provided a fine-tuning platform to reveal the fundamental principles catalysis behind intermetallics.[27]

Based on what I stated above, we can conclude that incorporating a second metal can modulate the catalyst structure to adjust the catalytic performance precisely.

1.3.2.2 Site-isolation strategy

Conventional wisdom has it that isolating the contiguous active sites is an effective way to break through the occurrence of ensemble sites, preventing ethylene from over-hydrogenation.[18,45,46] This is the so-called "site-isolation strategy" and the basic principle is to suppress the di/multi-σ bond adsorption configurations for molecular species. For this purpose, some inert metal is often employed to alloy with active metal to allow site-isolation. In this way, the goal of increasing ethylene selectivity can be achieved.

Intermetallic compounds with highly ordered atomic arrangements and unique electronic properties, offer opportunities to manipulate the active sites through precise control at the atomic level. Accordingly, a large number of works were focused on the introduction of another inert metal to form intermetallic structures that endowed the catalysts with isolated sites.[47,48] As presented in the previous study, where they employed DFT calculations to guide the atomic design for completely isolated Ni sites. As revealed in DFT calculation, the adsorptions of acetylene and ethylene π-adsorption was more kinetically favorable on the completely isolated Ni sites while those on partially isolated Ni sites were σ-adsorption. Based on this, they designed NiGa catalyst with completely isolated Ni sites, which was further verified by the experiment results that the NiGa catalyst with completely isolated Ni sites showed superior ethylene selectivity and coking suppression than the Ni_5Ga_3 catalyst with partially isolated Ni sites and the Ni catalyst with multi-atomic ensemble Ni sites. This finding provided ideas for precise designing highly effective catalysts by atomic control.[49] (Figure 1.7)Another example of site-isolation realized by intermetallic compounds was provided by Liu's study, in which

CuNi intermetallic compounds have high ethylene selectivity and catalytic stability, which were mainly associated with the alloying effect of Ni and Cu, endowing Ni with isolated active sites. Consequently, the ensemble effect of contiguous Cu and Ni atoms so oligomerization can be effectively inhibited.[36] All these studies pointed out that the positive effects of the site-isolation achieved by using intermetallic structures featured with specific atomic arrangement.

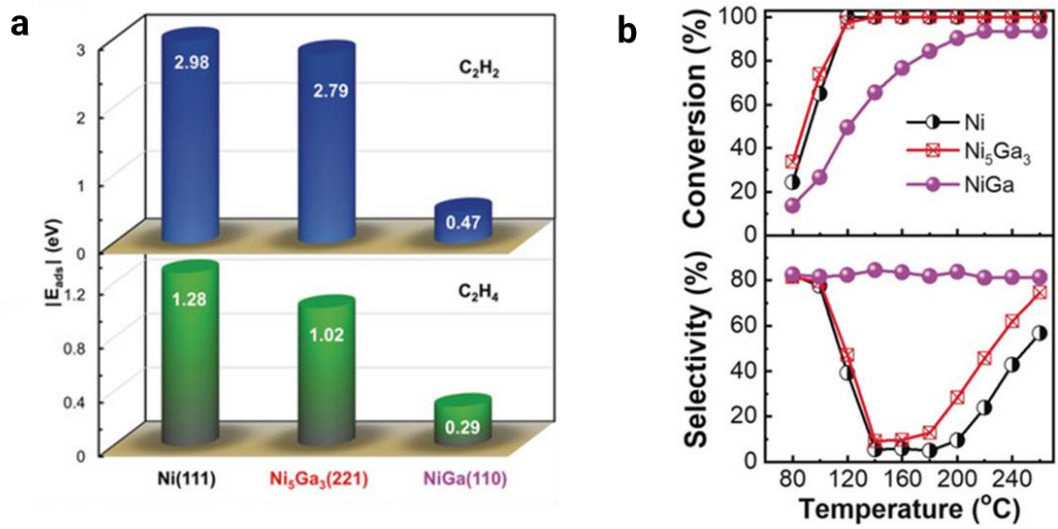

Figure 1.7. (a) Adsorption energies of acetylene and ethylene. **(b)** Acetylene conversion and ethylene selectivity as a function of reaction temperature for acetylene hydrogenation in the absence of ethylene. Reproduced from ref.[49] with permission. Copyright© 2020 Wiley.

Even though the strategy of alloying with the second active component allows the contiguous ensemble sites to be isolated to some extent, sometimes the particle size of the catalysts is typically larger than 2 nm so the active metal dispersion is still relatively low. That is to say, the fully exposed of active metal couldn't be achieved. Thus, it's highly desirable to develop alternative fabrication strategies to prepare well-defined and stable site-isolated catalysts with higher metal loading. Recently, the researchers have further developed strategies such as defect trapping and spatial confinement to achieve atomic dispersion of active metals on metal oxides or carbon materials, to form isolated metal active sites and thus maximized the utilization of active metal atoms.[50–52] Li Yadong's group successfully fabricated the NiSAs/N-C catalyst by in situ reduction of Ni sites under high temperature conditions. NiSAs/N-C catalysts were synthesized by embedding single-atom Ni on nitrogen-doped carbon materials, in which, the aggregation of Ni atoms can be strictly limited by the carbon skeleton. Consequently, the NiSAs/N-C catalysts exhibited excellent catalytic performance even under high temperature reaction conditions at 200 °C, with acetylene conversion and ethylene selectivity exceeding 90%.[53] Similarly, a single-atom Cu catalyst (Cu_1/ND@G) for acetylene

semi-hydrogenation was prepared using surface-defective nanodiamond graphene (ND@G) as the support to atomically disperse Cu. This Cu_1/ND@G catalyst achieved high conversion (95%), high selectivity (98%), and good stability (for more than 60 h) due to the unique structural features that the single-atom Cu was coordinated with three carbon atoms forming the Cu−C3 structure. This ensured the efficient activation of acetylene and easy desorption of ethylene.[53] Besides, owing to their ultra-high specific surface area and uniformity, Mo_3S_4 or W_3S_4 emerged as ideal platform to construct atomically dispersed catalysts.[54] Based on these, Feng et. designed an atomically dispersed non-noble metal Ni catalyst (Ni_1MoS) supported on Al_2O_3. Specifically, Mo_3S_4 clusters with a cubic structure cell afforded a Ni atom to bond with S or Mo atoms at the cell edge to be the crucial active site. This catalyst achieved 90% ethylene selectivity even at full acetylene conversion and no deactivation can be observed while poor catalytic performance was observed over Ni/Al_2O_3 with ensemble Ni sites. Combining experimental results with DFT calculations, the acceleration of selectivity was owing to the isolated $Ni^{\delta+}$ structure induced by Mo and S. Thus, ethylene desorption was more preferential than over-hydrogenation or oligomerization.[55] (Figure 1.8)

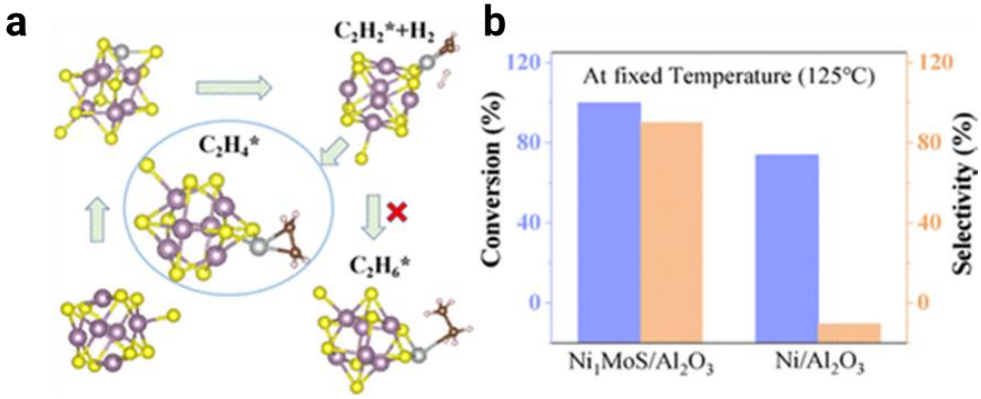

Figure 1.8. (a) Ethylene desorption as opposed to over-hydrogenation or oligomerization occurred over Ni_1MoS/Al_2O_3. (b) Catalytic performance of Ni_1MoS/Al_2O_3 and Ni/Al_2O_3. Reproduced from ref.[55] with permission. Copyright© 2021 American Chemical Society.

Apart from intermetallic compounds, random alloys are also famous materials which are frequently used in catalytic science. Among them, single-atom alloys (SAA), whose active sites were completed isolated with excess amount of the major metal, were regarded as an emerging potential alloy material for target reaction.[56,57] A theoretical work by Zhang and co-workers employed a series of metal-modified Cu-based SAAs for acetylene hydrogenation on a series. A series of promoters Ni, Ag, Au, Pt, Pd, and Rh can extremely promote the catalytic activity but they have different effects on the catalytic performance. Among them, Pd dopant exhibited

the highest selectivity towards ethylene and catalytic activity. Furthermore, utilizing (DFT) calculations, Yang et. concluded that RhCu and NiCu SAAs were unstable because aggregate strongly binding dopants such as Rh and Ni into ensembles while PdCu-SAA and PtCu-SAA gave rise to ethylene desorption, which was consistent with the experimental results in previous literature.[58]

1.3.2.3 Other strategies

I've listed two strategies for regulating the structures of catalysts above. Here are some other methods that have also been reported in the literature.

As I mentioned in section 1.3.1, there are already many examples of metal oxides employed as catalysts for acetylene hydrogenation reactions.[28–30] Many studies pointed out that it is oxygen vacancies on metal oxides that play active roles in acetylene semi-hydrogenation reaction. The surface engineering on defects of metal oxides can create new active sites to control catalytic activity and selectivity, on the basis of which, many efforts have been devoted to control the oxygen vacancies on metal oxides catalysts, including tuning the morphology of oxides and doping other metals to metal oxide catalysts. The recent discovery of CeO_2 as a semi-hydrogenation catalyst due to its unique redox and acid−base properties to form oxygen vacancies has already opened new perspectives in acetylene semi-hydrogenation catalysis. However, the high reaction temperature hindered its application so some researchers validated that doping promoters can boost the oxygen storage capacity and the reducibility of CeO_2.[59] Since then, there have been a number of reports on the addition of metals to oxides for acetylene semi-hydrogenation reactions. For example, Hua Guo's group demonstrated that doping Ni on CeO_2 was a route to alter the active sites, where Ni acted as a promoter rather than directly participating in the catalytic reaction.[60] Later, this group proposed another similar mechanism that when Ga was doped on CeO_2, more surface oxygen vacancies were constructed, thereby creating a template contain frustrated Lewis pairs to promote heterolytic H_2 dissociative chemisorption.[61] The similar conclusion was made over Cu/CeO_2 that Cu-doped CeO_2 (111) led to the formation of oxygen vacancy (O_v), which generated Cu/O and Ce/O frustrated Lewis pairs (FLPs). In this case, H_2 dissociation and acetylene hydrogenation were enhanced.[62] A similar tailing route was also employed over In_2O_3, that is, endowed In_2O_3 with Pt-O_4 moiety ensemble sites. In contrast to the pristine In_2O_3 catalyst, the Pt_1-In_2O_3 catalyst with the ensemble site created exhibits significantly increased hydrogen activation and were beneficial for forming more oxygen vacancy. Thus, Pt_1-In_2O_3 catalyst demonstrated 91%

ethylene selectivity at complete acetylene conversion. This result was in accordance with the theoretical calculation. Such an ensemble site made great contributions to the enhancement of catalytic performance because the hydrogen activation via the heterolytic dissociation of hydrogen was enhanced due to modulated electronic properties of the ensemble sites.[63]

Secondly, for the purpose of improving the hydrogenation activity of metal oxide catalysts, another strategy, the establishment of interfacial site on supported metal nanoparticles, was also confirmed to be effective.[64,65] Reducible metal oxides were served to modify the active sites. After high temperature reduction, the interfacial electronic interactions will present between the ligand-unsaturated oxides and the active metal, which can affect the activity and selectivity of the catalysts. The Ni-based catalysts modified with $Ce_xZr_{1-x}O_2$ were synthesized by loading the active metal Ni on the carrier. It was shown that the high temperature reducing atmosphere treatment led to the generation of a large number of oxygen vacancies on the surface of the $Ce_xZr_{1-x}O_2$ composite metal oxide, which promoted the high dispersion of the active metal Ni on its surface, and enhanced the electron interaction between Ni and $Ce_xZr_{1-x}O_2$, increasing the electron cloud density of the Ni active sites and showing the best activity in the catalytic hydrogenation reaction.[65] Also, inspired by Cu/Fe/Mg/Al layered double hydroxides for acetylene hydrogenation, Fu et al. reported an $Fe_{0.16}MgO_x$-modified Cu interfacial structure with bifunctional catalysis for acetylene semi-hydrogenation. The interfacial $Cu^{\delta-}$ sites can not only active acetylene and hydrogen, but also form an intermediate bound with Fe, in which ethylene preferred desorption rather than over-hydrogenation.[64]

Moreover, interfacial sites can not only be constructed on supported metal nanoparticles and single atoms, but also be grafted via the metal-support interactions. For instance, a hybrid Pd/Bi_2O_3 cluster ensemble on a TiO_2 substrate created metal/oxide interfaces for acetylene semi-hydrogenation. The ethylene adsorption is greatly reduced by the intra-cluster electron transfer to Pd through the as-formed nanoscale metal/oxide interface without impairing the hydrogen activation. As a consequence, selectivity of ethylene and conversion of acetylene were 91% and 90% respectively in a front-end hydrogenation process with a temperature as low as 44 °C.[66] A highly dispersed Ni nanoparticle catalyst Ni/MCM-41 prepared by impregnation method has a high conversion (96%) and high selectivity (87%). The high metal dispersion and the interaction between the metal and the support were responsible for the outstanding catalytic performance.[67]

1.4 Other catalysts

In addition to metal catalysts, other catalyst materials, such as graphene and other carbon materials, have been extensively studied in the field of selective hydrogenation of acetylene. For example, Strizhak et al. first reported acetylene semi-hydrogenation on multiwalled carbon nanotubes (MWCNTs). The highest reaction rate can be obtained at 350 °C with a selectivity to ethylene of 85 % without ethane and the surface functionality of carbon nanotubes differed significantly before and after reaction without changing morphology. In this process, there was a sufficiently high number of defects, a low oxygen content, and a basic surface in the presence of hydroxy and carbonyl groups on the surface of the MWCNT-400.[68] The presence of a large number of defects in the carbon nanotubes during the catalytic process and the functionalization of the surface by hydroxyl and carbonyl groups showed a high selectivity for the preparation of ethylene by acetylene hydrogenation; Strizhak et al. carried out the reduction of graphene oxide by hydrazine hydrate or molecular hydrogen, which have different catalytic performance for acetylene semi-hydrogenation. The presence of nitrogen atoms in the graphene lattice reduced the overall reduced state of graphene, while oxygen-containing functional groups such as hydroxyl groups contributed to the catalytic activity. These results further clarify the potential application of graphene-based materials in the field of selective hydrogenation of acetylene.[69]

1.5 Aim of this thesis

Ethylene is an important symbol of the level of a country's petrochemical industry. New ethylene plants have come on stream in recent years and the pace of increase in ethylene production capacity will further increase in the future and market competition will become more intense. The requirements for acetylene concentration in ethylene are becoming harsher. Acetylene selective hydrogenation is the current and future favorable method of acetylene removal. Noble metal nano catalysts are the most frequently used catalysts for acetylene semi-hydrogenation in industry. However, due to the high cost and unsatisfactory selectivity of noble metals, it is of great importance to search for non-precious metal catalysts for replacement, which is highly in line with the current theme of energy development and environmental protection in the world.

Although great efforts have been made in replacing noble metals with non-precious metals, many problems need to be solved. Through extensive literature survey and summary of

previous research work, I state the research challenges need to be addressed are: (1) the trade-off between acetylene rate and ethylene selectivity; (2) the low activity of non-noble metal; (3) high reaction temperature; (4) passable stability. On the basis of these, for meeting critical requirements, in this work, I provide the following guidelines to precisely modulate and construct bifunctional or even multifunctional catalysts.

1.5.1 Precise adjustment of metallic catalysts

Further precise adjustment of metallic catalysts is essential to achieve the specific catalytic performance target. It is generally believed that site isolation strategy can not only break the trade-off between acetylene rate and ethylene selectivity, but also effectively improve catalytic stability effectively by mitigating the over-hydrogenation and oligomerization. However, for single-atom materials, the active metal needs to be considerably low (typically <1/50) to maintain the isolated sites so achieving high overall reaction rates is a challenging task. Recently, new materials such as multi-metallic materials are opening up new ideas for designing multifunctional catalysts for such complicated reaction systems. Among them, high entropy intermetallics (HEIs) featured with unique structures attracted much interest. HEIs are multi-metallic alloys with five or more elements and specific crystal structures originating from the parent binary intermetallics, which differ considerably from high-entropy alloys (HEAs) with fcc or hcp structures with a random atomic distribution. Therefore, it's potential to obtain truly site-isolated, highly stable catalysts as if we choose a propriate parent structure for HEIs.

What's more, the active site separation can be realized through selective masking of inert components in intermetallic compounds or nanoparticle surfaces, which has been confirmed to be effective in the acetylene semi-hydrogenation reaction. The strength and adsorption type of acetylene reactants and C2 intermediates have been modified to inhibit alkane formation. Even so, this is at the expense of catalytic activity as this reaction usually follows the "L-H" mechanism, where the spatial separation of adsorbed C2 species and adsorbed H_2 species at separated active sites leads to an increase in the energy barrier, resulting in a decrease in reactivity. Faced with this new dilemma, a novel catalyst design concept that enhances the hydrogenation activity of non-noble metal without compromising selectivity is highly desirable. Catalysts with completely isolated sites can suppress the strong σ-adsorption mode while favoring the weak π-adsorption for ethylene, which promotes the ethylene desorption and suppresses its hydrogenation to ethane. As for partially catalysts with isolated active site, the adsorption modes for acetylene and ethylene are still σ-adsorption, which gives rise to

unfavorable selectivity to ethylene but relatively higher hydrogenation activity. Inspired by these, we address the possibility of further optimizing the adsorption/ desorption behaviours of ethylene on such partially isolated active sites towards excellent ethylene selectivity, which could also maintain the relatively higher activity than the completely isolated active sites. Thus, we turn our attention to a new material, a trimetallic pseudo-binary alloy described as $(A_{1-x}A'_x)_mB_n$ that combines the advantages of both random alloys and intermetallic compounds. The parent of this structure is a binary intermetallic compound, but a third metal, C, can be introduced in some ratios without changing the crystal structure. The catalytic performance can be remarkably enhanced by introducing the multifunctional effects.

In addition to the elemental substitution of intermetallic compounds to form multi-metallic catalysts, the incorporation of light elements into the lattice of the active metal is also a proven method to effectively tune the catalytic performance. Therefore, in this study, we also try to precisely control the catalytic performance by introducing light elements to alloy.

Additionally, we cast our attention on metal oxides, which have been proved to be efficient in various reactions including acetylene semi-hydrogenation reactions. Even if metal oxides have been employed in many catalytic reactions, research on the route to improve catalytic performance is limited. I hope this research will open new ideas on how to accurately control the catalytic properties of metal oxides.

1.5.2 Promoting the reaction mechanism of multi-metallic catalysts

There is currently a gap in the mechanistic study of multi-metallic materials for acetylene semi-hydrogenation reactions because the application of such materials in thermocatalytic reactions is still in its infancy. Moreover, the multi-metallic materials system is particularly complex due to the large number of elements in the material, so that the role of each element and the interactions between them cannot be easily and clearly explored. Therefore, it's of great significance to further investigate the relationship between catalyst structure and catalytic performance using a variety of methods such as kinetic studies, in situ characterization (IR, XAFS, XPS and temperature programming analysis), DFT calculations and so on. Non-metallic catalysts still have a long way to go from academic research to effective industrial applications because there is still room for improvement in catalytic performance and clarification of reaction mechanisms. Thus, I hope my work will clarify the mechanism of action of multi-metallic catalysts for acetylene semi-hydrogenation. Furthermore, it can inspire

readers to design more efficient catalysts and provide ideas for other applications of metallic catalysts in catalysis.

In addition, HEI and Heusler alloys can be considered as a well-defined platform to reveal the catalysis of intermetallic compounds as elemental substitution can be used to investigate catalysis with different electronic structures and various surface elements under the same parent crystal structure.

1.6 Outline of thesis

Based on these objectives, structure manipulation was revealed on (1) high-entropy intermetallics (HEIs), a multi-metallic alloy with five or more elements with specific crystal structure derived from the parent binary intermetallic; (2) pseudo-binary alloy, a ternary alloy described as $(A_{1-x}A'_x)_mB_n$, where a part of active metal A is substituted by a similar third element A'.

Chapter 2 presented a novel catalyst design based on high entropy intermetallics (HEI), which provide thermally stable isolated Ni without excess counterpart metals and achieve exceptionally high performance. Intermetallic NiGa was multi-metalized to a (NiFeCu)(GaGe), where the Ni and Ga sites were partially substituted with Fe/Cu and Ge, respectively, without altering the parent CsCl-type structure. The NiFeCuGaGe/SiO_2 HEI catalyst completely inhibited ethylene over-hydrogenation even at complete acetylene conversion and exhibited five-times higher activity than other 3d-transition-metal-based catalysts. The DFT study showed that the surface energy was decreased by multimetallization, which drastically weakened ethylene adsorption.

The first-generation HEI achieves high selectivity at full acetylene conversion. Ni sites in HEI were completely isolated, which weakened the adsorption of ethylene, leading to excellent selectivity. However, the weak adsorption of reactants, the lower hydrogen dissociation ability, and the change in reaction pathway due to the lack of ensemble metal sites, reduce its hydrogenation reactivity, which is evidenced by the higher reaction temperature required to achieve the approximately 100% conversion (220°C). A high reaction temperature often leads to oligomerization, which fouls the catalyst surface and deactivates the catalyst. Therefore, in **Chapter 3**, we report a flexibly tunable catalyst design concept based on a pseudo-binary alloy, which enabled a remarkable enhancement in the catalytic activity, selectivity, and durability of a Ni-based material. A series of $(Ni_{1-x}Cu_x)_3Ga/TiO_2$ catalysts exhibiting $L1_2$-type pseudo-binary alloy structures with various Cu contents (x = 0.2, 0.25, 0.33, 0.5, 0.6, and 0.75) were

prepared for active site tuning. The optimal catalyst, $(Ni_{0.8}Cu_{0.2})_3Ga/TiO_2$, exhibited outstandingly high catalytic activity among the reported 3d transition metal-based systems and excellent ethylene selectivity (96%) and long-term stability (100 h) with near full conversion even at 150°C. A mechanistic study revealed that Ni_2Cu hollow sites on the (111) surface weakened the strong adsorption of acetylene and vinyl adsorbate, which significantly accelerated the hydrogenation process and inhibited undesired ethane formation.

Our first- and second-generation catalysts showed great catalytic performance for acetylene semi-hydrogenation, but they were operated at low gas hourly space velocity (GHSV), 30000 and 37500 mL g^{-1} h^{-1} respectively. Similarly, most reported catalysts can only maintain a high acetylene conversion at a low GHSV. That is to say, there is still much room for improvement in the handling capacity of the existing non-noble metal catalysts. Thus, in **Chapter 4**, we attempt to improve the catalytic activity of Ni–Zn alloy in acetylene semi-hydrogenation without lowering its selectivity using the silica-decoration method. Ni–Zn alloy nanoparticles on SiO_2 were further decorated by additional silica, which significantly increased the acetylene conversion (15%–97%) without decreasing the ethylene selectivity (ca. 80%) at 200°C under a remarkably high GHSV (128000 mL g^{-1} h^{-1}).

Metal oxides are used in various catalytic systems but there is still much room for further improvement in catalytic performance. Thus, it makes sense to investigate effective ways of modifying catalytic properties based on metal oxides. Herein, in **Chapter 5**, we report on another strategy for structure regulation based on In_2O_3. At first, In_2O_3 was supported on SiO_2 for higher efficiency to form In_2O_3/SiO_2, which was active for acetylene semi-hydrogenation, deactivation occurred within a few hours probably due to by-production of poisonous species. When In_2O_3/SiO_2 was further doped with a small amount of Co (0.5 wt%), the acetylene conversion and ethylene selectivity remained high (approximately 70%). For the Co/ In_2O_3/SiO_2 catalyst, the hydrogen pretreatment temperature had strong influence on the catalytic performance, in which reduction by H_2 at 250°C resulted in the best stability. A temperature-programmed reduction study suggested that metallic Co species contributed to inhibiting the formation of poisonous by-products, which allowed the stability to be improved.

1.7 Concluding Remark

In summary, the innovative catalyst design concept we proposed in this study not only developed highly efficient catalysts for acetylene semi-hydrogenation, but also provided a fresh perspective on how to design and tune multi-metallic catalysts. The insights obtained in this

study accelerate the development of multi-metallic catalysts and industrial processes for the purification of acetylene.

References

[1] A. Borodziński, A. Cybulski, *Applied Catalysis A: General* **2000**, *198*, 51.

[2] D. Duca, F. Frusteri, A. Parmaliana, G. Deganello, *Applied Catalysis A: General* **1996**, *146*, 269.

[3] W. J. Kim, S. H. Moon, *Catalysis Today* **2012**, *185*, 2.

[4] D. V. Glyzdova, N. S. Smirnova, D. A. Shlyapin, P. G. Tsyrul'nikov, *Russian Journal of General Chemistry* **2020**, *90*, 1120.

[5] H. Zea, K. Lester, A. K. Datye, E. Rightor, R. Gulotty, W. Waterman, M. Smith, *Applied Catalysis A: General* **2005**, *282*, 237.

[6] L. Zhang, M. Zhou, A. Wang, T. Zhang, *Chemical Reviews* **2020**, *120*, 683.

[7] A. J. McCue, J. A. Anderson, *Frontiers of Chemical Science and Engineering* **2015**, *9*, 142.

[8] J. Sheridan, *J. Chem. Soc.* **1945**, 305.

[9] Y. Lu, R. Reeves, K. Kubik, *Systems Engineering* **1998**, *I*, 1.

[10] Frevel, L.K.; Kressley, L.J., U.S. Patent **1957**, 2,802, 889.

[11] G. C. Bond, D. A. Dowden, N. Mackenzie, *Transactions of the Faraday Society* **1958**, *54*, 1537.

[12] S. Leviness, V. Nair, A. H. Weiss, Z. Schay, L. Guczi, *Journal of Molecular Catalysis* **1984**, *25*, 131.

[13] P. Of, F. A. S. Bases, **1960**, 10.

[14] K. Kovnir, J. Osswald, M. Armbrüster, R. Giedigkeit, T. Ressler, Y. Grin, R. Schlögl, *Studies in Surface Science and Catalysis* **2006**, *162*, 481.

[15] Y. H. Park, G. L. Price, *Journal of the Chemical Society, Chemical Communications* **1991**, 1188.

[16] Y. H. Park, G. L. Price, *Industrial and Engineering Chemistry Research* **1992**, *31*, 469.

[17] E. W. Shin, C. H. Choi, K. S. Chang, Y. H. Na, S. H. Moon, *Catalysis Today* **1998**, *44*, 137.

[18] O. Matselko, R. R. Zimmermann, A. Ormeci, U. Burkhardt, R. Gladyshevskii, Y. Grin, M. Armbrüster, *Journal of Physical Chemistry C* **2018**, *122*, 21891.

[19] B. Yang, R. Burch, C. Hardacre, G. Headdock, P. Hu, *ACS Catalysis* **2012**, *2*, 1027.

[20] G. X. Pei, X. Y. Liu, A. Wang, Y. Su, L. Li, T. Zhang, *Applied Catalysis A: General* **2017**, *545*, 90.

[21] C. S. Spanjers, J. T. Held, M. J. Jones, D. D. Stanley, R. S. Sim, M. J. Janik, R. M. Rioux, *Journal of Catalysis* **2014**, *316*, 164.

[22] J. K. N. Felix Studt, Frank Abild-Pedersen, Thomas Bligaard, 1 Rasmus Z. Sørensen, Claus H. Christensen, *Science* **2008**, *320*, 1320.

[23] P. Tyler, *Labour's Lost Leader* **2020**, 1320.

[24] L. Wang, F. Li, Y. Chen, J. Chen, *Journal of Energy Chemistry* **2019**, *29*, 40.

[25] X. Shi, Y. Lin, L. Huang, Z. Sun, Y. Yang, X. Zhou, E. Vovk, X. Liu, X. Huang, M. Sun, S. Wei, J. Lu, *ACS Catalysis* **2020**, *10*, 3495.

[26] G. Kyriakou, M. B. Boucher, A. D. Jewell, E. A. Lewis, T. J. Lawton, A. E. Baber, H. L. Tierney, M. Flytzani-stephanopoulos, E. C. H. Sykes, **2012**, *335*, 1209.

[27] T. Kojima, S. Kameoka, S. Fujii, S. Ueda, A. P. Tsai, *Science Advances* **2018**, *4*, 1.

[28] J. Carrasco, G. Vilé, D. Fernández-Torre, R. Pérez, J. Pérez-Ramírez, M. V. Ganduglia-Pirovano, *Journal of Physical Chemistry C* **2014**, *118*, 5352.

[29] D. Albani, M. Capdevila-Cortada, G. Vilé, S. Mitchell, O. Martin, N. López, J. Pérez-Ramírez, *Angewandte Chemie* **2017**, *129*, 10895.

[30] Q. Wan, Y. Chen, S. Zhou, J. Lin, S. Lin, *Journal of Materials Chemistry A* **2021**, *9*, 14064.

[31] Y. Deng, Y. Ge, M. Xu, Q. Yu, D. Xiao, S. Yao, D. Ma, *Accounts of Chemical Research* **2019**, *52*, 3372.

[32] R. M. Mironenko, O. B. Belskaya, V. A. Likholobov, *Russian Journal of General Chemistry* **2020**, *90*, 532.

[33] C. Yang, Z. Wu, G. Zhang, H. Sheng, J. Tian, Z. Duan, H. Sohn, A. J. Kropf, T. Wu, T. R. Krause, J. T. Miller, *Catalysis Today* **2019**, *323*, 123.

[34] B. Bridier, J. Pérez-Ramírez, *Journal of the American Chemical Society* **2010**, *132*, 4321.

[35] T. Komatsu, T. Kishi, T. Gorai, *Journal of Catalysis* **2008**, *259*, 174.

[36] Y. Liu, J. Zhao, J. Feng, Y. He, Y. Du, D. Li, *Journal of Catalysis* **2018**, *359*, 251.

[37] Y. Song, S. Laursen, *Journal of Catalysis* **2019**, *372*, 151.

[38] D. M. Rao, S. T. Zhang, C. M. Li, Y. Di Chen, M. Pu, H. Yan, M. Wei, *Dalton Transactions* **2018**, *47*, 4198.

[39] Y. Chen, J. Chen, *Applied Surface Science* **2016**, *387*, 16.

[40] C. W. A. Chan, A. H. Mahadi, M. M. J. Li, E. C. Corbos, C. Tang, G. Jones, W. C. H. Kuo, J. Cookson, C. M. Brown, P. T. Bishop, S. C. E. Tsang, *Nature Communications* **2014**, *5*, 1.

[41] S. Büchele, Z. Chen, E. Fako, F. Krumeich, R. Hauert, O. V. Safonova, N. López, S. Mitchell, J. Pérez-Ramírez, *Angewandte Chemie - International Edition* **2020**, *59*, 19639.

[42] Y. Niu, X. Huang, Y. Wang, M. Xu, J. Chen, S. Xu, M. G. Willinger, W. Zhang, M. Wei, B. Zhang, *Nature Communications* **2020**, *11*, 1.

[43] X. Ge, Z. Ren, Y. Cao, X. Liu, J. Zhang, G. Qian, X. Gong, L. Chen, X. Zhou, W. Yuan, X. Duan, *Journal of Materials Chemistry A* **2022**, *10*, 19722.

[44] E. R. and A. M. J.C. Rodriguez, A.J. Marchi , A. Borgna, *Studies in Surface Science and Catalysis* **2001**, *139*, 1.

[45] S. Liu, Y. Niu, Y. Wang, J. Chen, X. Quan, X. Zhang, B. Zhang, *Chemical Communications* **2020**, *56*, 6372.

[46] A. Dasgupta, H. He, R. Gong, S. L. Shang, E. K. Zimmerer, R. J. Meyer, Z. K. Liu, M. J. Janik, R. M. Rioux, *Nature Chemistry* **2022**, *14*, 523.

[47] A. P. Tsai, S. Kameoka, K. Nozawa, M. Shimoda, Y. Ishii, *Accounts of Chemical Research* **2017**, *50*, 2879.

[48] S. Furukawa, T. Komatsu, *ACS Catalysis* **2017**, *7*, 735.

[49] Y. Cao, H. Zhang, S. Ji, Z. Sui, Z. Jiang, D. Wang, F. Zaera, X. Zhou, X. Duan, Y. Li, *Angewandte Chemie* **2020**, *132*, 11744.

[50] L. Li, Z. Li, W. Yang, Y. Huang, G. Huang, Q. Guan, Y. Dong, J. Lu, S. H. Yu, H. L. Jiang, *Chem* **2021**, *7*, 686.

[51] L. Nie, D. Mei, H. Xiong, B. Peng, Z. Ren, X. I. P. Hernandez, A. DeLaRiva, M. Wang, M. H. Engelhard, L. Kovarik, A. K. Datye, Y. Wang, *Science* **2017**, *358*, 1419.

[52] P. Xie, T. Pu, A. Nie, S. Hwang, S. C. Purdy, W. Yu, D. Su, J. T. Miller, C. Wang, *ACS Catalysis* **2018**, *8*, 4044.

[53] X. Dai, Z. Chen, T. Yao, L. Zheng, Y. Lin, W. Liu, H. Ju, J. Zhu, X. Hong, S. Wei, Y. Wu, Y. Li, *Chemical Communications* **2017**, *53*, 11568.

[54] J. Jiang, M. Gao, W. Sheng, Y. Yan, *Angewandte Chemie - International Edition* **2016**, *55*, 15240.

[55] B. Fu, A. J. McCue, Y. Liu, S. Weng, Y. Song, Y. He, J. Feng, D. Li, *ACS Catalysis* **2022**, *12*, 607.

[56] R. T. Hannagan, G. Giannakakis, M. Flytzani-Stephanopoulos, E. C. H. Sykes, *Chemical Reviews* **2020**, *120*, 12044.

[57] T. Zhang, A. G. Walsh, J. Yu, P. Zhang, *Chemical Society Reviews* **2021**, *50*, 569.

[58] K. Yang, B. Yang, *Physical Chemistry Chemical Physics* **2017**, *19*, 18010.

[59] G. Vilé, P. Dähler, J. Vecchietti, M. Baltanás, S. Collins, M. Calatayud, A. Bonivardi, J. Pérez-Ramírez, *Journal of Catalysis* **2015**, *324*, 69.

[60] C. Riley, S. Zhou, D. Kunwar, A. De La Riva, E. Peterson, R. Payne, L. Gao, S. Lin, H. Guo, A. Datye, *Journal of the American Chemical Society* **2018**, *140*, 12964.

[61] S. Zhou, L. Gao, F. Wei, S. Lin, H. Guo, *Journal of Catalysis* **2019**, *375*, 410.

[62] A. H. A. F. Study, S. Zhou, Q. Wan, **2022**, *2*.

[63] Y. Li, Y. Cao, X. Ge, H. Zhang, K. Yan, J. Zhang, G. Qian, Z. Jiang, X. Gong, A. Li, X. Zhou, W. Yuan, X. Duan, *Journal of Catalysis* **2022**, *407*, 290.

[64] F. Fu, Y. Liu, Y. Li, B. Fu, L. Zheng, J. Feng, D. Li, *ACS Catalysis* **2021**, *11*, 11117.

[65] F. Ocampo, B. Louis, L. Kiwi-Minsker, A. C. Roger, *Applied Catalysis A: General* **2011**, *392*, 36.

[66] S. Zou, B. Lou, K. Yang, W. Yuan, C. Zhu, Y. Zhu, Y. Du, L. Lu, J. Liu, W. Huang, B. Yang, Z. Gong, Y. Cui, Y. Wang, L. Ma, J. Ma, Z. Jiang, L. Xiao, J. Fan, **2021**, 1.

[67] J. Zhao, L. He, J. Yu, Y. Shi, R. Miao, Q. Guan, P. Ning, *New Journal of Chemistry* **2021**, *45*, 1054.

[68] I. B. Bychko, A. A. Abakumov, N. V. Lemesh, P. E. Strizhak, *ChemCatChem* **2017**, *9*, 4470.

[69] A. A. Abakumov, I. B. Bychko, O. V. Selyshchev, D. R. T. Zahn, X. Qi, J. Tang, P. E. Strizhak, *Carbon* **2020**, *157*, 277.

Chapter Two

Nickel–-Based High-Entropy Intermetallic as a Highly Active and Selective Catalyst for Acetylene Semi-hydrogenation

2.1 Introduction

Acetylene semi-hydrogenation is a critical industrial process that supplies polymer-grade ethylene for polyethylene production. In this process, the acetylene impurity in crude ethylene is hydrogenated selectively to ethylene, while at the same time, the over-hydrogenation and oligomerization of ethylene are prevented.[1,2] In industry, Pd–Ag bimetallic materials are commonly used as selective semi-hydrogenation catalysts.[3] Intermetallic compounds such as PdGa, [3–5] PdIn,[6] and PdZn[7] are also known as good catalysts for this reaction. However, the high cost of Pd has highlighted the need for more cost-effective catalysts and economically beneficial processes. In this context, the development of efficient non-noble metal-based catalysts for acetylene semi-hydrogenation is attractive and desirable from a pure and applied chemistry point of view.

Recently, late 3d transition metal-based catalysts such as NiZn[1], Ni_xGa_y[8], $Al_{13}Fe_4$[9], $Cu/Fe_{0.16}MgO_x$[10] have been reported as cost-effective alternatives to the Pd-based catalysts for acetylene semi-hydrogenation. Among them, Ni-based catalysts are most widely studied due to the greater hydrogenation ability. However, achieving high catalytic activity and selectivity using Ni-based materials is still a significant challenge because of the much lower activity of Ni than Pd and the difficulty in preventing the over-hydrogenation of ethylene at near-complete acetylene conversions. Moreover, there is a trade-off between the acetylene conversion rate and ethylene selectivity because of the linear scaling relationships between the binding energies of acetylene and ethylene.[3,11-14] These drawbacks have hindered the development of highly efficient catalysts using Ni for acetylene semi-hydrogenation. Single-atom alloys (SAAs), in which an active metal is isolated by inert host metals, can break this scaling relationship,[15,16] thereby increasing the turnover frequency (TOF) and selectivity in some catalytic systems, including acetylene semi-hydrogenation. However, the concentration of the active metal must be considerably low (typically <1/50) to retain the isolated state.[15] A similar situation occurs in catalysis using single-atom materials. Therefore, obtaining high overall reaction rates is a challenging task, even if the TOF is enhanced remarkably. Thus, an innovative catalyst design and material should be established to overcome this dilemma.

This paper introduces a novel design concept using high entropy intermetallics (HEIs) to produce highly active and selective catalysis for acetylene semi-hydrogenation. HEIs are multimetallic alloys with five or more elements and specific crystal structures originating from the parent binary intermetallics, which differ considerably from high-entropy alloys (HEAs) with fcc or hcp structures with a random atomic distribution (Figure 2.1).

A new Ni-based HEI catalyst was designed based on intermetallic NiGa with a simple CsCl-type structure, which is also a good semi-hydrogenation catalyst.[85] On the most stable {110} planes of NiGa, the coordination number of surface Ni is only two because one-dimensionally aligned Ni and Ga columns are arranged alternately (Figure 2.1c). Therefore, the surface Ni atoms can be isolated without excess counterpart metals, unlike HEAs, when the Ni site is partially replaced with less active metals. The Ga site can also be substituted with another element to increase the mixing entropy and thermodynamic stability. Such site-specific substitution is possible when analogous elements are chosen.[86] Here, we chose less active Fe and Cu so that the Ni sites were "catalytically" isolated (Figure 2.1c). Co was excluded due to its relatively high hydrogenation activity. Ge was chosen as a Ga analog due to the similarity in electronegativity and atomic size. Thus, site-specific multi-metallization of intermetallics allows the construction of sufficiently isolated and thermodynamically stable Ni sites for hydrogenation with relatively high Ni contents. Surprisingly, this HEI catalyst exhibited outstanding ability to inhibit the over-hydrogenation of ethylene and remarkably high catalytic activity compared to other selective Ni-based hydrogenation catalysts.[8,19-30] Herein, we report the innovative material, design, and catalytic performance of acetylene semi-hydrogenation chemistry. To the best of our knowledge, this is the first example of a high-entropy material for selective hydrogenation reaction.

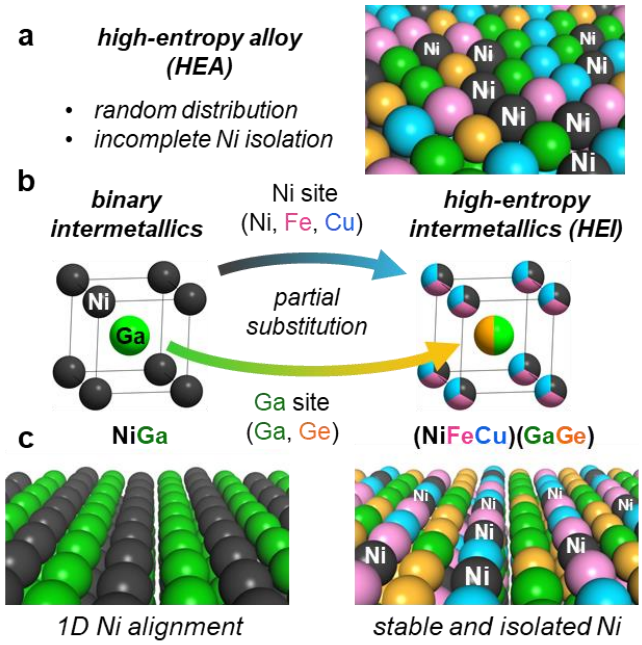

Figure 2.1. Catalyst design concept based on HEI: a) Surface structure of a Ni-based HEA. b) Multi-metallization of intermetallic NiGa to (NiFeCu)(GaGe) HEI. c) Surface structure of the (110) planes of NiGa and (NiFeCu)(GaGe) HEI.

2.2 Experimental section

2.2.1 Catalyst preparation

$NiGa/SiO_2$ (Ni: 3wt. %) and $NiFeCuGaGe/SiO_2$ (Ni: 1 wt. %) catalysts were prepared by the pore-filling co-impregnation method using Ni $(NO_3)_2 \cdot 6H_2O$ (Wako, 99.9%), Fe $(NO_3)_3 \cdot 9H_2O$ (Furuya Metal Co. Ltd.), $Cu(NO_3)_2 \cdot 3H_2O$ (Furuya Metal Co. Ltd.), Ga $(NO_3)_3 \cdot nH_2O$ (n = 7–9, Wako, 99.9%), and $(NH_4)_2GeF_6$ (Furuya Metal Co. Ltd., 99%) as metal precursors. A mixed solution of metal precursors (atomic ratio: Ni:Ga = 1:1, Ni:Fe:Cu:Ga:Ge =1:1:1:1:1) was added dropwise to SiO_2 (CARiACT G–6, Fuji Silysia, S_{BET} = 673 $m^2\ g^{-1}$). The resulting mixtures were sealed and aged overnight at room temperature. The mixture was then transferred to a round-bottom flask and frozen in liquid nitrogen. The frozen sample was dried in a vacuum at ca. −5°C, followed by drying overnight in an oven at 90°C. For the HEI catalyst, the resulting powder was calcined at 400°C for 1 h, followed by reduction at 700°C in flowing H_2 (40 mL min^{-1}). For NiGa, the dried powder was reduced at 800°C under similar conditions without calcination. The ramping rate was 10°C min^{-1} for the calcination and reduction procedures.

The corresponding quaternary intermetallic catalysts were prepared in asimilar manner with the following atomic ratio: Ni:Cu:Ga:Ge =1:1:1:1, Ni:Fe:Ga:Ge =1:1:1:1, and Ni:Fe:Cu:Ga =1:1:1:2.

2.2.2 Characterization

The XRD patterns of the catalysts were obtained using a MiniFlex 700 + D/teX Ultra (X-ray source: Cu Kα radiation). Synchrotron XRD was measured at the BL19B2 beamlines of SPring-8, Japan Synchrotron Radiation Research Institute (JASRI). A wavelength of 0.5 Å (25 keV) was used as the X-ray source. HAADF–STEM analysis was conducted using a JEOL JEM-ARM200 M microscope equipped with an EDX detector. The XAFS spectra of the catalyst samples and reference compounds were recorded at the BL14B2 beamline in SPring-8, JASRI in transmission mode using a Si (111) double-crystal monochromator at room temperature. Before the measurements, the catalyst was pelletized (ca. 150 mg with a diameter of 7 mm) and pretreated by H_2 at 700°C (HEI/SiO_2) or 800°C (NiGa/SiO_2) for 0.5 h in a quartz tube. Subsequently, a quartz tube containing the reduced pellet was sealed and transferred to an Argon grove box (O_2: <0.01 ppm) to prevent exposure to air. The pellet was sealed in a plastic film bag (Barrier Nylon) together with an oxygen absorber (ISO A500-HS: Fe powder). The resulting XAFS spectra were analyzed using Athena and Artemis software ver. 0.9.25 implemented in the Demeter package.[31] A Fourier-transform of the EXAFS oscillations was obtained in the *k* range of 3−14 $Å^{-1}$. A back Fourier-transform obtained in the *R* range of 1.5−3.5 Å was used for curve fitting. FEFF8 was used to calculate the backscattering amplitude and phase shift functions.[32]

Temperature-programed analyses were conducted using a BELCAT-II (Microtrac BEL) instrument. For H_2-TPR, 35 mg of the as-calcined (not reduced) catalyst was pretreated under Ar flow (20 mL min^{-1}) at 300°C for 30 min to remove the weakly absorbed species, such as H_2O, followed by cooling to 100°C. The reduction was initiated under flowing 5% H_2/Ar (20 mL min^{-1}) from 100°C to 900°C at a ramping rate of 2°C min^{-1}. H_2 consumption was quantified using a thermal conductivity detector (TCD) placed downstream in the apparatus. For H_2-TPD, 50 mg of the as-prepared catalyst was pretreated at 500°C under flowing 5%H_2/Ar

(20 mL min^{-1}) for 0.5 h and cooled to 50°C under flowing Ar for 0.5 h. The resulting catalyst was exposed to H_2 for 1 h at 50°C and flushed with Ar to remove the weakly adsorbed species. The temperature was then increased from 50°C to 700°C at a ramp rate of 5°C min^{-1} under flowing Ar, where the desorbed species were analyzed by quadrupole mass spectrometry placed downstream. C_2H_4-(H_2-) TPSR was conducted in a similar manner to that of H_2-TPD using 100 mg of the as-reduced catalyst, He carrier gas, and the reaction gas mixture of C_2H_4 + H_2 (20 + 10 mL min^{-1}) or C_2H_4 alone (20 mL min^{-1}).

2.2.3 Catalytic reaction

Acetylene semi-hydrogenation was carried out in a quartz fixed-bed reactor with a 6 mm internal diameter at atmospheric pressure. Typically, a certain amount of catalyst (0.1 g for HEI, 0.2 g for NiGa) diluted with quartz sand (total 2.0 g) was loaded in the quartz tube, which was reduced in flowing H_2 gas (20 mL min^{-1}) at 500°C for 0.5 h and cooled to 30°C under a N_2 flow (20 mL min^{-1}). A reactant gas mixture (C_2H_2:H_2:C_2H_4:He = 1:10:10/0:39 mL min^{-1}) was then fed into the reactor. The temperature dependence of the catalytic performance was evaluated from 100°C to 250°C at a ramp rate of 10°C min^{-1}. The outlet gas was analyzed using an online gas chromatograph (Shimadzu GC-8A with a column of Unipak S, GL Science) equipped with a TCD. C_2H_4 and C_2H_6 were the only C_2 products detected by GC. No green oil, C1, and C4 compounds were detected under the reaction conditions used in this study. The acetylene conversion and ethylene selectivity were estimated using the following equations:

$$C_2H_2 \text{ conversion} = \frac{[C_2H_2]_{inlet} - [C_2H_2]_{outlet}}{[C_2H_2]_{inlet}} \times 100\% \quad (1)$$

$$C_2H_4 \text{ selectivity} = 1 - \frac{\frac{[CH_4]_{outlet}}{2} + [C_2H_6]_{outlet} + 2*[C_4]_{outlet}}{[C_2H_2]_{inlet} - [C_2H_2]_{outlet}} \times 100\% \quad (2)$$

All kinetic studies (Arrhenius-type plots and reaction orders) were conducted in the low conversion region (<15%) by adjusting the catalyst amount. All data points were collected four times at 15 min intervals, of which the average was reported.

2.2.4 Computational details

Periodic DFT calculations were performed using the CASTEP code[33] with Vanderbilt-type ultrasoft pseudopotentials and the revised version of Perdew−Burke−Ernzerhof exchange−correlation functional based on the generalized gradient approximation.[34] The plane-wave basis set was truncated at a kinetic energy of 360 eV. A Fermi smearing of 0.1 eV was used. Dispersion correlations were considered using the Tkatchenko–Scheffler method with a scaling coefficient of s_R = 0.94 and a damping parameter of d = 20.[35] The reciprocal space was sampled using a *k*-point mesh with a typical spacing of 0.04 $Å^{-1}$, as generated by the Monkhorst−Pack scheme.[36] Geometry optimizations were performed on supercell structures using the periodic boundary conditions. The unit cell size of the bulk NiGa crystal was first optimized. Then, the unit cell was rebuilt so that the [110] direction of the primitive cell was oriented along the z-axis. The cell was then expanded to a (2×2×2) supercell. A slab structure was prepared using this supercell (thickness of four atomic layers) with 13 Å of vacuum spacing on the z-axis, followed by the geometry optimization with the cell size fixed for surface relaxation. The convergence criteria for structure optimization and energy calculation were set to (a) an SCF tolerance of 1.0×10^{-6} eV per atom, (b) an energy tolerance of 1.0×10^{-5} eV per atom, (c) a maximum force tolerance of 0.05 eV $Å^{-1}$, and (d) a maximum displacement tolerance of 1.0×10^{-3} Å. For all calculations, the net charge was set to zero and spin polarization was considered. The adsorption energy was defined as follows: $E_{ad} = E_{A\text{-}S} - (E_S + E_A)$, where $E_{A\text{-}S}$, E_A, and E_S are the energy of the slab together with the adsorbate, the total energy of the free adsorbate, and the total energy of the bare slab, respectively. The surface energy was calculated for the most stable (110) plane of NiGa and the corresponding layers of HEI. The surface energy was defined as follows: $\gamma = (E_S - NE_B)/2A$, where E_B, A, and N are the energy of bulk unit cell, surface area, and number of unit cells in the slab, respectively. A transition state search was carried out based on the complete linear synchronous transit/quadratic synchronous transit method[37,38] with the tolerance for all root-mean-square forces on an atom of 0.10 eV $Å^{-1}$.

The HEI structure was constructed by substituting some Ni and Ga atoms in the NiGa–(2×2×2) supercell with Fe/Cu and Ge atoms, respectively, so that the Ni/(Fe+Ni+Cu) and

Ga/(Ga+Ge) ratios were close to 0.33 and 0.5, respectively (total number: Ni = 10, Fe = 11, Cu = 11, Ga = 16, and Ge = 16). The configuration of each element (Ni, Fe, and Cu in the Ni sites and Ga and Ge in the Ga sites) was determined randomly using the RAND and RANK functions in Excel. Besides, the following restrictions were used to maximize the configuration entropy, which cannot be considered by the conventional DFT and is expected to be thermodynamically likely. (1) All the Ni atoms in each (110) layer were isolated (no Ni–Ni); (2) the number of each element in each (110) layer was similar (Ni, Fe, and Cu = 2 or 3, and Ga and Ge = 4). Five configurations that were optimized geometrically were generated (bulk structures: A1–A5), and twenty slab models that exposed each (110) layer (A1a–A5d, Figure 2.19) were constructed. The A1 and A4 configurations showed slightly lower surface energies than the other configurations (Figure 2.21a), which were used for surveying the E_{ad} of ethylene. Twenty different Ni sites in eight (110) layers (A1a–d and A4a–d) were considered for the π-adsorption of ethylene (number of Ni sites in Figure 2.19 corresponds to those in Figure 2.21b). Finally, the A4d1 Ni site, which showed an E_{ad} of ethylene closest to the average, was chosen as the standard surface of HEI for the hydrogenation reactions.

2.3 Results

2.3.1 Characterization of the catalysts structure

First, NiGa and NiFeCuGaGe-HEI catalysts were prepared using a pore-filling co-impregnation method with silica as the support. Figure 2.1a-2.1f show a high-angle annular dark-field scanning transmission electron microscopy (HAADF–STEM) image of NiFeCuGaGe/SiO_2 and the corresponding elemental maps acquired by energy-dispersive X-ray spectroscopy. Small nanoparticles (<5nm) were formed on the silica support, where Fe, Ni, Cu, Ga, and Ge were distributed evenly throughout the nanoparticles, indicating the homogeneous formation of quinary alloy nanoparticles. Similar trends were also observed in other regions of STEM images (Figures 2.2 and 2.3). The particle size ranged from 2 to 6 nm, with a mean particle size of 4.9 nm (Figure 2.1g). A similar size was also observed for NiGa/SiO_2 (4.1 nm, Figure 2.4). Figure 2.1i presents the synchrotron X-ray diffraction (XRD) pattern of HEI, which concurred with that of intermetallic NiGa, but was different from that of

any fcc alloy. This suggests that the quinary alloy nanoparticles retain the NiGa intermetallic structure. Although minor peaks of an impurity phase assignable to $Cu_{0.8}Ga_{0.2}$ were also observed at 13.5° and 26.0° (Figure 2.5), its contribution to the overall catalysis may be ignorable because of the low concentration and activity of Cu. The high-resolution STEM image revealed an atomic arrangement with lattice spacings of 2.06 Å and a dihedral angle of 60°, which matched closely with those of the intermetallic NiGa crystal viewed along the [1$\bar{1}$1] direction (2.05 Å for NiGa{110} planes, Figure 2.1h).[39] X-ray absorption spectroscopy (XAFS) was used to clarify the electronic structure and coordination environment of HEI. For both Ni and Ga K-edges, the XANES features of HEI were similar to those of NiGa (Figures 2.1j and 2.1k), suggesting that the electronic states of Ni and Ga little changed upon multi-metallization. The Ni K adsorption edges of NiGa and HEI were lower in energy than that of Ni foil. In contrast, opposite trends were observed in the Ga K-edge, indicating electron transfer fromGa to Ni, as reported elsewhere.[17] The Fe, Cu, and Ge K-edge XANES spectra of HEI confirmed that these elements were all in the metallic states (Figure 2.6). This is consistent with the result of the temperature-programed reduction, in which the HEI/SiO_2 catalyst was reduced completely by H_2 at 700°C (Figure 2.7). The white line intensities of NiGa and HEI were higher than that of Ga metal, which was attributed to electron transfer from Ga to Ni or strong interaction between Ga and the lattice oxygen of silica or both. Ga in HEI is likely to bind the lattice oxygen preferentially because it is the most oxophilic element among the five constituent metals.[40] However, we cannot exclude the presence of a small fraction of Ga oxide phase. Figure 2.1l summarizes the EXAFS raw oscillations of the reference foils, NiGa, and HEI. The oscillation features of HEI in Fe, Ni, and Cu K-edges were similar to that of NiGa in the Ni K-edge, whereas it was different from those of the reference foils. Hence, these transition metals are not in the monometallic bcc or fcc structure but are present in a crystallographically equivalent position to the Ni site in NiGa. A similar trend was observed for the typical elements; the Ge K-edge EXAFS of HEI agreed with that of NiGa in the Ga K-edge, indicating that Ge substituted for the Ga site of NiGa. Curve fitting analysis was also conducted for the EXAFS oscillations (Table 2.1 and Figures 2.8-2.10), in which all the corresponding interatomic scatterings between the transition (Fe, Ni, and Cu) and the typical (Ga and Ge) metals could be

assigned to the first coordination shell. Moreover, the transition–transition and typical–typical metal scatterings were also assigned to the second coordination shell. These results suggest that Fe, Ni, and Cu occupied the Ni site of NiGa, whereas Ga and Ge were present in the Ga site. Thus, nanoparticulate HEI formed with the CsCl structure.

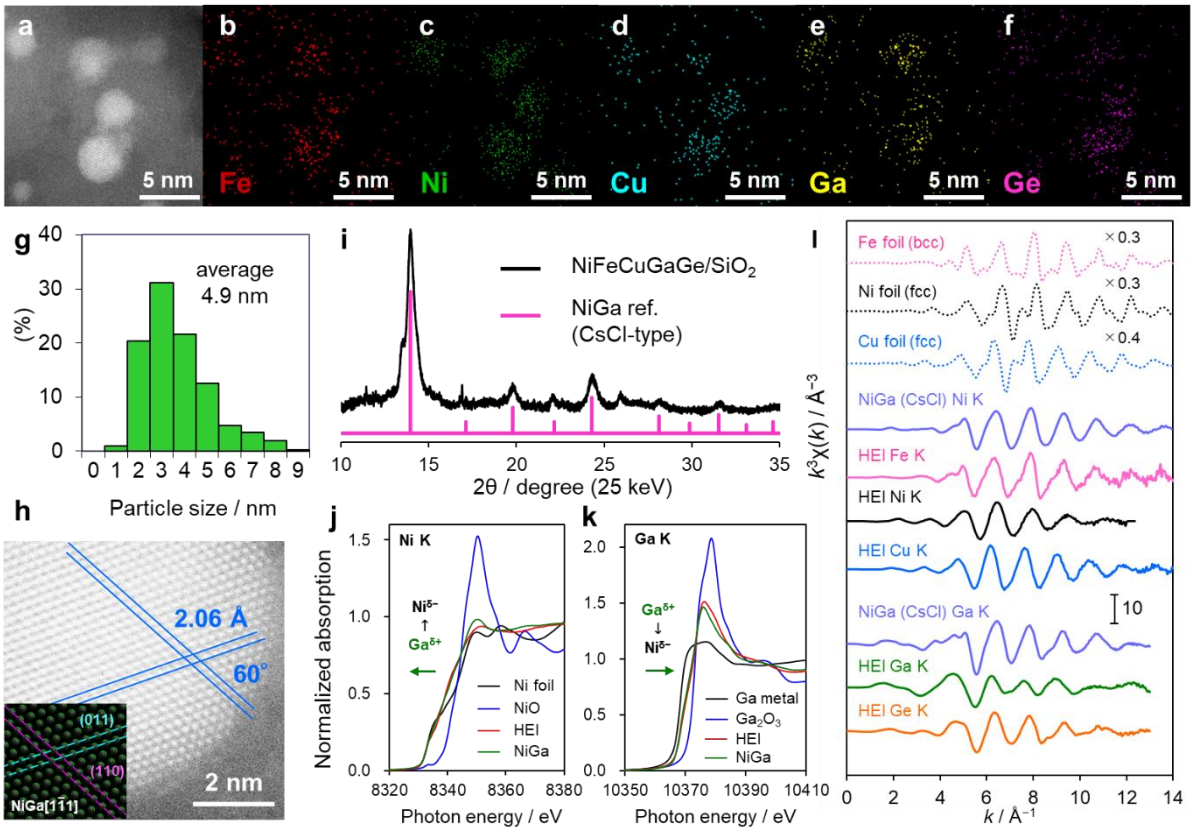

Figure 2.1 Characterization on the NiFeCuGaGe/SiO_2 (HEI): a) HAADF–STEM image, corresponding elemental maps for b) Fe, c) Ni, d) C u, e) Ga, f) Ge, g) particle size distribution, h) close-up on a single nanoparticle (the inset depicts the NiGa crystal viewed along [1$\bar{1}$1] direction), i) synchrotron X-ray diffraction (baseline subtraction was done using the diffraction data of bare SiO_2), j) Ni, and k) Ga K-edge XANES, and l) raw EXAFS oscillations.

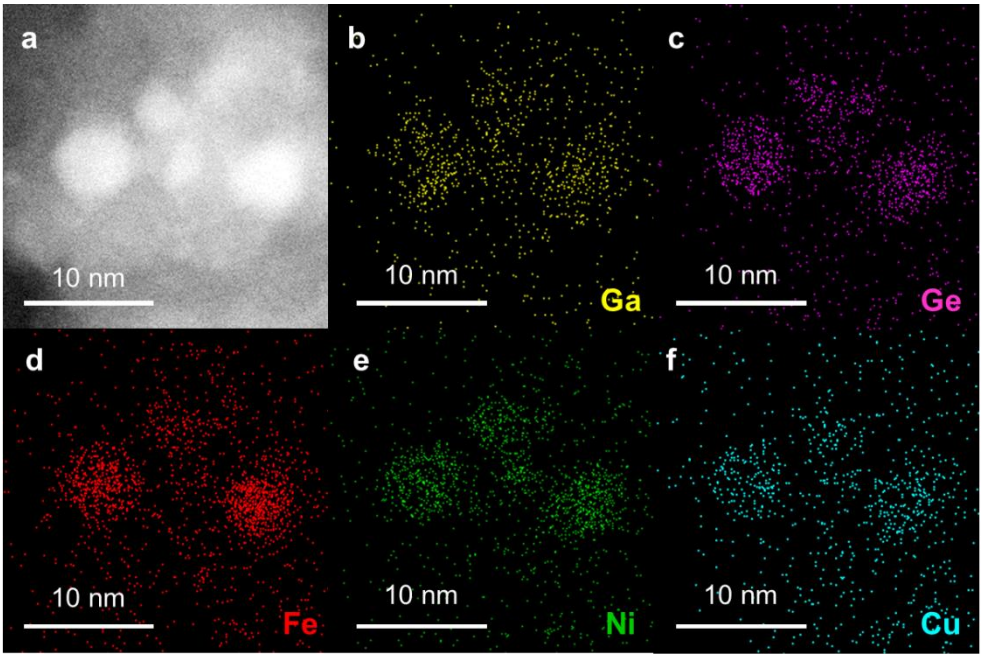

Figure 2.2 (a) HAADF–STEM image and the corresponding elemental maps for (b) Ga, (c) Ge, (d) Fe, (e) Ni, (f) Cu (magnified for a few particles).

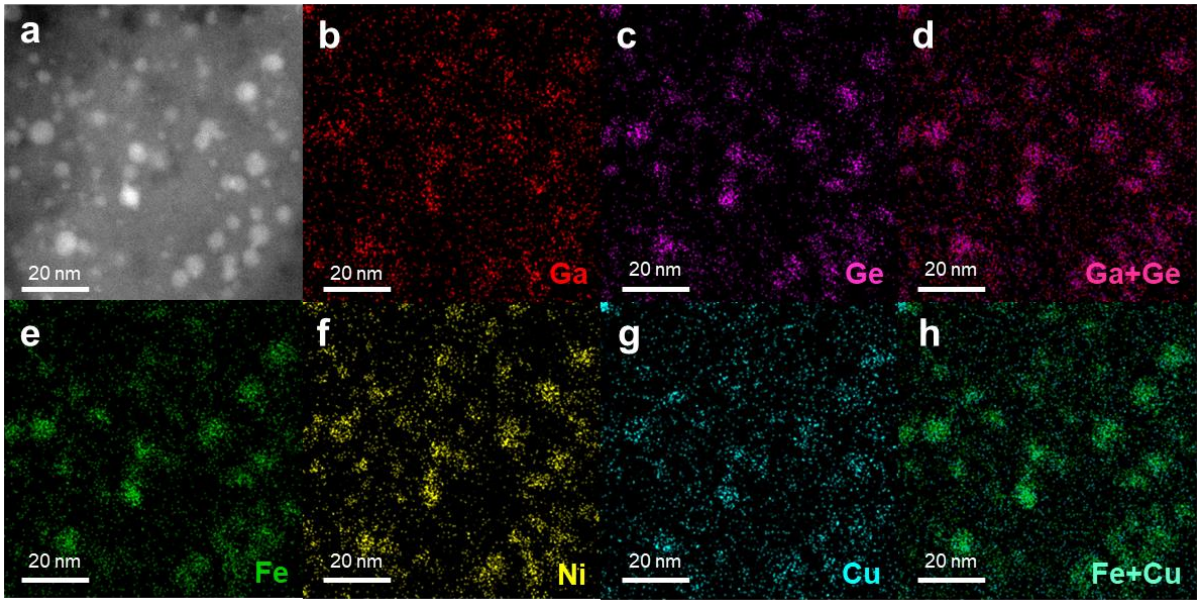

Figure 2.3. (a) HAADF–STEM image and the corresponding elemental maps for (b) Ga, (c) Ge, (d) Ga+Ge, (e) Fe, (f) Ni, (g) Cu, and (h) Fe+Cu (wider range is shown).

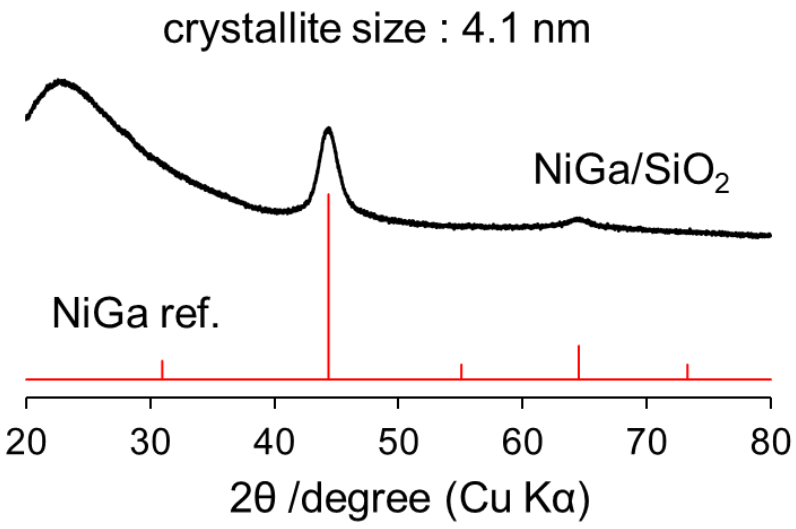

Figure 2.4. XRD pattern of $NiGa/SiO_2$.

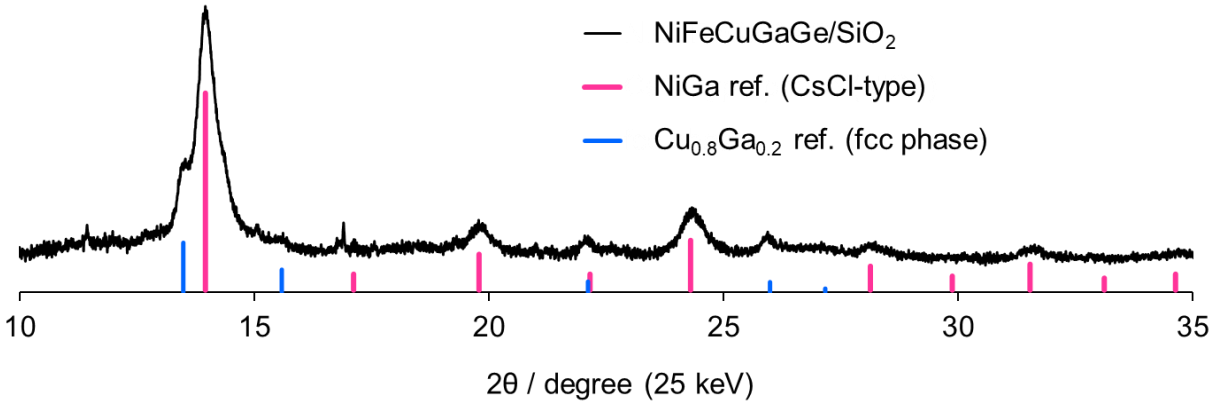

Figure 2.5. Assignments of the synchrotron XRD pattern of $NiFeCuGaGe/SiO_2$ to the reference phases.

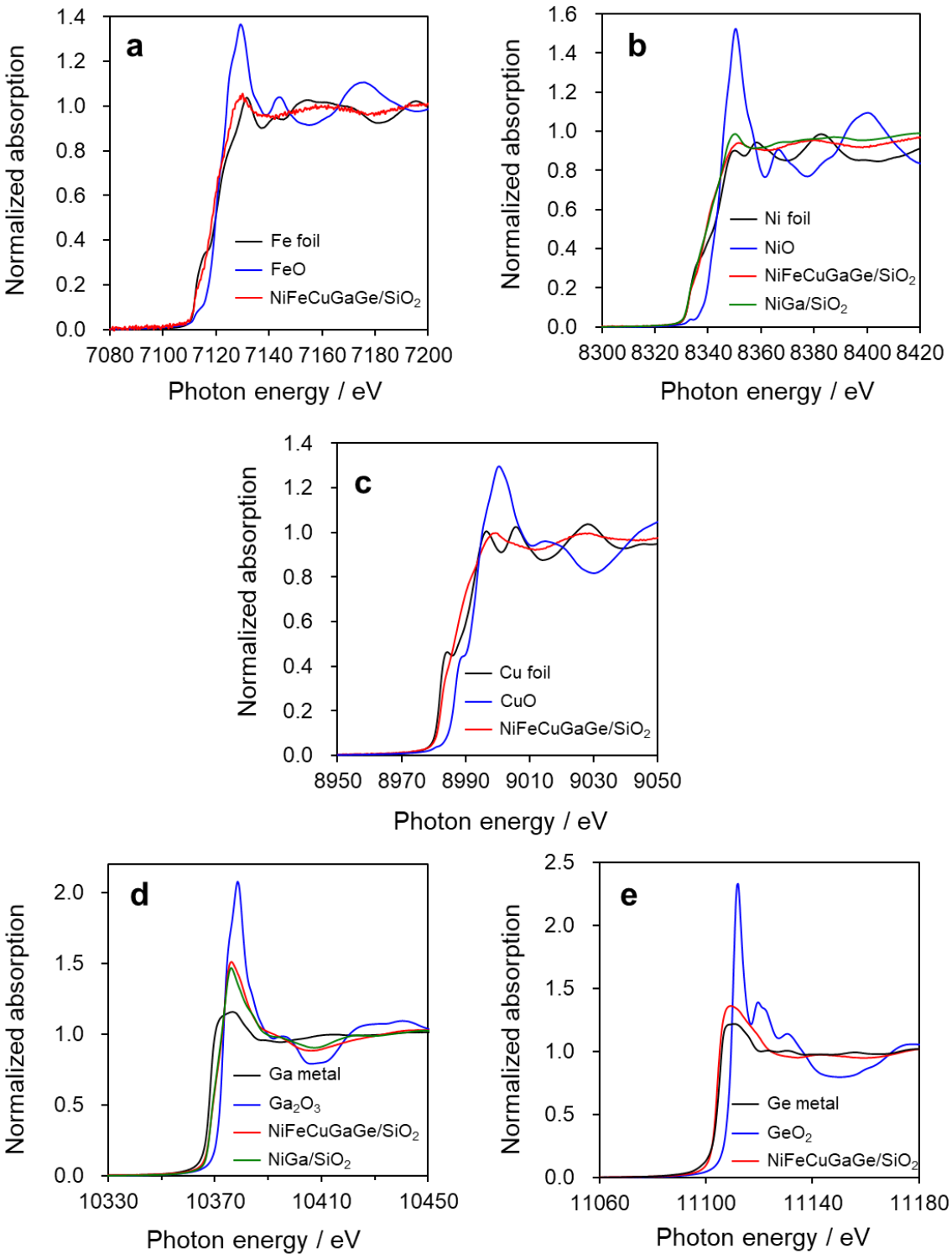

Figure 2.6. (a) Fe, (b) Ni, (c) Cu, (d) Ga, and (e) Ge K-edge XANES spectra of $NiGa/SiO_2$, $NiFeCuGaGe/SiO_2$., and reference compounds.

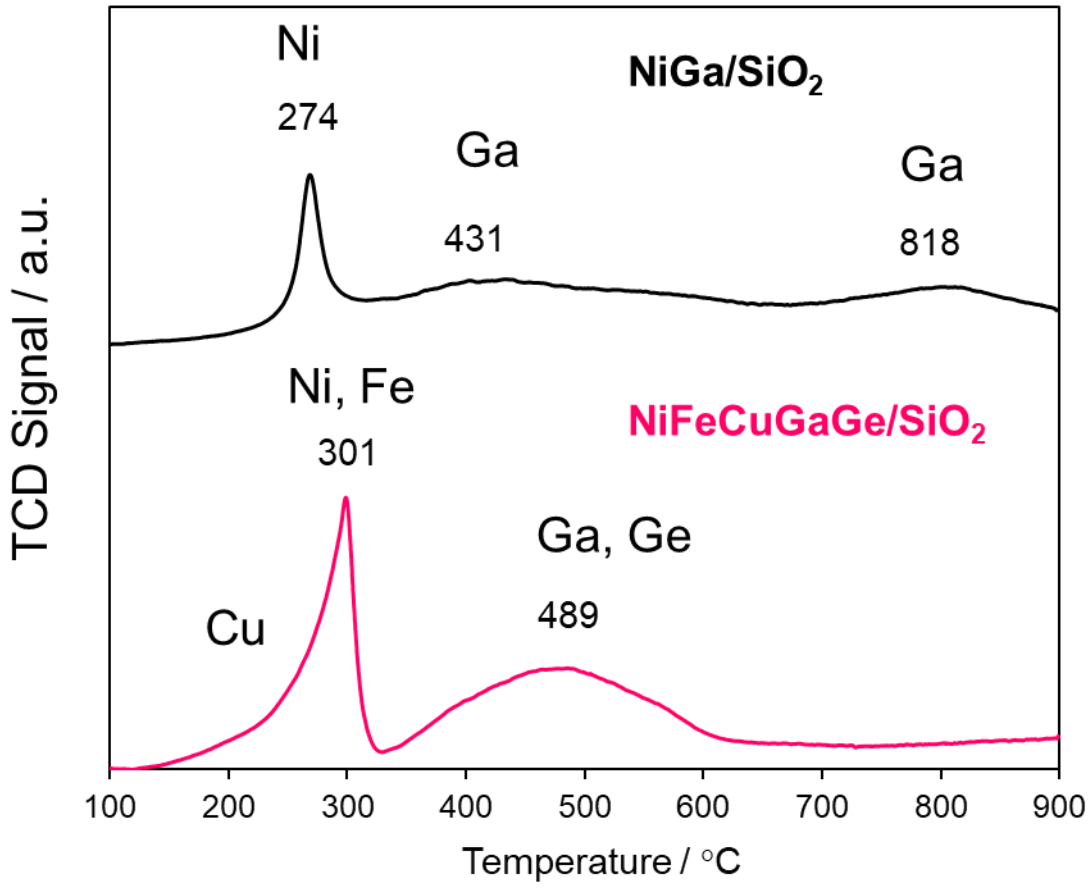

Figure 2.7. TPR profiles of $NiGa/SiO_2$ and $NiFeCuGaGe/SiO_2$. According to literature,[41] for NiGa, the reduction peaks at, 274°C, 431°C, and 818°C are assigned to the reduction of Ni^{2+}, Ga^{3+} (easily reducible), and Ga^{3+} (hardly reducible) species. Based on this result, for the HEI catalyst, the reduction peaks at 301°C and 489°C were assignable to the reduction of Ni^{2+}/Fe^{3+} and Ga^{3+}/Ge^{4+}, respectively. The reduction of Cu^{2+} can be assigned to the shoulder peak appeared at around 250°C.

Table 2.1. Results of EXAFS curve-fitting analysis.

Sample	Edge	Shell	S_0^2	*CN*	*r* (Å)	ΔE_0 (eV)	σ^2 (Å^2)	R-factor
Fe foil	Fe K	Fe–Fe	0.752	8 (fix)	2.46±0.02	−5.0±2.7	0.005	0.003
		Fe–Fe		6 (fix)	2.84±0.01		0.005	
Ni foil	Ni K	Ni–Ni	0.839	12 (fix)	2.48±0.00	7.7±0.6	0.007	0.002
Cu foil	Cu K	Cu–Cu	0.912	12 (fix)	2.54±0.00	0.3±0.6	0.009	0.002
Ga_2O_3	Ga K	Ga–O	0.929	3 (fix)	1.86±0.02	5.5±1.3	0.007	0.005
		Ga–O		3 (fix)	2.01±0.01		0.004	
GeO_2	Ge K	Ge–O	0.930	4 (fix)	1.74±0.01	5.7±2.8	0.002	0.020
NiCuFeGaGe /SiO_2	Fe K	Fe–Ga(Ge)	0.752	7.8±0.5	2.48±0.00	−7.8±0.9	0.011	0.001
		Fe–Fe(Ni,Cu)		5.9±0.4	2.99±0.01		0.042	
	Ni K	Ni–Ga(Ge)	0.839	7.6±1.0	2.41±0.01	−7.7±1.4	0.016	0.003
		Ni–Ni(Cu,Fe)		5.7±0.8	2.92±0.02		0.020	
	Cu K	Cu–Ga(Ge)	0.912	8.3±0.5	2.53±0.00	−0.9±0.8	0.013	0.002
		Cu–Cu(Ni,Fe)		6.2±0.4	3.08±0.02		0.030	
	Ga K	Ga–O	0.929	2.5±0.5	1.83±0.01	1.7±2.3	0.009	0.009
		Ga–Cu(Ni,Fe)		6.5±1.5	2.53±0.01		0.018	
		Ga–Ga(Ge)		4.9±1.1	2.99±0.01		0.037	
	Ge K	Ge–O	0.930	0.5±0.3	1.75±0.02	−1.5±1.6	0.004	0.004
		Ge–Cu(Ni,Fe)		6.2±2.42	2.42±0.01		0.015	
		Ge–Ge(Ga)		4.7±2.84	2.84±0.02		0.021	
NiGa/SiO_2	Ni K	Ni–Ga	0.879	5.6±2.46	2.46±0.00	−3.8±0.8	0.010	0.001
		Ni–Ni		4.2±3.02	3.02±0.01		0.034	
	Ga K	Ga–O	0.900	2±1.87	1.87±0.02	4.7±1.4	0.010	0.005
		Ga–Ni		5.1±2.47	2.47±0.01		0.010	
		Ga–Ga		3.8±2.94	2.94±0.02		0.019	

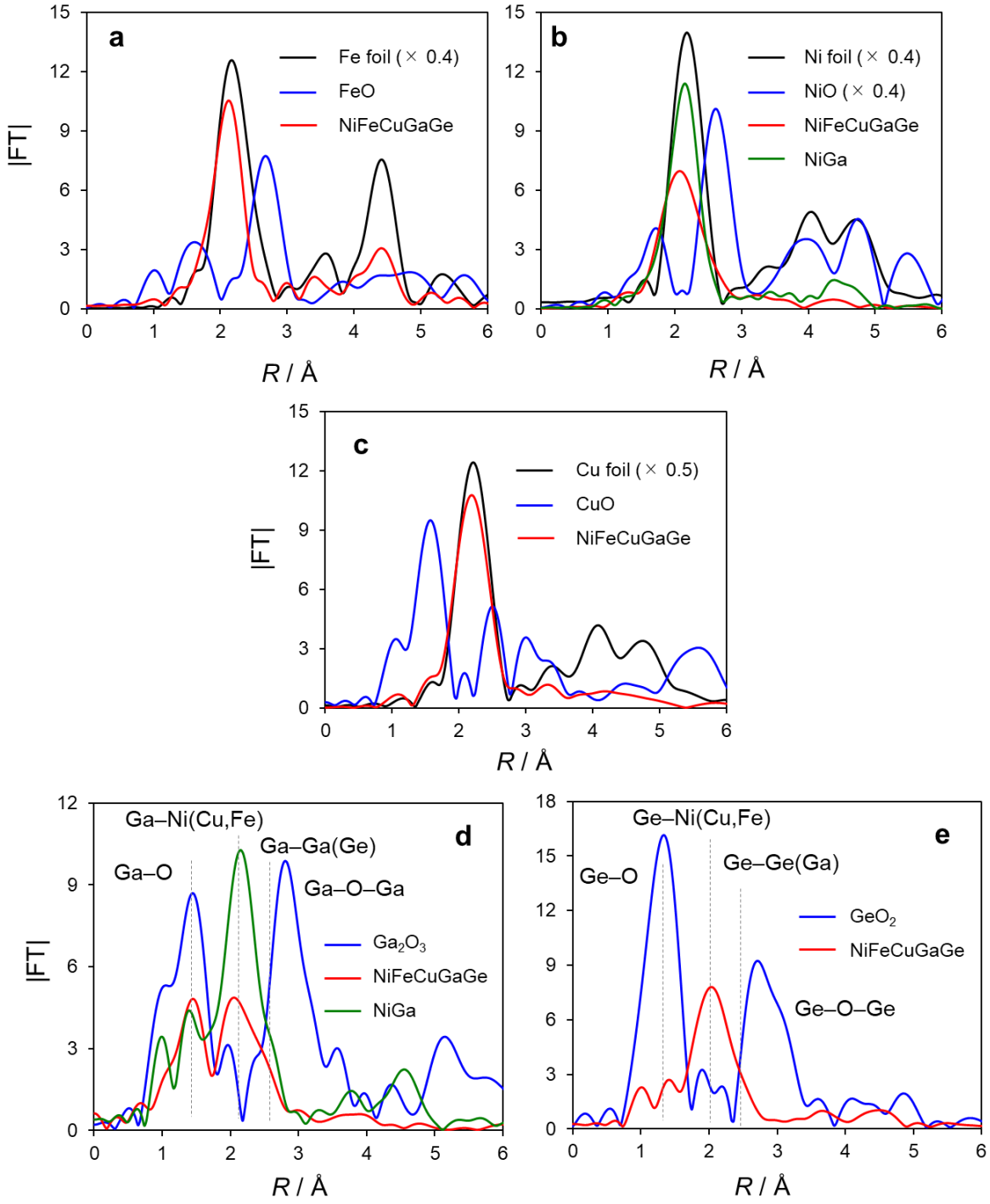

Figure 2.8. Fourier-transforms of EXAFS in (a) Fe, (b) Ni, (c) Cu, (d) Ga, and (e) Ge K-edges.

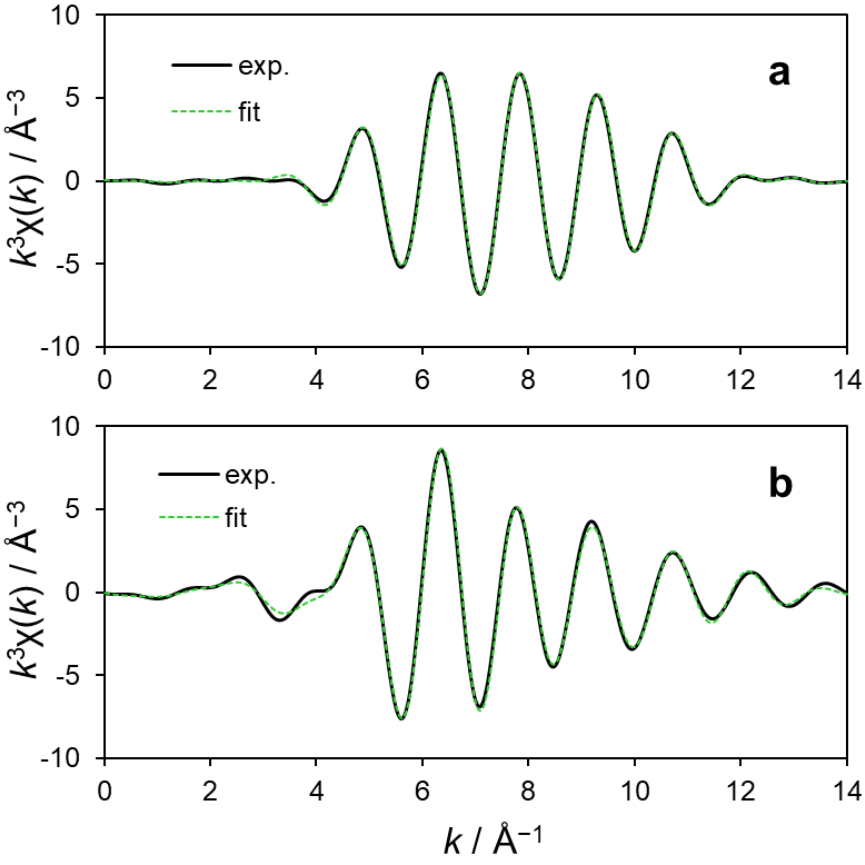

Figure 2.9. Curve-fitting results of (a) Ni and (b) Ga K-edge k^3-weighted EXAFS of NiGa/SiO_2. Solid and dashed lines indicate the results of simulation and experiment, respectively.

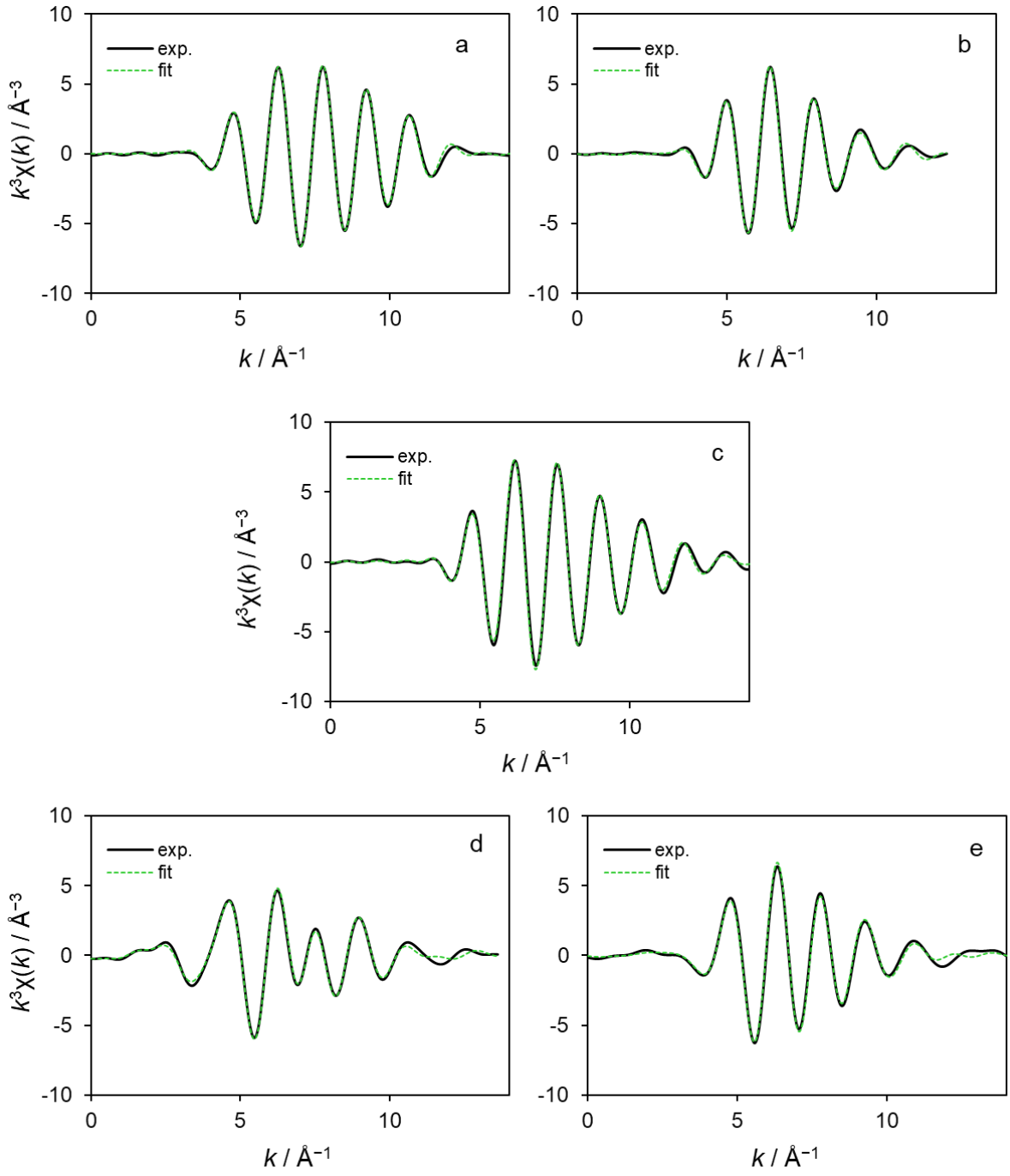

Figure 2.10. Curve-fitting results of (a) Fe, (b) Ni, (c) Cu, (d) Ga, and (e) Ge K-edge k^3-weighted EXAFS of NiFeCuGaGe/SiO_2. Solid and dashed lines indicate the results of simulation and experiment, respectively.

2.3.2 Catalytic Reactions

Next, the prepared NiGa and the HEI catalysts were then tested for acetylene semi-hydrogenation. Figure 2.11a presents the temperature dependence of C_2H_2 conversion and C_2H_4 selectivity in the absence of excess ethylene. Both catalysts showed similar trends in conversion, and the ethylene selectivity was >90% until acetylene conversion reached 100% (<170°C). Note that the Ni loading and catalyst weight of NiGa were three and two times those of HEI, respectively so that comparable acetylene conversion was obtained. Considering that the particle sizes are similar for both catalysts, the Ni-based TOF of HEI appears to be several times higher than that of NiGa. A large difference was also observed in the selectivity trend after reaching 100% conversion. Although intermetallic NiGa is a selective catalyst for this reaction, there is no information on the selectivity trend at >95% conversion. In this study, the ethylene selectivity decreased to approximately 60% after reaching 100% conversion. This is a typical trend in semi-hydrogenation chemistry, suggesting that inhibiting the over-hydrogenation of ethylene is still a difficult task when acetylene is completely consumed. On the other hand, the HEI catalyst did not show any loss of selectivity, even after reaching 100% conversion and at higher temperatures. Hence, the HEI catalyst is inactive for ethylene hydrogenation despite its remarkable activity for acetylene hydrogenation. Similar trends were also observed when the reaction was performed in the presence of excess ethylene, i.e., a model condition for ethylene purification (Figure 2.11b). Although HEI showed no loss of selectivity, a sharp decrease in selectivity (−60%) was observed for NiGa when complete acetylene conversion had been achieved. The negative selectivity suggests that semihydrogenated acetylene and co-fed ethylene were hydrogenated to ethane.[42] The temperature required for 100% conversion was shifted to a higher temperature, probably because excess ethylene competes with acetylene for adsorption on the catalyst surface. For NiGa, ethylene selectivity was recovered slightly when the temperature was higher than 230°C (Figures 2.11a and 2.11b). This can be attributed to enhanced desorption of ethylene at higher temperatures.[12,17]

A temperature-programed surface reaction (TPSR) was performed to assess the exceptional ability to inhibit the over-hydrogenation of ethylene. Figure 2.11c shows the TPSR profiles of ethylene hydrogenation over NiGa and HEI. For NiGa, ethane was produced from

100°C, and its evolution reached a maximum at 200°C and higher, highlighting the intrinsic activity of NiGa for ethylene hydrogenation. On the other hand, no ethane was detected up to 300°C when HEI was used. This is the first report of the complete inhibition of ethylene over-hydrogenation using a Ni-based material to the best of our knowledge. The high selectivity upon the complete conversion of acetylene over a wide temperature range is desirable for practical applications. Although no over-hydrogenation of ethylene was confirmed in ethylene hydrogenation, only a small quantity of ethane (typically, <5% selectivity) was detected over a wide range of conversions and temperatures during acetylene semi-hydrogenation. This might be because the direct hydrogenation of acetylene to ethane occurred via a surface ethylidene intermediate.[101] TPSR was also performed with ethylene alone to evaluate the C–C cracking behavior. NiGa generated methane at 230°C and higher, whereas no methane was formed on HEI (Figure 2.12), suggesting that HEI does not catalyze C–C cracking in this temperature region. The long-term stability of the HEI catalyst was then tested. High acetylene conversion (99.8%) and ethylene selectivity (95%–98%) were retained for at least 28 h at 190°C (Figure 2.11d, see Figure 2.13 for the corresponding result in the presence of excess ethylene). Moreover, no green oil, C1, or C4 hydrocarbons were formed during the long run. We further performed control experiments using quaternary intermetallic catalysts such as (NiFe)(GaGe)/SiO_2, (NiCu)(GaGe)/SiO_2, and (NiFeCu)Ga/SiO_2 (Figure 2.14) to demonstrate the need of the five elements. All the quaternary catalysts showed lower catalytic activity and stability. This indicates that the isolation by Fe/Cu and the Ge doping are necessary for greater stability, probably due to the site-isolation and enhanced entropy effects.

The catalytic performance of HEI was compared with those of 3d transition metal-based catalysts reported elsewhere with respect to the specific activity and ethylene selectivity at high acetylene conversion (>90%, Figure 2.11e; see Table 2.2 and Figure 2.15 for details and the complete list).[3,17,19,20,24,26,28,30,44,45] As a universal and practical scale for activity, this study used milliliters of converted acetylene per minute per gram of active metal. In the literature,[17] NiGa/LDH showed the highest activity among the 3d-transition metal-based catalysts that showed >80% ethylene selectivity (216 $mL_{C2H2}min^{-1}g_{Ni}^{-1}$; similar activity was achieved using the present NiGa/SiO_2, 167 $mL_{C2H2}min^{-1}g_{Ni}^{-1}$). The HEI catalyst exhibited approximately five

times higher activity than NiGa/LDH (1000 $mL_{C2H2}min^{-1}g_{Ni}^{-1}$) with excellent selectivity. Thus, remarkably high catalytic activity and selectivity were achieved using Ni in a catalyst design based on HEI.

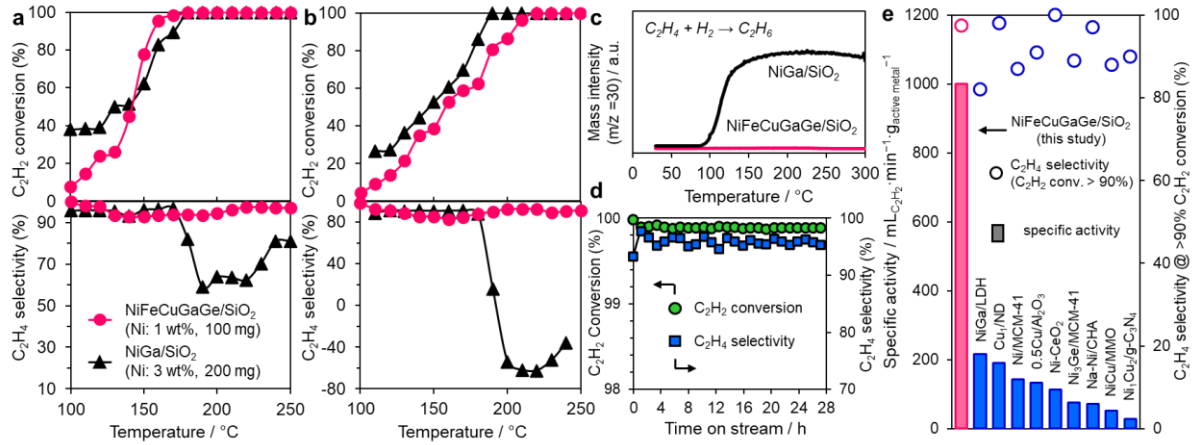

Figure 2.11. Catalytic performance of $NiGa/SiO_2$ and $NiFeCuGaGe/SiO_2$ (HEI) in acetylene semi-hydrogenation. C_2H_2 conversion and C_2H_4 selectivity in the a) absence (C_2H_2: H_2: He = 1: 10: 39 $mLmin^{-1}$) and b) presence of excess ethylene (C_2H_2: H_2: C_2H_4: He = 1: 10: 10: 39 $mLmin^{-1}$). c) Temperature-programmed surface reaction profiles for ethylene hydrogenation. d) Long-term stability test using HEI/SiO_2. e) Comparison with 3d transition metal-based selective semi-hydrogenation catalysts in the literature. Catalysts showing >80% selectivity at >90% conversion are listed for visibility (other data is shown in Table 2.2 and Figure 2.15).

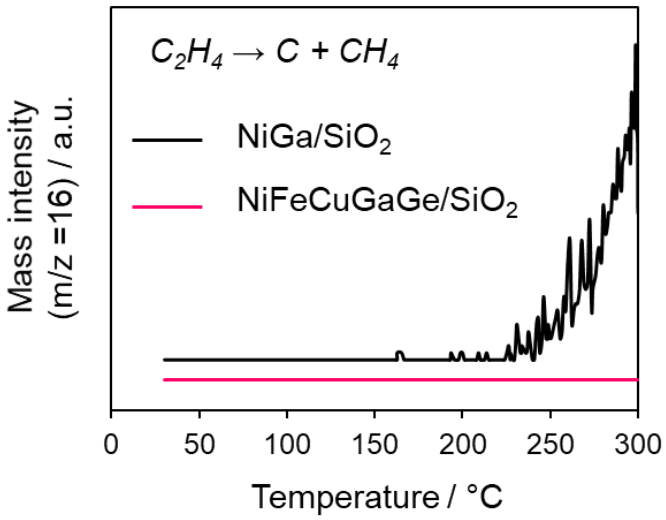

Figure 2.12. TPSR profiles of ethylene cracking over $NiGa/SiO_2$ and $NiFeCuGaGe/SiO_2$.

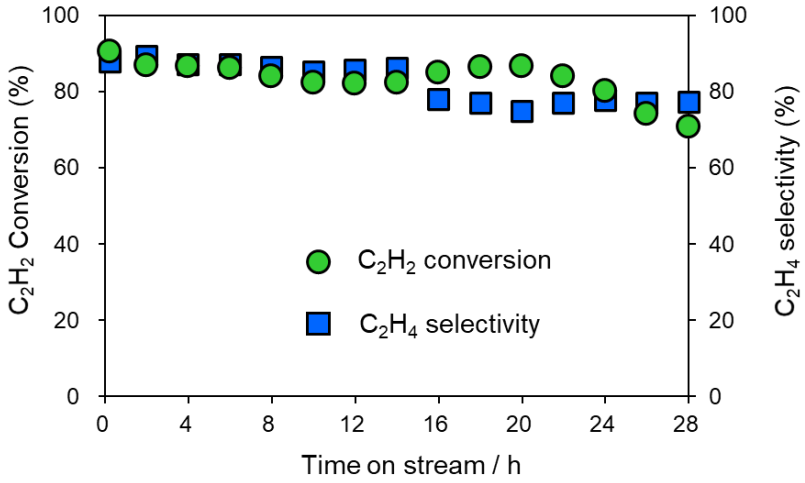

Figure 2.13. Long-term stability test using NiFeCuGaGe/SiO_2 in the presence of excess ethylene at 180°C. Although slight deactivation was observed after 20 h, it might be attributed to the presence of a small amount of impurity (higher hydrocarbons) in ethylene feed, because no deactivation occurred when only acetylene was used.

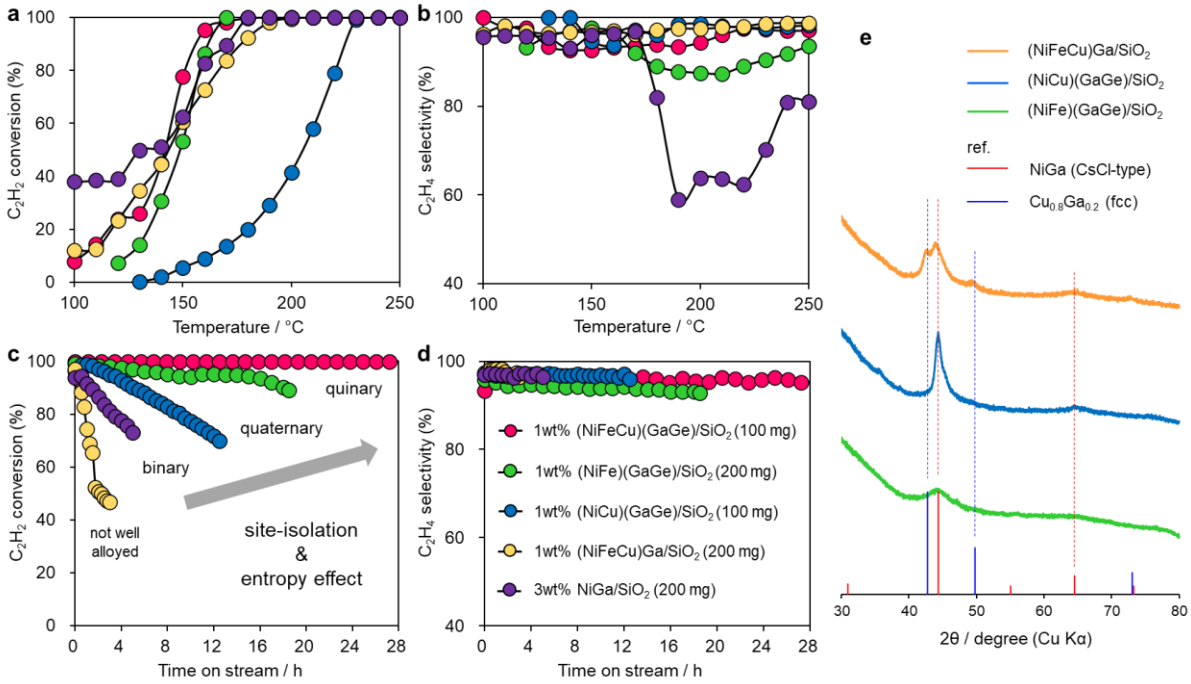

Figure 2.14. Control experiments using NiGa and the corresponding quaternary intermetallics. Temperature dependence of (a) acetylene conversion and (b) ethylene selectivity, and time-course of (c) acetylene conversion and (d) ethylene selectivity in long-term stability tests. (e) XRD patterns of the quaternary alloys showing that (NiCu)(GaGe) and (NiFe)(GaGe) were well alloyed but (NiFeCu)Ga was not. Since (NiFe)(GaGe)/SiO_2, (NiFeCu)Ga/SiO_2 and NiGa/SiO_2 showed lower activity, twice catalysts were used. The stability tests were done at

190°C, 160°C, 225°C, 180 °C and 200 °C for (NiFeCu)(GaGe)/SiO_2, (NiFe)(GaGe)/SiO_2, (NiCu)(GaGe)/SiO_2, (NiFeCu)Ga/SiO_2, and NiGa/SiO_2 respectively, to obtain >90% conversions. The stability of NiGa/SiO_2 in this study was lower than that in the previous report.[46] This was probably due to the size of nanoparticles; this study: 4 nm, the reported: 10 nm. Our NiGa catalyst may have a much larger fraction of edge/step sites than the reported, which trigger undesired side reactions causing deactivation such as oligomerization. (NiCu)(GaGe) and (NiFe)(GaGe) showed intermediate stability between NiGa and HEI (NiGa < (NiCu)(GaGe) < (NiFe)(GaGe) < HEI), which may be due to not only the higher selectivity by the site-isolation effect but also the greater stability of alloy nanoparticles by the entropy effect (**c**). The lower stability of (NiCu)(GaGe) than that of (NiFe)(GaGe) is probably due to the much higher reaction temperature (225°C > 160°C). The significantly low stability of (NiFeCu)Ga may be due to the insufficient alloying as shown in (**e**). This is probably due to the intrinsic low miscibility of the Fe–Cu[47] system, contrary to the Ni–Cu[48] and Ni–Fe[49] systems. Considering that the Ni site of (NiFeCu)(GaGe) HEI was well alloyed, the multi-metallization of the Ge site might have enhanced the alloying of Ni, Fe, and Cu at the Ni sites. Thus, the order of the catalyst stability can be reasonably explained when the entropy effect is also considered. Moreover, these results indicate that the five elements are necessary not only for high selectivity and stability, but also for well alloying of all constituent metals owing to the entropy effect. The ethylene selectivity at the complete acetylene conversion increased in the following order: NiGa << (NiFe)(GaGe) < Cu-containing catalysts (**b**). This result suggests that alloying Ni with Cu is more effective than that with Fe to inhibit over-hydrogenation of ethylene. However, Fe is still necessary to obtain better performance due to site-isolation and the entropy effect.

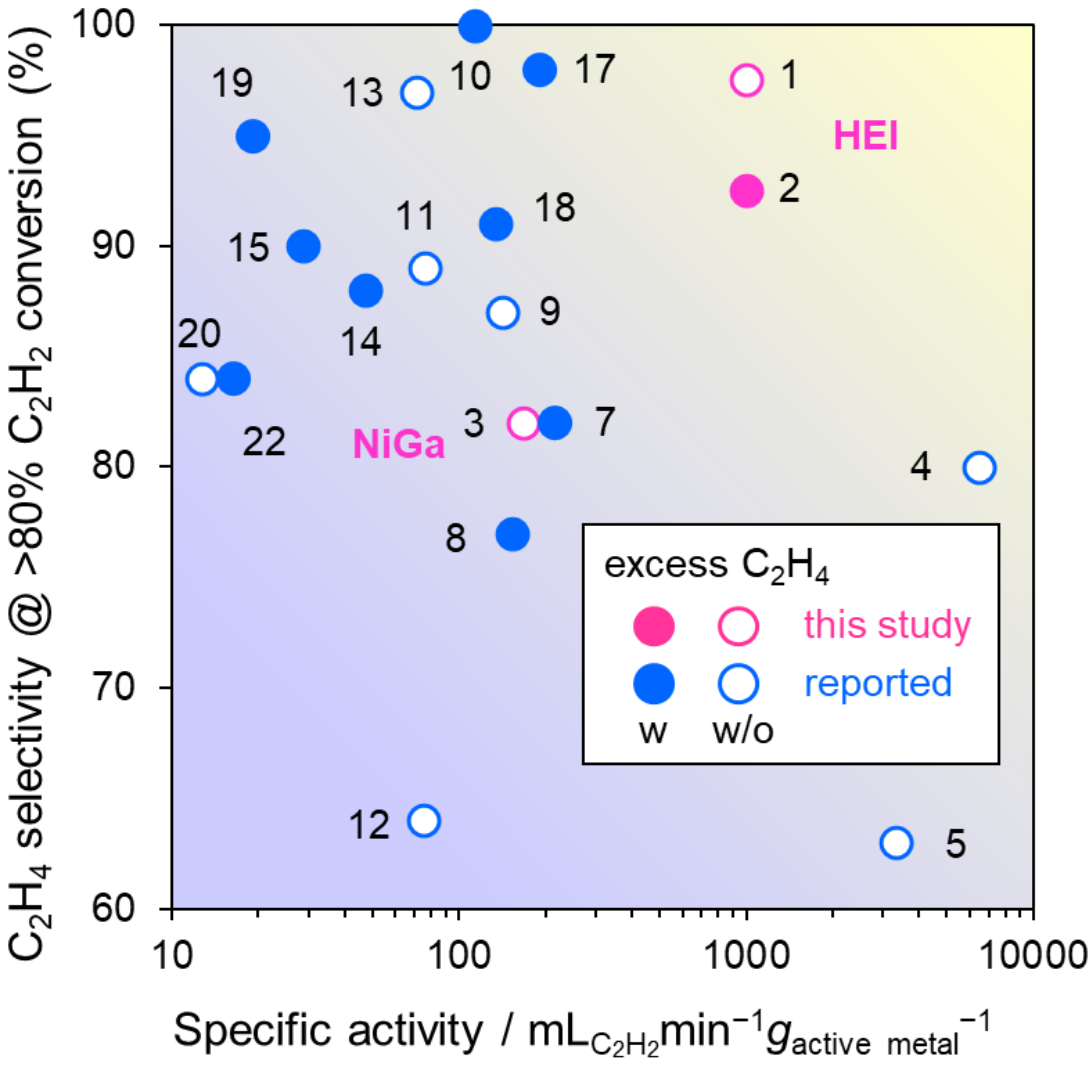

Figure 2.15. Relationship between the specific activity and ethylene selectivity at high acetylene conversion (>80%) for 3d transition metal-based catalysts that were reported in literature and developed in this study. Numbers correspond to the entries in Table 2.2. Our NiGa/SiO_2 catalyst (3) showed similar activity and selectivity to those of NiGa/MgAl-LDH (7), indicating that the catalytic performance of intermetallic NiGa was well reproduced.

Table 2.2. Summary of reaction conditions and catalytic performances in acetylene semi-hydrogenation using 3d transition metal-based catalysts that were reported in literature and developed in this study.

entry	catalyst	loading (wt%)	amount / mg	C_2H_2 flow /mLmin^{-1}	$C_2H_2 : H_2 : C_2H_4$	total flow /mLmin^{-1}	GHSV mLg^{-1}h^{-1}	/conv. (%)	sel. (%)	temp. / °C	specific rate [a]	ref
1	NiCuFeGaGe/SiO_2	1	100	1	1 : 10 : 0	50	30000	100	98	220	1000	this work
2	NiCuFeGaGe/SiO_2	1	100	1	1 : 10 : 10	50	30000	100	93	220	1000	this work
3	NiGa/SiO_2	3	200	1	1 : 10 : 0	50	15000	100	82	180	167	this work
4	Si–Ni–Zn/SiO_2	2	15	2	1 : 10 : 0	32	128000	97	80	200	6467	[50]
5	$NiCu_{0.125}$/MCM-41 [b]	1	100	3.3	1 : 3 : 0	13.3	8000	100	63	250	3333	[51]
6	$AgNi_{0.125}/SiO_2$ [b]	0.37	30	0.3	1 : 20 : 59	30	60000	98	25	200	2649	[52]
7	NiGa/MgAl-LDH	10	50	1.2	1 : 10 : 20	120	144000	90	82	190	216	[47]
8	$Ni_3Ga/MgAl_2O_4$	2	100	0.33	1 : 20 : 100	67	40000	92	77	220	153	[53]
9	Ni/MCM-41	25	100	3.7	1 : 2 : 0	66.6	40000	96	87	240	142	[54]
10	Ni–CeO_2	1.54	200	0.35	1 : 70 : 4	70	21000	100	100	200	114	[55]
11	Ni_3Ge/MCM-41	3.2	1500	3.9	1 : 2.1 : 0	29	1160	94	89	250	76	[56]
12	Ni_6In/SiO_2	8	500	3	1 : 10 : 0	300	36000	100	64	200	75	[57]
13	Na-Ni/CHA	3.5	200	0.5	1 : 16 : 0	50	15000	100	97	170	71	[58]
14	NiCu/MgAl-MMO[b]	9.58	100	0.558	1 : 2 : 103	166	100500	81	88	140	47	[59]
15	Ni_1Cu_2/g-C_3N_4 [b]	3.5	150	0.15	1 : 10 : 50	30	12000	100	90	160	29	[60]
16	Ni-SAs/N-C	5.67	400	0.2	1 : 20 : 100	40	6000	96	91	200	8	[61]
17	Cu1/ND	0.25	200	0.1	1 : 10 : 20	10	3000	95	98	200	190	[62]
18	0.5Cu/Al_2O_3	0.5	300	0.2	1 : 10 : 50	20	4000	100	91	188	133	[63]
19	Cu/$Fe_{0.16}MgO_x$ [c]	18.0	200	0.69	1 :100 : 3	209	62700	100	95	215	19	[64]
20	$Cu(OH)_2$	78.9	100	1	1 : 9 : 0	10	600	100	84	110	13	[65]
21	Cu_2O	88.8	100	0.045	1 : 22 : 197	10	6000	100	64	120	0.5	[66]
22	$Al_{13}Fe_4$	38.9	20	0.15	1 : 10 : 100	30	90000	85	84	200	16	[67]
23	Co_2FeGe [d]	47.8	400	0.03	1 : 400 : 100	30	4500	91	90	200	0.1	[68]

[a] Unit: $mL_{C_2H_2}$ min^{-1} $g_{\text{active metal}}^{-1}$. [b], [c] , [d] Ni (b), Cu (c), Co (d) were regarded as the main active metal, respectively.

2.3.3 Mechanistic study

Then, a kinetic study was conducted to obtain insight into the effects of HEI on the reaction mechanism. The apparent activation energies (E_a) of acetylene semi-hydrogenation were obtained using Arrhenius-type plots. HEI showed a much lower E_a than NiGa (40.4 and 55.1 kJ mol^{-1}, respectively; Figure 2.16). This result is consistent with the significantly enhanced catalytic activity by multi-metallization. The reaction orders of acetylene (P_{C2H2}) and hydrogen (P_{H2}) pressures were −0.91 and 2.27, respectively, for NiGa (Figure 2.17). The negative order of P_{C2H2} suggests that strong acetylene adsorption prevents hydrogen adsorption. The largely positive order of P_{H2} indicates that hydrogen adsorption (i.e., the appearance of vacant active sites) makes a large contribution to the overall reaction rate for NiGa. A similar trend in the reaction orders ($P_{C2H2} < 0$, $P_{H2} > 1$) has also been reported.[69] However, the reaction orders for HEI were significantly different: −0.13 (P_{C2H2}) and 0.80 (P_{H2}) (Figure 2.17). P_{C2H2} increased to near zero, whereas P_{H2} decreased significantly to below unity. This change suggests that acetylene adsorption was weakened by multi-metallization to facilitate hydrogen adsorption to the surface. Based on these results, the significant increase in catalytic activity was attributed to the following two factors: (1) decrease in the energy barrier of semi-hydrogenation and (2) enhanced supply of hydrogen to the surface, both of which were enabled by multi-metallization in the HEI framework.

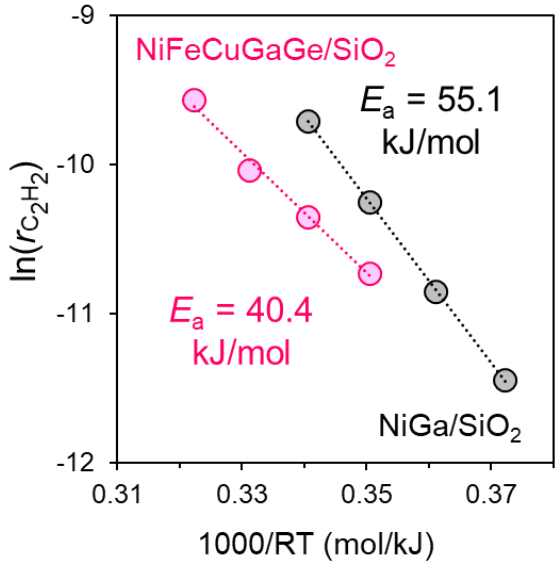

Figure 2.16. Arrhenius-type plots obtained from acetylene semi-hydrogenation over $NiGa/SiO_2$ and $NiFeCuGaGe/SiO_2$.

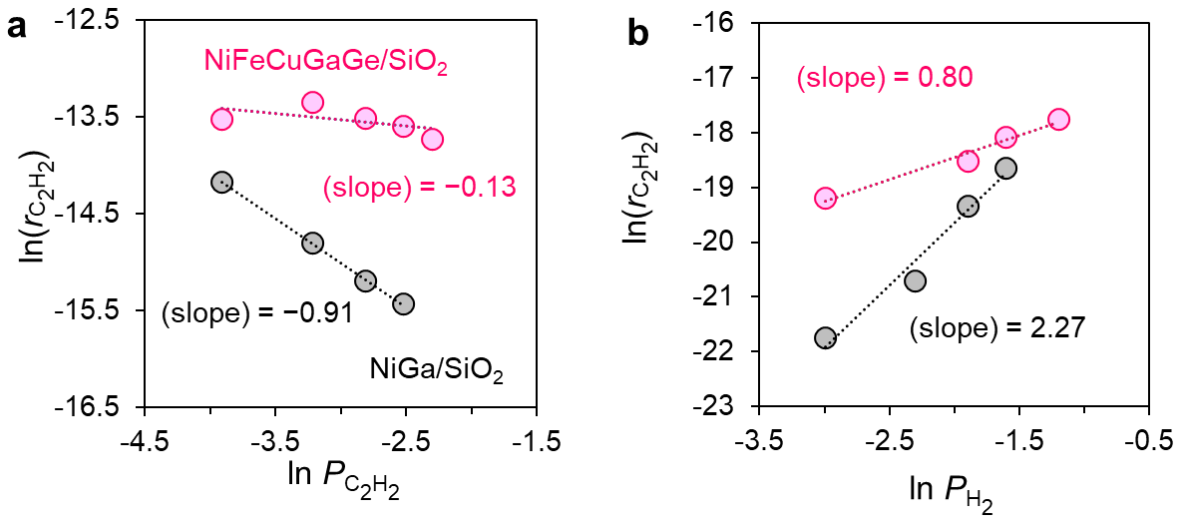

Figure 2.17. Reaction orders of (a) acetylene ($P_{C_2H_2}$) and (b) hydrogen (P_{H_2}) pressures in acetylene semi-hydrogenation over NiGa/SiO_2 and NiFeCuGaGe/SiO_2.

2.3.4 DFT calculation

Finally, we performed a density functional theory (DFT) study to understand the roles of multi-metallization on the enhanced activity and selectivity on an atomic scale. First, a NiGa–(2×2×2) supercell was constructed as a parent structure for multi-metallization (Figure 2.18a). Note that, the z-axis of the supercell corresponds to the [110] direction of the primitive cell of NiGa so that the resulting slab model exposes the most stable (110) plane to the vacuum space. The Ni and Ga sites in the parent model were substituted partially and randomly to Fe/Cu and Ge, respectively (see Computational details for further details in modeling). Five bulk structures of HEI with different elemental distribution in each of the Ni and Ga sites (twenty slab models with different surface layers) were modeled to understand the influence of the elemental distribution on the surface properties (Figure 2.19). The surface energies of the HEI (110) plane were 1.48–1.65 Jm^{-2} for the twenty different models (Figure 4b, see Figure 2.20a for the individual values), in which the standard deviation was only 0.04 Jm^{-2}, indicating the elemental distribution had little influence. Interestingly, the surface energies of HEI were much lower than that of NiGa, probably due to surface relaxation upon the multi-metallization. Then, the adsorption energy (E_{ad}) of ethylene was considered for twenty different Ni sites of HEI (Figure 2.20b). Although E_{ad} differed to some extent depending on the microenvironment of the Ni sites, they all were less negative than −0.30 eV (average: −0.11 eV, Figure 2.18b, see Figure

2.20b for individual values). These values were remarkably less negative than that for NiGa (−0.64 eV), reflecting the significantly weaker adsorptivity of Ni in HEI. Hence, the loss of surface energy is one of the key origins of the weak adsorptivity.

We subsequently focused on the hydrogenation of acetylene to ethane using the slab model that showed the closest E_{ad} of ethylene to the average. First, the potential energy diagram of hydrogen atom diffusion along the Fe–Ni–Cu column was calculated to understand the favorable location of hydrogen (Figure 2.21). The top site of Fe was the most stable for hydrogen atom adsorption, followed by the Fe–Ni bridge and Ni top sites, whereas the Cu sites were energetically unfavored. Therefore, hydrogen attacks the adsorbates on the Ni site from the Fe–Ni side as a likely direction of hydrogenation (Figure 2.18c, see Figures 2.22-2.24 for the other structures and comprehensive energy diagrams). HEI provided a lower energy barrier (E_A) for acetylene semi-hydrogenation (hydrogen attack to C_2H_2 or C_2H_3) than NiGa, which is consistent with the experimental results (Figure 2.18d). Then, we compared ethylene desorption and over-hydrogenation to evaluate the selectivity to ethylene (Figure 2.18e).

For NiGa, although the electronic energy of desorption was higher than that of over-hydrogenation, an opposite trend was observed in the Gibbs free energy because of the large contribution of translational entropy in gaseous ethylene.[70,71] The free energy change in desorption (ΔG_{des}) was slightly positive (0.05 eV) and much lower than the free energy barrier of over-hydrogenation (ΔG_{oh}, 0.43 eV), which reproduced the reported values for NiGa. On the other hand, ΔG_{des} of HEI was significantly negative (−0.51 eV) because of the low adsorptivity of HEI. Moreover, ΔG_{oh} increased upon multi-metallization (0.50–0.64 eV), resulting in a large difference in ΔG_{des} and ΔG_{oh} (1.15 eV). Hence, the HEI surface allows the fast desorption of ethylene but does not facilitate over-hydrogenation, thereby allowing the highly selective semi-hydrogenation of acetylene without over-hydrogenation. We further calculated the side reaction path via an ethylidene intermediate to evaluate the possibility of direct hydrogenation pathways of acetylene to ethane (Figures 2.25-2.29). E_A of ethylidene ($CH–CH_3$) formation from vinyl ($CH=CH_2$) was much higher than that of ethylene formation (NiGa (110): 0.84 eV > 0.45 eV, HEI(110): 1.20 eV > 0.30 eV), indicating that this pathway is unlikely to occur on the terrace site. However, much lower E_A of 0.42 eV was obtained when

the reaction occurred on a step site of NiGa(210). Therefore, it is likely that a small fraction of step sites triggers the direct hydrogenation path.

We also considered the effect of electronic state on the enhanced catalytic performance of HEI. Figure 2.18f shows the density of states (DOS) projected on the d orbitals of NiGa and HEI. The DOS profile of HEI could be deconvoluted into contributions from Fe, Ni, and Cu atoms, of which the contribution of Ni matched the DOS profile of NiGa. Hence, the electronic structure of Ni itself did not change upon multi-metallization, i.e., a negligible ligand effect from Fe/Cu. Therefore, the significantly enhanced catalytic performance of HEI was attributed to geometric effects from multi-metallization (Ni isolation and surface relaxation) but not to electronic effects.

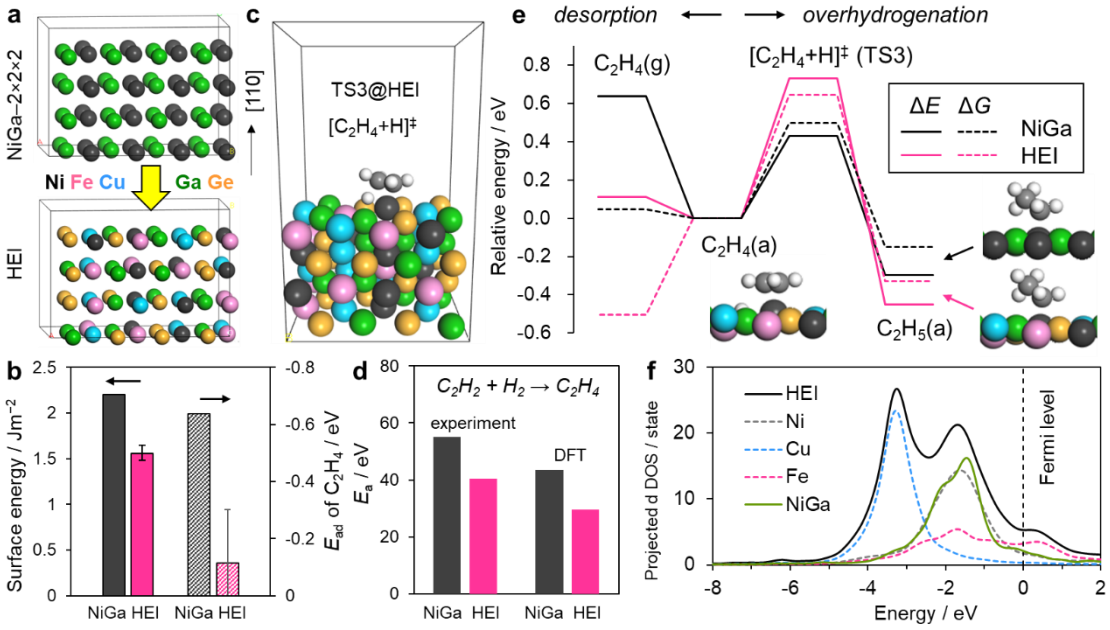

Figure 2.18. DFT calculations for the (110) surfaces of NiGa and (NiFeCu)(GaGe) HEI. a) Optimized bulk structures of the parent NiGa supercell and the HEI model. b) Surface energy and adsorption energy of ethylene on Ni sites. c) An example of a TS image: hydrogen attack to C_2H_2 on HEI. d) E_a of acetylene hydrogenation. e) Energy diagrams of ethylene desorption and overhydrogention. f) Profiles of density of states (DOS) projected on d orbitals. The dotted line indicates the partial d DOS of HEI projected on each transition metal.

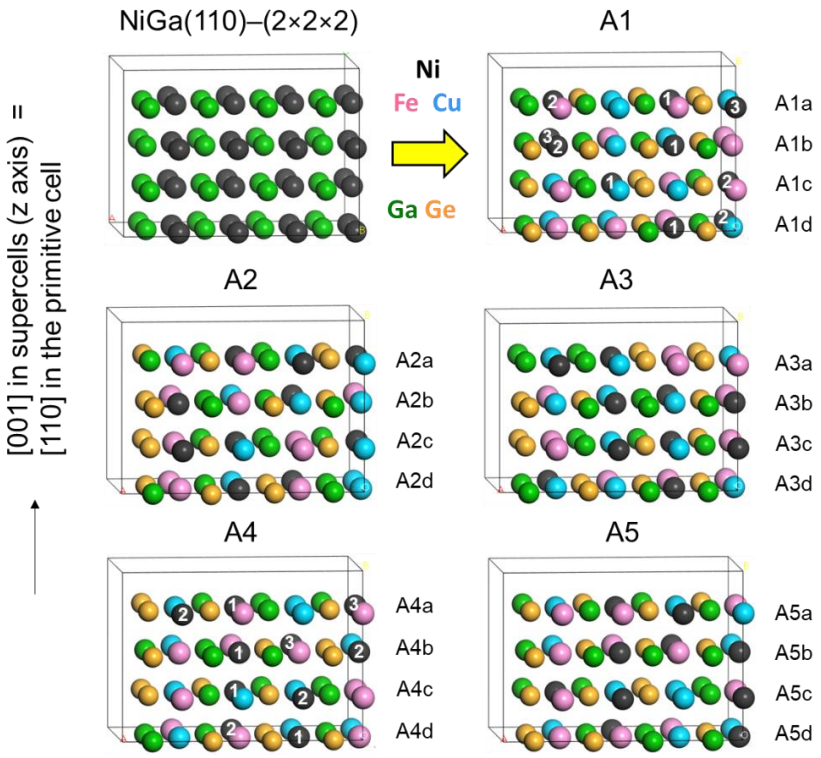

Figure 2.19. Bulk structure of NiGa(110)–(2×2×2) and the corresponding HEI models with five different atomic distribution (A1–A5). Each bulk model has four (110) layers with different local environments. Twenty different slab models were generated so that each (110) layer was exposed to the vacuum space (A1a–A5d). Numbers in A1 and A4 indicate the Ni site used for calculating E_{ad} of ethylene on isolated Ni.

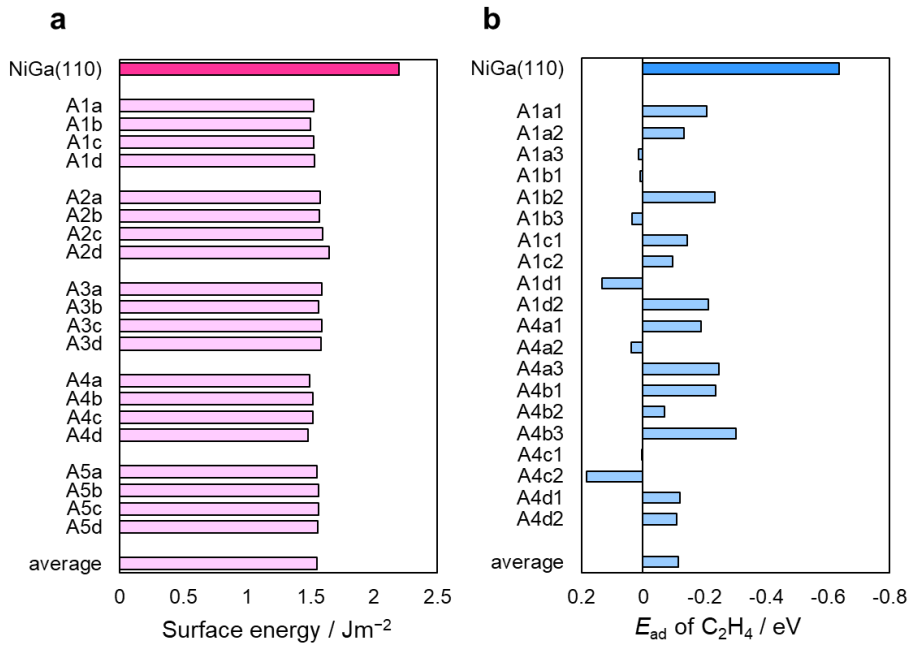

Figure 2.20. (a) Surface energy of (110) planes of NiGa and HEI. (b) E_{ad} of ethylene on Ni sites of HEI with A1 and A4 conformations. Positive E_{ad} values were regarded as zero when estimating the average of E_{ad}.

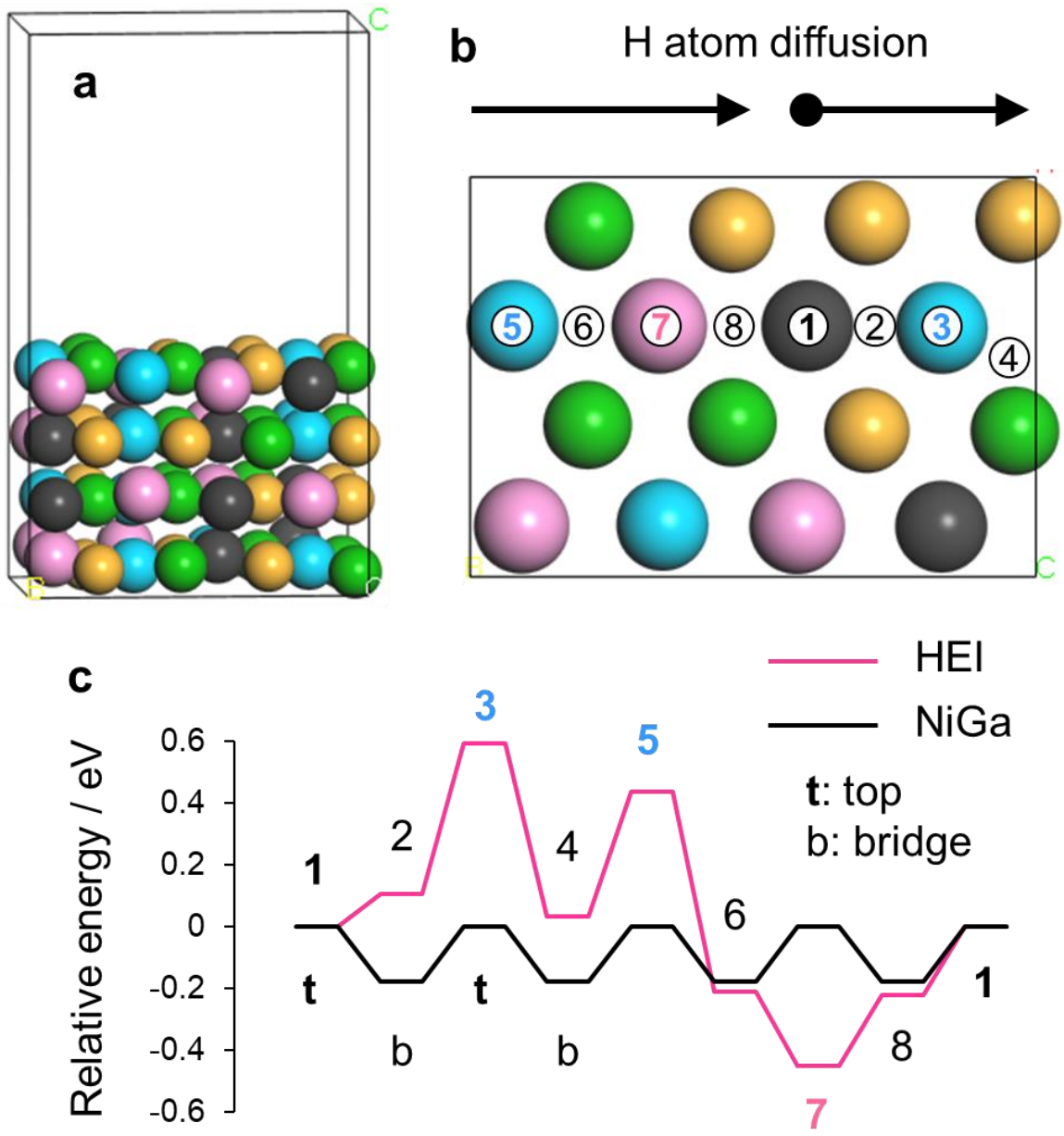

Figure 2.21. (a) The slab structure of A4d conformation. (b) surface diffusion pathway of hydrogen atom on the (110) surface of HEI (A4d). (c) Energy diagrams of hydrogen diffusion on the (110) surface of NiGa and HEI (A4d). Numbers in b and c indicate the stationary adsorption site for atop and bridge fashion. The Cu–Cu site (4) exceptionally favored the Cu_2Ga hollow site for hydrogen adsorption.

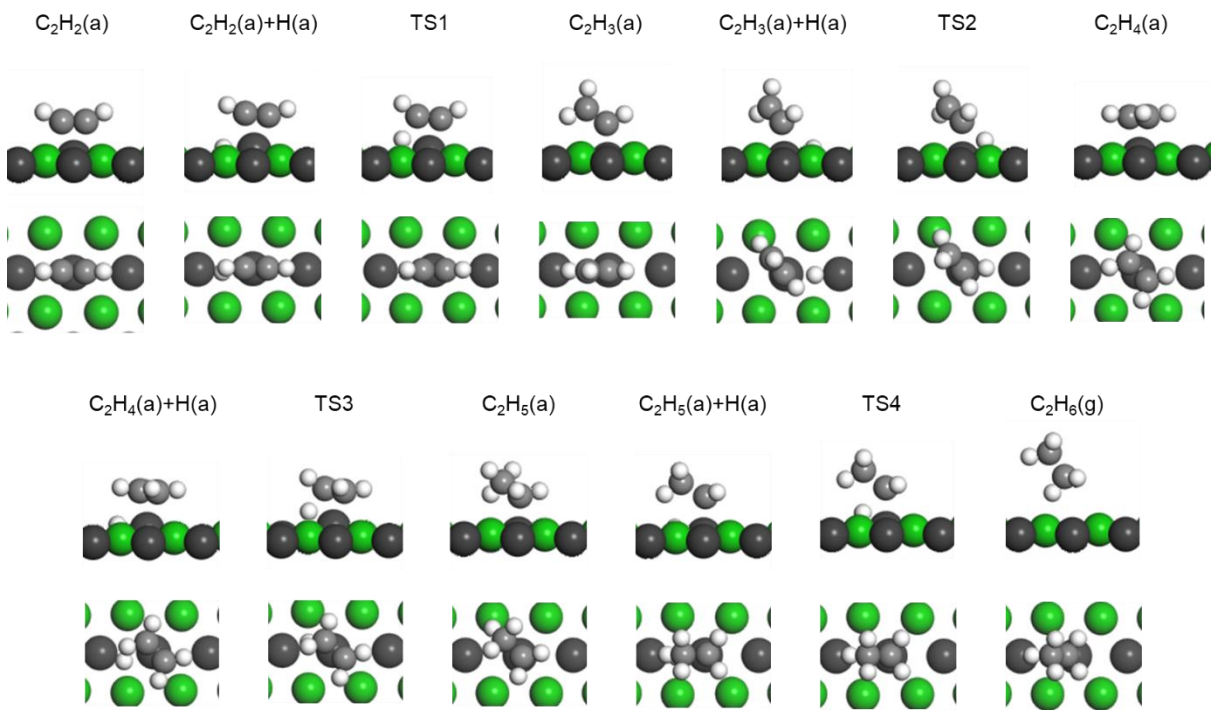

Figure 2.22. Optimized structures of the slab and adsorbates in acetylene hydrogenation to ethane over NiGa(110).

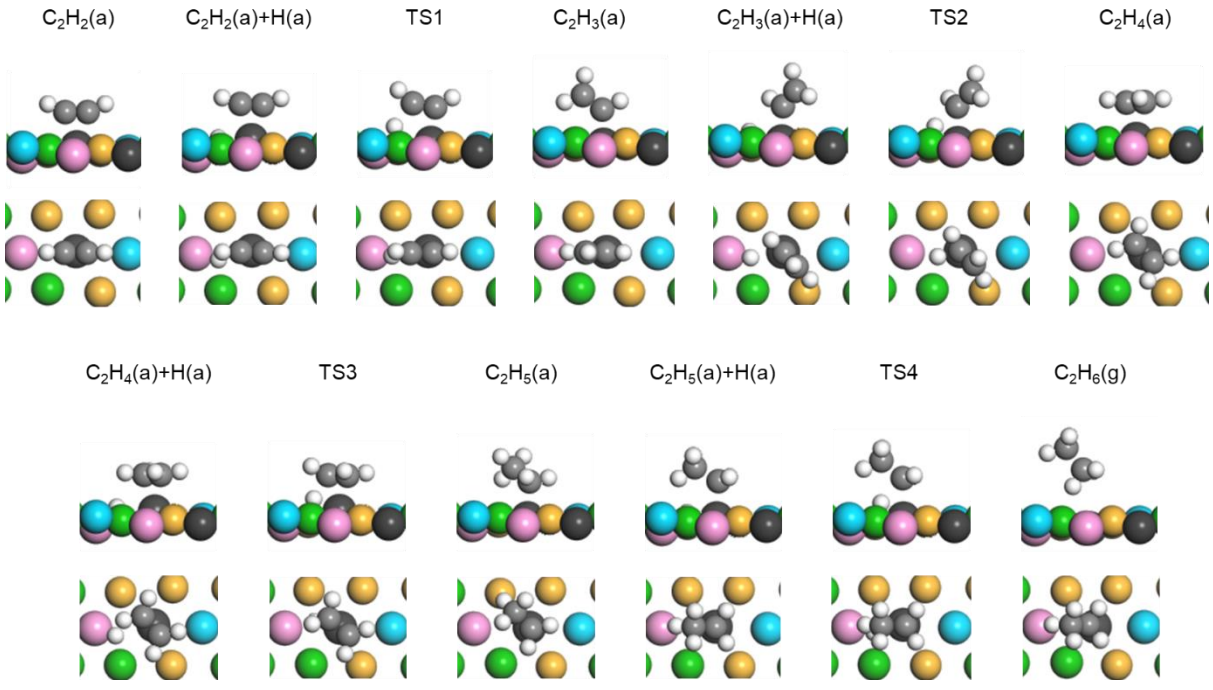

Figure 2.23. Optimized structures of the slab and adsorbates in acetylene hydrogenation to ethane over the A4d1 site of HEI.

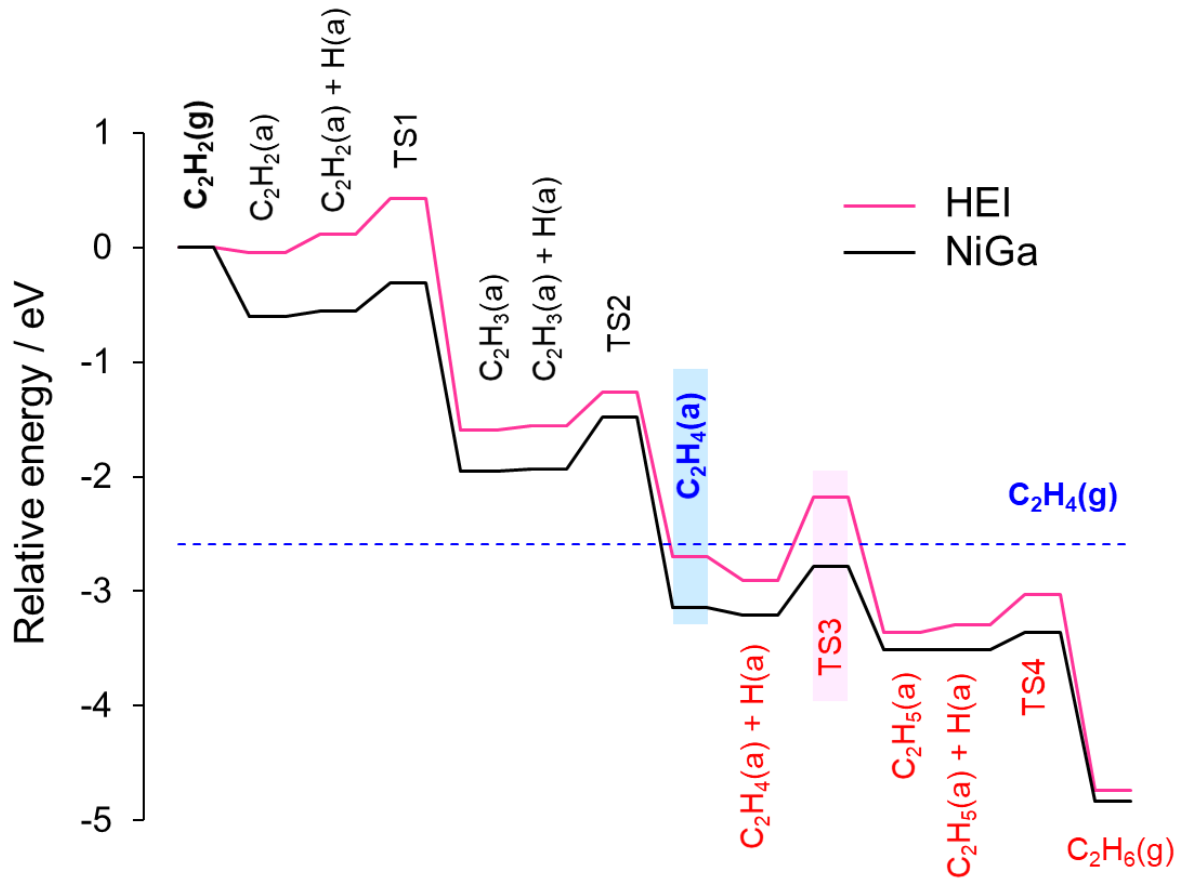

Figure 2.24. Comprehensive energy diagrams of acetylene hydrogenation to ethane over NiGa (110) and the A4d1 site of HEI. The total energy of the slab and gaseous acetylene was set to zero.

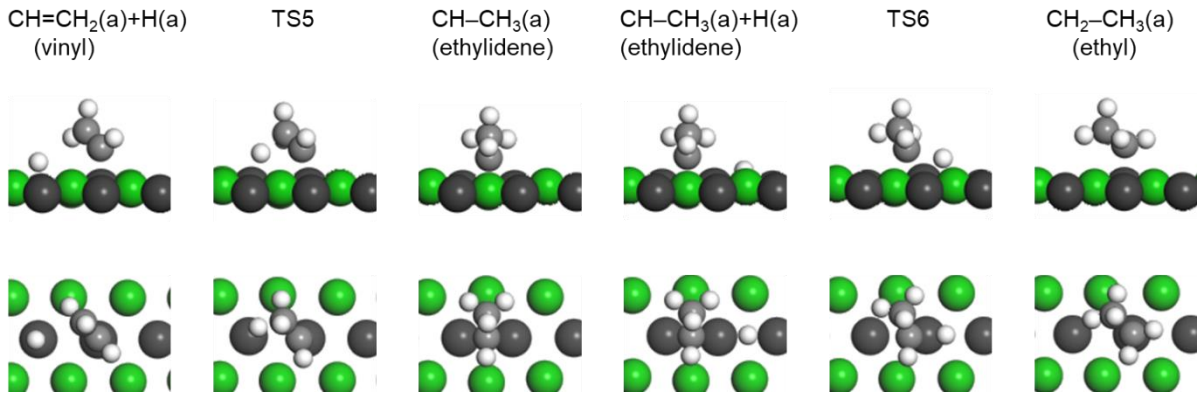

Figure 2.25. Optimized structures of the slab and adsorbates in ethylidene path over NiGa(110).

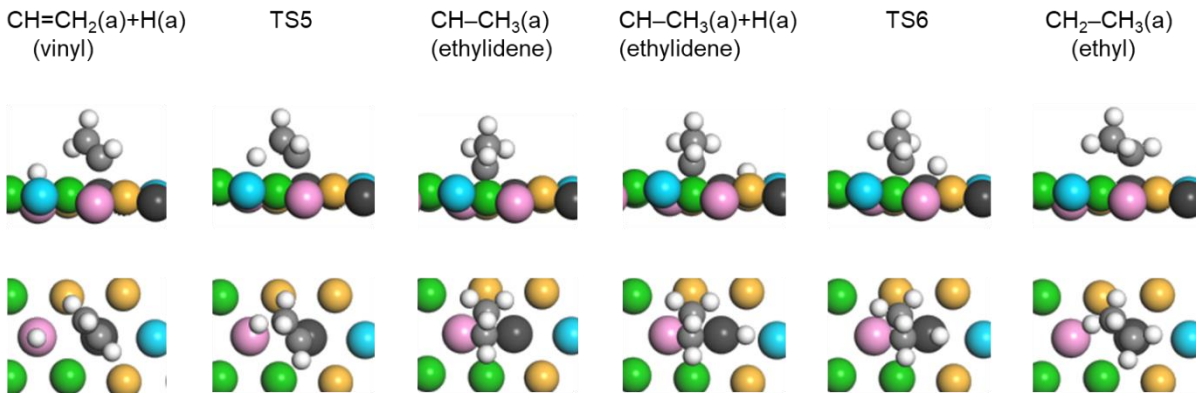

Figure 2.26. Optimized structures of the slab and adsorbates in ethylidene path over the A4d1 site of HEI.

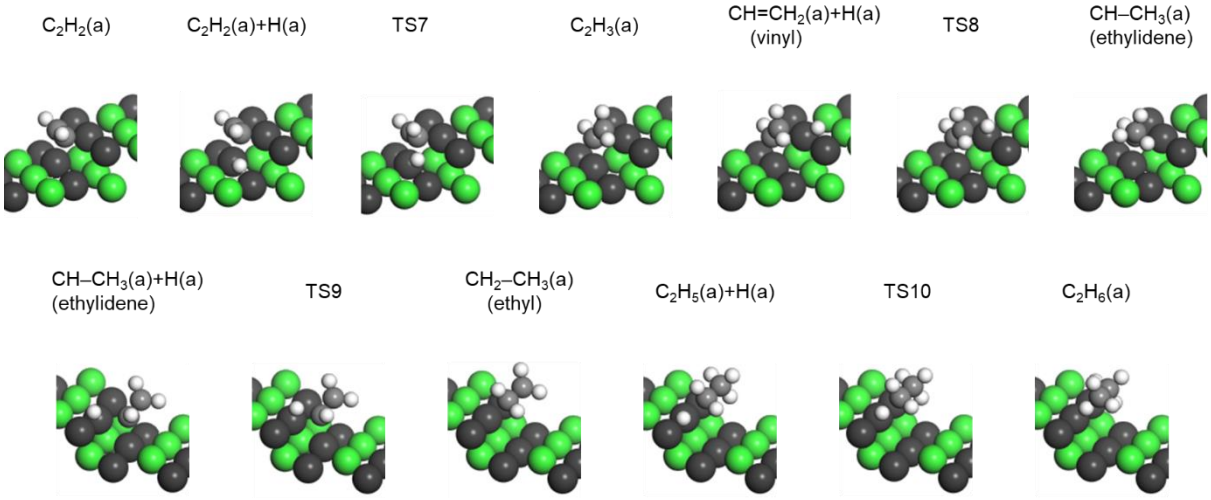

Figure 2.27. Optimized structures of the slab and adsorbates in ethylidene over NiGa(210).

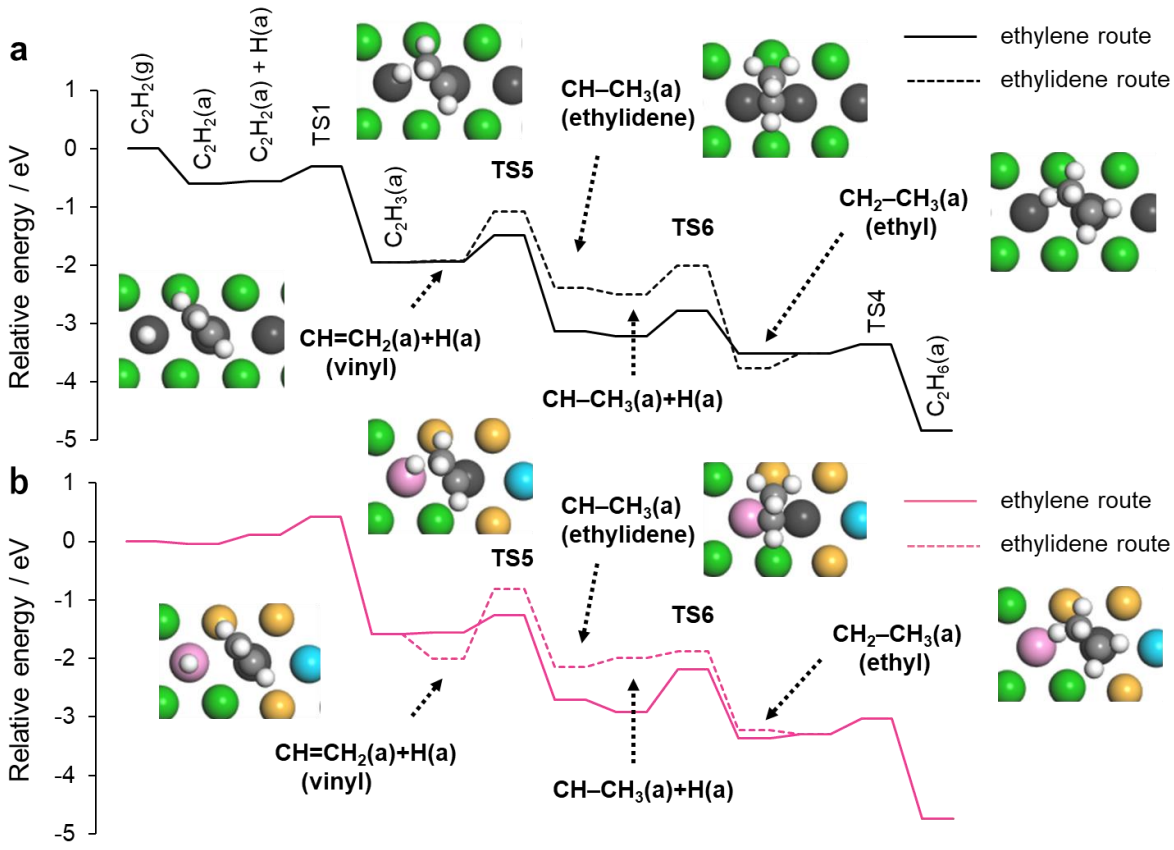

Figure 2.28. Comprehensive energy diagrams of acetylene hydrogenation to ethane via etylene and ethylidene routes over (a) NiGa(110) and (b) the A4d1 site of HEI. The total energy of the slab and gaseous acetylene was set to zero.

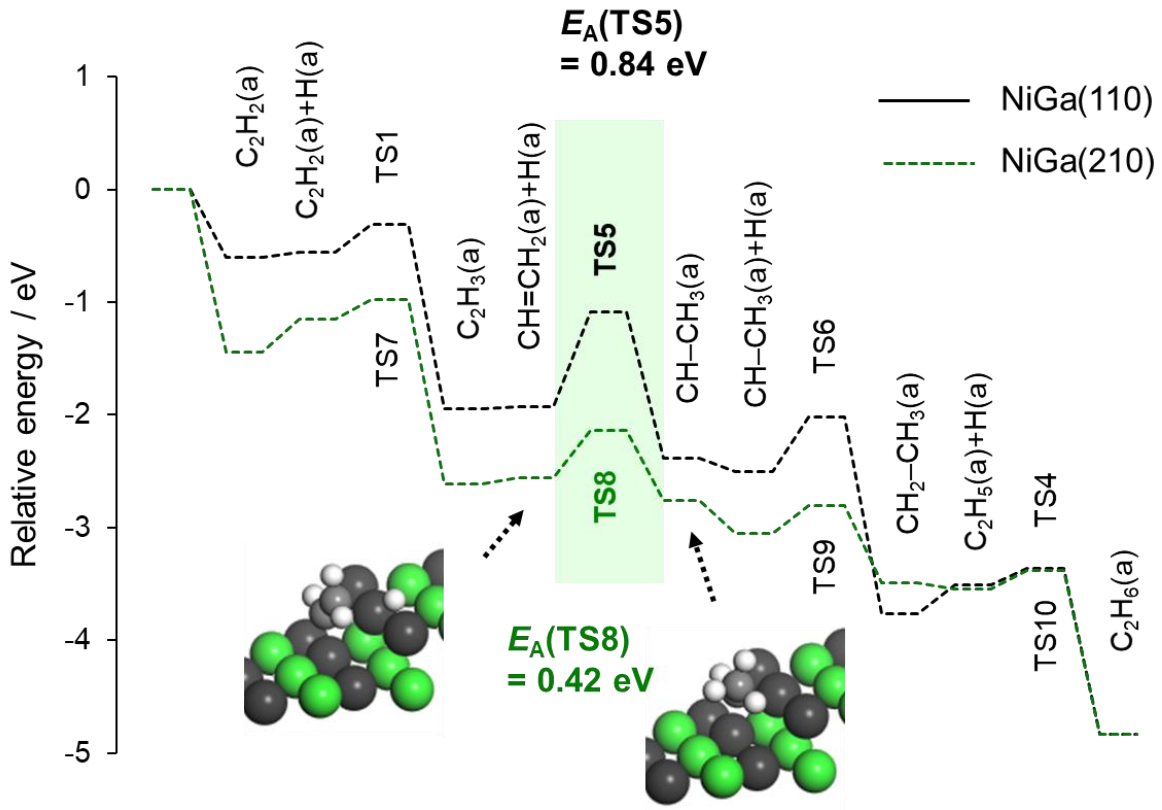

Figure 2.29. Comprehensive energy diagrams of acetylene hydrogenation to ethane via the ethylidene route over NiGa(110) and NiGa(210). The total energy of the slab and gaseous acetylene was set to zero.

2.4 Discussion

In summary, we designed and synthesized a Ni-based HEI catalyst supported on SiO_2 for highly efficient acetylene semi-hydrogenation. An intermetallic NiGa structure was multi-metalized to (NiFeCu)(GaGe) HEI without changing the parent CsCl-type structure so that Ni atoms were isolated with a minimum amount of diluent metals. This multi-metallization decreased the surface energy of the most stable (110) plane significantly, probably due to surface relaxation, which drastically promoted ethylene desorption. Therefore, the HEI catalyst does not hydrogenate ethylene even at the complete conversion of acetylene, thereby retaining high selectivity (typically >95%) over a wide range of operation temperatures (100°C–250°C). Moreover, HEI exhibited five times higher catalytic activity than NiGa and other 3d transition metal-based catalysts that showed high selectivity. The remarkable enhancement in catalytic activity can be attributed to the lower energy barrier of acetylene hydrogenation and facilitated

the adsorption/activation of hydrogen. Thus, the HEI catalyst can have excellent catalytic activity and selectivity in acetylene semi-hydrogenation, both of which were achieved using Ni as the main active metal for the first time. The role of multi-metallization on the enhancement was attributed to geometric effects but not to an electronic effect. The insights obtained in this study provide a highly efficient catalyst for semi-hydrogenation and an innovative catalyst design concept that is versatile for a wide variety of catalytic systems.

References

[1] J. K. N. Felix Studt, Frank Abild-Pedersen, Thomas Bligaard, Rasmus Z. Sørensen, Claus H. Christensen, *Science* **2008**, 1320.

[2] J. Osswald, K. Kovnir, M. Armbrüster, R. Giedigkeit, R. E. Jentoft, U. Wild, Y. Grin, R. Schlögl, *Journal of Catalysis* **2008**, *258*, 219.

[3] G. X. Pei, X. Y. Liu, A. Wang, A. F. Lee, M. A. Isaacs, L. Li, X. Pan, X. Yang, X. Wang, Z. Tai, K. Wilson, T. Zhang, *ACS Catalysis* **2015**, *5*, 3717.

[4] M. Armbrüster, K. Kovnir, M. Behrens, D. Teschner, Y. Grin, R. Schlögl, *Journal of the American Chemical Society* **2010**, *132*, 14745.

[5] K. Kovnir, M. Armbrüster, D. Teschner, T. V. Venkov, F. C. Jentoft, A. Knop-Gericke, Y. Grin, R. Schlögl, *Science and Technology of Advanced Materials* **2007**, *8*, 420.

[6] Y. Cao, Z. Sui, Y. Zhu, X. Zhou, D. Chen, *ACS Catalysis* **2017**, *7*, 7835.

[7] H. Zhou, X. Yang, L. Li, X. Liu, Y. Huang, X. Pan, A. Wang, J. Li, T. Zhang, *ACS Catalysis* **2016**, *6*, 1054.

[8] Y. Liu, X. Liu, Q. Feng, D. He, L. Zhang, C. Lian, R. Shen, G. Zhao, Y. Ji, D. Wang, G. Zhou, Y. Li, *Advanced Materials* **2016**, *28*, 4747.

[9] M. Armbrüster, K. Kovnir, M. Friedrich, D. Teschner, G. Wowsnick, M. Hahne, P. Gille, L. Szentmiklósi, M. Feuerbacher, M. Heggen, F. Girgsdies, D. Rosenthal, R. Schlögl, Y. Grin, *Nature Materials* **2012**, *11*, 690.

[10] F. Fu, Y. Liu, Y. Li, B. Fu, L. Zheng, J. Feng, D. Li, *ACS Catalysis* **2021**, *11*, 11117.

[11] C. Te Kuo, Y. Lu, L. Kovarik, M. Engelhard, A. M. Karim, *ACS Catalysis* **2019**, 11030.

[12] W. G. Menezes, L. Altmann, V. Zielasek, K. Thiel, M. Bäumer, *Journal of Catalysis* **2013**, *300*, 125.

[13] G. X. Pei, X. Y. Liu, A. Wang, L. Li, Y. Huang, T. Zhang, J. W. Lee, B. W. L. Jang, C. Y. Mou, *New Journal of Chemistry* **2014**, *38*, 2043.

[14] L. Zhang, Y. Ding, K. H. Wu, Y. Niu, J. Luo, X. Yang, B. Zhang, D. Su, *Nanoscale* **2017**, *9*, 14317.

[15] M. T. Darby, R. Réocreux, E. C. H. Sykes, A. Michaelides, M. Stamatakis, *ACS Catalysis* **2018**, *8*, 5038.

[16] M. T. Darby, M. Stamatakis, A. Michaelides, E. C. H. Sykes, *Journal of Physical Chemistry Letters* **2018**, *9*, 5636.

[17] Y. Cao, H. Zhang, S. Ji, Z. Sui, Z. Jiang, D. Wang, F. Zaera, X. Zhou, X. Duan, Y. Li, *Angewandte Chemie* **2020**, *132*, 11744.

[18] Y. Nakaya, E. Hayashida, H. Asakura, K. Shimizu, **n.d.**, 5.

[19] T. Komatsu, T. Kishi, T. Gorai, *Journal of Catalysis* **2008**, *259*, 174.

[20] C. Riley, A. De La Riva, S. Zhou, Q. Wan, E. Peterson, K. Artyushkova, M. D. Farahani, H. B. Friedrich, L. Burkemper, N. V. Atudorei, S. Lin, H. Guo, A. Datye, *ChemCatChem* **2019**, *11*, 1526.

[21] G. X. Pei, X. Y. Liu, A. Wang, Y. Su, L. Li, T. Zhang, *Applied Catalysis A: General* **2017**, *545*, 90.

[22] S. Zhou, L. Kang, X. Zhou, Z. Xu, M. Zhu, *Nanomaterials* **2020**, *10*, 1.

[23] B. Bridier, J. Pérez-Ramírez, *Journal of the American Chemical Society* **2010**, *132*, 4321.

[24] J. Gu, M. Jian, L. Huang, Z. Sun, A. Li, Y. Pan, J. Yang, W. Wen, W. Zhou, Y. Lin, H. J. Wang, X. Liu, L. Wang, X. Shi, X. Huang, L. Cao, S. Chen, X. Zheng, H. Pan, J. Zhu, S. Wei, W. X. Li, J. Lu, *Nature Nanotechnology* **2021**, *16*, 1141.

[25] W. F. Simanullang, J. Ma, K. I. Shimizu, S. Furukawa, *Catalysis Science and Technology* **2021**, *11*, 4016.

[26] Y. Chai, G. Wu, X. Liu, Y. Ren, W. Dai, C. Wang, Z. Xie, N. Guan, L. Li, *Journal of the American Chemical Society* **2019**, *141*, 9920.

[27] X. Dai, Z. Chen, T. Yao, L. Zheng, Y. Lin, W. Liu, H. Ju, J. Zhu, X. Hong, S. Wei, Y. Wu, Y. Li, *Chemical Communications* **2017**, *53*, 11568.

[28] Y. Liu, J. Zhao, J. Feng, Y. He, Y. Du, D. Li, *Journal of Catalysis* **2018**, *359*, 251.

[29] Y. Chen, J. Chen, *Applied Surface Science* **2016**, *387*, 16.

[30] J. Zhao, L. He, J. Yu, Y. Shi, R. Miao, Q. Guan, P. Ning, *New Journal of Chemistry* **2021**, *45*, 1054.

[31] B. Ravel, M. Newville, *Phys. Scr. T* **2005**, *T115*, 1007–1010.

[32] A. Ankudinov, B. Ravel, *Phys. Rev. B - Condens. Matter Mater. Phys.* **1998**, *58*, 7565–7576.

[33] M. D. Segall, P. J. D. Lindan, M. J. Probert, C. J. Pickard, P. J. Hasnip, S. J. Clark, M. C. Payne, *J. Phys. Condens. Matter* **2002**, *14*, 2717–2744.

[34] B. Hammer, L. B. Hansen, J. K. Nørskov, *Phys. Rev. B - Condens. Matter Mater. Phys.* **1999**, *59*, 7413–7421.

[35] A. Tkatchenko, M. Scheffler, *Phys. Rev. Lett.* **2009**, *102*, 6–9.

[36] K. Hu, M. Wu, S. Hinokuma, T. Ohto, M. Wakisaka, J. I. Fujita, Y. Ito, *J. Mater. Chem. A* **2019**, *7*, 2156–2164.

[37] T. A. Halgren, W. N. Lipscomb, *Chem. Phys. Lett.* **1977**, *49*, 225–232.

[38] N. Govind, M. Petersen, G. Fitzgerald, D. King-Smith, J. Andzelm, *Comput. Mater. Sci.* **2003**, *28*, 250–258.

[39] C. Li, Y. Chen, S. Zhang, J. Zhou, F. Wang, S. He, M. Wei, D. G. Evans, X. Duan, *ChemCatChem* **2014**, *6*, 824.

[40] S. Furukawa, T. Komatsu, *ACS Catalysis* **2017**, *7*, 735.

[41] L. Wang, F. Li, Y. Chen, J. Chen, *J. Energy Chem.* **2019**, *29*, 40–49.

[42] S. Leviness, V. Nair, A. H. Weiss, Z. Schay, L. Guczi, *Journal of Molecular Catalysis* **1984**, *25*, 131.

[43] E. Vignola, S. N. Steinmann, A. Al Farra, B. D. Vandegehuchte, D. Curulla, P. Sautet, *ACS Catalysis* **2018**, *8*, 1662.

[44] X. Shi, Y. Lin, L. Huang, Z. Sun, Y. Yang, X. Zhou, E. Vovk, X. Liu, X. Huang, M. Sun, S. Wei, J. Lu, *ACS Catalysis* **2020**, *10*, 3495.

[45] F. Huang, Y. Deng, Y. Chen, X. Cai, M. Peng, Z. Jia, J. Xie, D. Xiao, X. Wen, N. Wang, Z. Jiang, H. Liu, D. Ma, *Nature Communications* **2019**, *10*, 1.

[46] Y. Cao, H. Zhang, S. Ji, Z. Sui, Z. Jiang, D. Wang, F. Zaera, X. Zhou, X. Duan, Y. Li, *Angew. Chemie* **2020**, *132*, 11744–11749.

[47] Q. Chen, Z. Jin, *Metall. Mater. Trans. A* **1995**, *26*, 417–426.

[48] L. Kaufman, *Calphad* **1979**, *3*, 45–76.

[49] G. Cacciamani, J. De Keyzer, R. Ferro, U. E. Klotz, J. Lacaze, P. Wollants, *Intermetallics* **2006**, *14*, 1312–1325.

[50] W. F. Simanullang, J. Ma, K. I. Shimizu, S. Furukawa, *Catal. Sci. Technol.* **2021**, *11*, 4016–4020.

[51] S. Zhou, L. Kang, X. Zhou, Z. Xu, M. Zhu, *Nanomaterials* **2020**, *10*, 1–12.

[52] G. X. Pei, X. Y. Liu, A. Wang, Y. Su, L. Li, T. Zhang, *Appl. Catal. A Gen.* **2017**, *545*, 90–96.

[53] Y. Liu, X. Liu, Q. Feng, D. He, L. Zhang, C. Lian, R. Shen, G. Zhao, Y. Ji, D. Wang, G. Zhou, Y. Li, *Adv. Mater.* **2016**, *28*, 4747–4754.

[54] J. Zhao, L. He, J. Yu, Y. Shi, R. Miao, Q. Guan, P. Ning, *New J. Chem.* **2021**, *45*, 1054–1062.

[55] C. Riley, A. De La Riva, S. Zhou, Q. Wan, E. Peterson, K. Artyushkova, M. D. Farahani, H. B. Friedrich, L. Burkemper, N. V. Atudorei, S. Lin, H. Guo, A. Datye, *ChemCatChem* **2019**, *11*, 1526–1533.

[56] T. Komatsu, T. Kishi, T. Gorai, *J. Catal.* **2008**, *259*, 174–182.

[57] Y. Chen, J. Chen, *Appl. Surf. Sci.* **2016**, *387*, 16–27.

[58] Y. Chai, G. Wu, X. Liu, Y. Ren, W. Dai, C. Wang, Z. Xie, N. Guan, L. Li, *J. Am. Chem. Soc.* **2019**, *141*, 9920–9927.

[59] Y. Liu, J. Zhao, J. Feng, Y. He, Y. Du, D. Li, *J. Catal.* **2018**, *359*, 251–260.

[60] J. Gu, M. Jian, L. Huang, Z. Sun, A. Li, Y. Pan, J. Yang, W. Wen, W. Zhou, Y. Lin, H. J. Wang, X. Liu, L. Wang, X. Shi, X. Huang, L. Cao, S. Chen, X. Zheng, H. Pan, J. Zhu, S. Wei, W. X. Li, J. Lu, *Nat. Nanotechnol.* **2021**, *16*, 1141–1149.

[61] X. Dai, Z. Chen, T. Yao, L. Zheng, Y. Lin, W. Liu, H. Ju, J. Zhu, X. Hong, S. Wei, Y. Wu, Y. Li, *Chem. Commun.* **2017**, *53*, 11568–11571.

[62] F. Huang, Y. Deng, Y. Chen, X. Cai, M. Peng, Z. Jia, J. Xie, D. Xiao, X. Wen, N. Wang, Z. Jiang, H. Liu, D. Ma, *Nat. Commun.* **2019**, *10*, 1–7.

[63] X. Shi, Y. Lin, L. Huang, Z. Sun, Y. Yang, X. Zhou, E. Vovk, X. Liu, X. Huang, M. Sun, S. Wei, J. Lu, *ACS Catal.* **2020**, *10*, 3495–3504.

[64] F. Fu, Y. Liu, Y. Li, B. Fu, L. Zheng, J. Feng, D. Li, *ACS Catal.* **2021**, *11*, 11117–11128.

[65] C. Lu, A. Zeng, Y. Wang, A. Wang, *ACS Omega* **2021**, *6*, 3363–3371.

[66] C. Lu, Y. Wang, R. Zhang, B. Wang, A. Wang, *ACS Appl. Mater. Interfaces* **2020**, *12*, 46027–46036.

[67] M. Armbrüster, K. Kovnir, M. Friedrich, D. Teschner, G. Wowsnick, M. Hahne, P. Gille, L. Szentmiklósi, M. Feuerbacher, M. Heggen, F. Girgsdies, D. Rosenthal, R. Schlögl, Y. Grin, *Nat. Mater.* **2012**, *11*, 690–693.

[68] T. Kojima, S. Kameoka, S. Fujii, S. Ueda, A. P. Tsai, *Sci. Adv.* **2018**, *4*, 1–8.

[69] S. Riyapan, Y. Zhang, A. Wongkaew, B. Pongthawornsakun, J. R. Monnier, J. Panpranot, *Catalysis Science and Technology* **2016**, *6*, 5608.

[70] M. W. Schreiber, C. P. Plaisance, M. Baumgärtl, K. Reuter, A. Jentys, R. Bermejo-Deval, J. A. Lercher, *Journal of the American Chemical Society* **2018**, *140*, 4849.

[71] Z. Maeno, S. Yasumura, X. Wu, M. Huang, C. Liu, T. Toyao, K. I. Shimizu, *Journal of the American Chemical Society* **2020**, *142*, 4820.

Chapter Three

Active Site Tuning Based on pseudo-Binary Alloys for Low-Temperature Acetylene Semi-hydrogenation

3.1 Introduction

The selective hydrogenation of a trace amount of acetylene in crude ethylene while inhibiting over-hydrogenation to ethane is a major industrial process for producing polymer-grade ethylene toward polyethylene production[1]. Pd-based catalysts have been industrially used for the selective hydrogenation of acetylene[2], and the use of noble metals increases the cost of the overall process. Therefore, developing an efficient catalyst using nonnoble metals is urgently required in pure and applied chemistry. In this context, noble-metal-alternative catalysts using 3d transition metals, such as Ni, Co, Cu, and Fe, are promising candidates.

Ni-based alloys have been studied as potential candidates as industrial catalysts for acetylene semi-hydrogenation owing to the relatively high hydrogenation activity of Ni and the enhanced selectivity derived from alloying with less active elements. However, the insufficient low-temperature activity of Ni-based catalysts, compared with that of Pd-based catalysts (e.g., Pd is workable even at <100°C, whereas Ni typically requires a temperature >200°C), hampers their industrial application for acetylene semi-hydrogenation[3]. Therefore, a novel catalyst design concept that significantly enhances the hydrogenation activity of Ni without lowering the semi-hydrogenation selectivity is highly desired. To develop an ideal reaction environment for this purpose, the geometric and electronic states of surface Ni sites should be finely controlled and optimized. Ordered alloys, such as NiM intermetallics (e.g., NiZn[1], NiGa[4], and NiIn[5]), exhibit specific atomic arrangements and unique electronic states, demonstrating high ethylene selectivity in acetylene semi-hydrogenation. However, the regulated structures do not allow flexible modification of the reaction environment. Conversely, solid-solution alloys, such as the Ni–Cu system, can arbitrarily vary the composition ratio, whereas various Ni_xCu_y ensembles are generated due to the randomness, which typically results in less selective hydrogenation.

A trimetallic pseudo-binary alloy described as $(A_{1-x}A'_x)_mB_n$, where a part of active metal A is substituted by a similar third element A' (close to A in the periodic table), can be a promising candidate to provide high flexibility, tunability, and functionality to the reaction environment owing to the combination of the specific structure derived from intermetallic A_mB_n and the wide variation in x. Choosing an appropriate structure of parent Ni_mM_n, the third

element, and its doping amount, *x*, will facilitate the construction of an optimal and well-tuned active site for highly active and selective acetylene semi-hydrogenation.

Here, we used Ni_3Ga and Cu as the parent intermetallic structure and the third element for active site tuning, respectively. Considering that Ni_3Ga exhibits moderately high hydrogenation activity and ethylene selectivity while remaining Ni_3 hollow sites on the most stable (111) surface (Figure 3.1), there is a large room for active-site modulation to improve catalytic performance. In addition, Cu is known as a diluent for active Ni–Ni ensembles with high solubility. Therefore, doping Cu into the Ni sites of Ni_3Ga to form a $(Ni_{1-x}Cu_x)_3Ga$ pseudo-binary alloy allows the flexible design and fine-tuning of the reaction environment for efficient semi-hydrogenation (Figure 3.1). Herein, we report that $(Ni_{0.8}Cu_{0.2})_3Ga/TiO_2$ acted as a highly active and selective catalyst for acetylene semi-hydrogenation, where the optimal Cu doping outstandingly improved the hydrogenation activity while maintaining excellent ethylene selectivity. This resulted in a 48- fold higher specific activity than that of reported 3d transition metal-based catalysts at 150°C. Moreover, this catalyst is workable even at 100°C with high performance (100% conversion with 96% selectivity) for the first time. In addition, we showed atomic-level insight into the significant enhancement in the catalytic performance clarified by deep characterization and mechanistic studies.

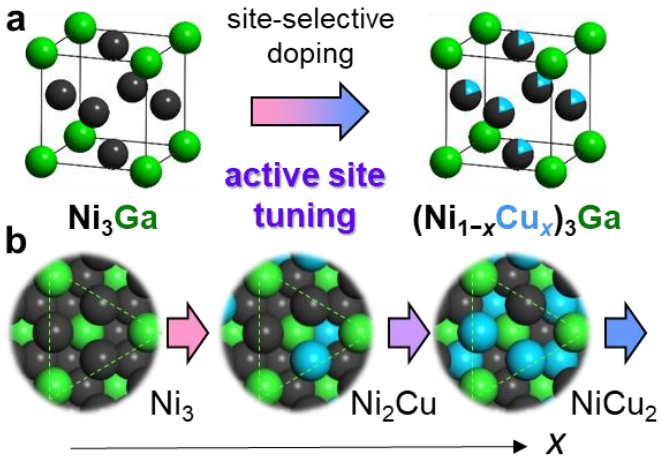

Figure 3.1. Active site tuning based on pseudo-binary alloy. (a) Site-selective doping of Cu to the Ni sites of intermetallic Ni_3Ga to form a $(Ni_{1-x}Cu_x)_3Ga$ pseudo-binary alloy. (b) Atomic arrangement of the Ni_3Ga (111) surface and the changes in the Ni_3 hollow sites upon Cu substitution.

3.2 Experimental section

3.2.1 Catalyst preparation

$(Ni_{1-x}M_x)_3Ga/TiO_2$ (M = Cu, Fe, Co, Zn) and Ni_3Ga/TiO_2 (Ni: 1 wt.%) were prepared through a conventional impregnation method using $Ni(NO_3)_2{\cdot}6H_2O$ (Wako, 99.9%); Cu $(NO_3)_2{\cdot}3H_2O$ (Furuya Metal Co. Ltd.); $Fe(NO_3)_3{\cdot}9H_2O$ (Furuya Metal Co. Ltd.); $Co(NO_3)_3{\cdot}6H_2O$ (Wako, 98%); $Zn(NO_3)_2{\cdot}6H_2O$ (Kanto, 99%); and Ga $(NO_3)_3{\cdot}nH_2O$ (n = 7–9, Wako, 99.9%) as metal precursors. The TiO_2 support (Degussa P25, S_{BET} = 35–65 $m^2\ g^{-1}$, anatase + rutile) was added to a vigorously stirred aqueous solution (50 mL H_2O per gram of TiO_2) containing the precursors of Ni, Ga, and M, followed by stirring for 3 h at 30°C (Ni: 1 wt%, (Ni+Cu)/Ga = 3). The stoichiometric or small excess Cu was fed for the formation of the desired alloy phase: Cu/(Ni+Cu) = 0, 0.2, 0.33, 0.5, 0.6, 0.67, 0.8 for x = 0, 0.2, 0.25, 0.33, 0.5, 0.6, and 0.75, respectively. The mixture was dried under a reduced pressure at 40°C using a rotary evaporator. Next, the sample was calcined under flowing air at 400°C for 1 h and reduced under flowing hydrogen (50 ml min^{-1}) at 600°C for 1 h. The ramping rate was set at 10°C min^{-1} for the calcination and reduction procedures. The corresponding SiO_2-supported catalysts were prepared through the pore-filling co-impregnation method. The mixed aqueous solution of the metal precursors was added dropwise to SiO_2 (CARiACT G–6, Fuji Silysia, S_{BET} = 673 $m^2\ g^{-1}$) to ensure that the solutions only filled the pores of the silica gel (volume of solution: 1.6 mL per gram of silica). The resulting mixture was sealed and aged overnight at room temperature, followed by rapid freezing using liquid nitrogen and subsequent freeze-drying under vacuum at −5°C overnight. Thereafter, the obtained sample was dried overnight in an oven at 90°C, followed by calcination and reduction, as mentioned above.

3.2.2 Characterization

HAADF–STEM analysis was conducted using a JEOL JEM-ARM200 M microscope equipped with an EDX detector. The XRD patterns of the catalysts were recorded using a MiniFlex 700+D/teX Ultra instrument using a Cu Kα X-ray source. EXAFS measurements of the catalysts were conducted at the BL14B2 and BL01B1 beamlines of SPring-8, Japan Synchrotron Radiation Research Institute (JASRI) using Si (111) double crystals as

monochromators. The spectra were recorded at the Ni, Cu, and Ga K-edges in transmission (reference samples and $(Ni_{0.8}Cu_{0.2})_3Ga/SiO_2$ at the Ni and Ga K-edges) and fluorescence (other samples and edges) modes at room temperature. Prior to the measurements, the catalyst was pelletized and pretreated using H_2 at 600°C for 0.5 h in a quartz tube. Afterward, a quartz tube containing the reduced pellet was sealed and transferred to an Argon glove box (O_2, <0.01 ppm) to prevent exposure to air. The pellet was sealed in a plastic film bag (Barrier Nylon) with an oxygen absorber (ISO A500-HS: Fe powder). The obtained EXAFS spectra were analyzed using Athena and Artemis software (ver. 0.9.25) implemented in the Demeter package. The k^3-weighted EXAFS oscillation was Fourier-transformed in the k range of 3–12 $Å^{-1}$. The backscattering amplitude and phase shift functions were calculated using FEFF8.

Temperature-programmed analyses were conducted using a BELCAT-II (Microtrac BEL) instrument. For C_2H_2-TPD, the catalyst (100 mg) was pretreated at 600°C under flowing 5% H_2/Ar (20 mL min^{-1}) for 0.5 h and cooled to 50°C under flowing Ar, followed by cooling to −50°C using liquid nitrogen with an Ar purge (20 mL min^{-1}). The resulting catalyst was exposed to C_2H_2 for 1 h at −50°C. Afterward, Ar was purged for 90 min to remove physisorbed species. Thereafter, the temperature was increased from −50°C at a ramp rate of 5°C min^{-1} under flowing Ar, where the desorbed species were analyzed by quadrupole mass spectrometry placed downstream. C_2H_4-TPD was performed similarly to C_2H_2-TPD except that the adsorption and starting temperature was−80°C. C_2H_4/H_2-TPSR was conducted using the catalyst (80 mg) pretreated with a 5% H_2/Ar gas mixture (20 mL min^{-1}) for 0.5 h. After the reduction, the catalyst was cooled to 30°C using CATCryo-II under a He flow (20 mL min^{-1}), exposed to a mixture of C_2H_4 and 5% H_2/Ar (1 and 20 mL min^{-1}, respectively) at the same temperature for 30 min, and heated from 30°C to 350°C at a ramping rate of 10°C min^{-1}. The formation of ethane (C_2H_6; m/z = 30) in the outlet gas was analyzed online similarly to TPD.

3.2.3 Catalytic Reaction

Acetylene semi-hydrogenation was conducted in a quartz fixed-bed reactor with an internal diameter of 6 mm at atmospheric pressure. Generally, the catalyst (80 mg) was diluted with quartz sand (2.0 g) loaded into the quartz tube, which was reduced under flowing H_2 gas (20

mL min^{-1}) at 600°C for 0.5 h and cooled to 30°C under a He flow (20 mL min^{-1}) prior to the catalytic reaction. Subsequently, the catalysts were evaluated by feeding the reactant gas mixture (C_2H_2:H_2:C_2H_4:He = 1:10:5/0:39 mL min^{-1}) into the reactor. The temperature dependence of the catalytic performance was evaluated from 100°C to 250°C at a ramping rate of 10°C min^{-1}. The outlet gas was analyzed and quantified using an online gas chromatograph (Shimadzu GC-8A with a column of Unipak S, GL Science) equipped with a thermal conductivity detector. In this study, C_2H_4 and C_2H_6 were the only C_2 products detected by gas chromatography (GC). No C1 and C4 compounds were detected under the reaction conditions tested in this study. Acetylene conversion and ethylene selectivity were defined by the following equations:

$$C_2H_2 \text{ conversion} = \frac{[C_2H_2]_{inlet} - [C_2H_2]_{outlet}}{[C_2H_2]_{inlet}} \times 100\% \quad (1)$$

$$C_2H_4 \text{ selectivity} = 1 - \frac{[CH_4]_{outlet} + [C_2H_6]_{outlet} + [C_4]_{outlet}}{[C_2H_2]_{inlet} - [C_2H_2]_{outlet}} \times 100\% \quad (2)$$

All the catalytic tests for kinetic analysis (Arrhenius-type plots and reaction orders) were performed within a low conversion region (<15%) by adjusting the catalyst amount. All data points were collected four times at 15-min intervals, and their averages were reported.

3.2.4 Computational details

Periodic DFT calculations were performed using the CASTEP code[6] with Vanderbilt-type ultrasoft pseudopotentials as well as the revised version of the Perdew–Burke–Ernzerhof exchange–correlation functional based on the generalized gradient approximation[7]. The plane-wave basis set was truncated at a kinetic energy of 360 eV. A 0.1-eV Fermi smearing was used. The Tkatchenko–Scheffler method was employed to analyze dispersion correlations with a scaling coefficient of s_R = 0.94 and a damping parameter of d = 20[8]. The reciprocal space was sampled using a k-point mesh with a spacing of 0.04 $Å^{-1}$, as generated by the Monkhorst–Pack scheme[9]. The slab model was constructed using Ni_3Ga (111) planes with a

thickness of four atomic layers with 13 Å of vacuum spacing. For Cu doping, a part of the Ni atoms in the two surface layers was replaced with Cu so that the Ni/Cu ratio in those layers was four. Geometry optimizations and TS searches were performed on supercell structures using periodic boundary conditions. The convergence criteria for structural optimization and energy calculation were set at (a) a self-consistent field tolerance of 1.0×10^{-6} eV per atom, (b) an energy tolerance of 1.0×10^{-5} eV per atom, (c) a maximum force tolerance of 0.05 eV $Å^{-1}$, and (d) a maximum displacement tolerance of 1.0×10^{-3} Å. The TS search was performed using the complete linear synchronous transit/quadratic synchronous transit (LST/QST) method.[10,11] The convergence criterion for the TS calculations was set at root-mean-square forces on an atom tolerance of 0.1 eV $Å^{-1}$.

3.3 Results

3.3.1 Structure characterization of the catalysts

First, Ni_3Ga and a series of $(Ni_{1-x}Cu_x)_3Ga$ catalysts (x = 0.2, 0.25, 0.33, 0.5, 0.6, and 0.75) were prepared through the conventional co-impregnation method using TiO_2 as a support (see Methods section for details). Figures 3.1a–3.1e shows the high-angle annular dark-field scanning transmission electron microscopy (HAADF–STEM) images of $(Ni_{0.8}Cu_{0.2})_3Ga/TiO_2$ and the corresponding elemental maps acquired by energy dispersive X-ray (EDX) analysis.

Ni, Cu, and Ga were uniformly dispersed on the nanoparticle, suggesting the homogeneous formation of a Ni–Cu–Ga ternary alloy (see Figure 3.2 for other nanoparticles). The particle size range was 5–20 nm with a volume-weighted average of 11.4 nm (Figure 2f). The high-resolution HAADF–STEM image shows lattice fringes with 2.09 Å and 2.55 Å spacings with a dihedral angle of 90° (Figure 3.1g), which roughly correlate with the interplanar distances of the (111) and (110) planes of Ni_3Ga (2.07 Å and 2.53 Å), respectively. The slightly larger sizes can be attributed to the expansion of the Ni_3Ga lattice due to Cu doping to the Ni site (atomic radii: Ni, 1.244 Å; Cu, 1.276 Å). The magnification shows that the atomic arrangement matched with the Ni_3Ga-type crystal viewed along the [112] direction (Figure 3.1h). Moreover, the superlattice diffraction spots ({110}; indicated by arrows) were observed in the corresponding fast Fourier transform image (FFT; Figure 3.1h, lower right inset), which

evidences that the ternary alloy exhibited an $L1_2$ intermetallic structure but was not a face-centered cubic (fcc) solid-solution alloy. Thereafter, another quantitative analysis for the lattice expansion was conducted by X-ray diffraction (XRD). As shown in Figure 3.1i, Ni_3Ga/TiO_2 exhibited a broad peak at 43.74° (overlapped with TiO_2's diffraction), which correlated with the 111 diffraction of intermetallic Ni_3Ga. This peak shifted to a lower angle (43.52°) upon Cu doping, again indicating lattice expansion. Notably, the diffraction angle of the ternary alloy correlated with the theoretical estimation (43.52°; corresponding to 0.5% lattice expansion) using Vegard's law and assuming a solid solution between Ni_3Ga and Cu_3Ga at a ratio of 0.8:0.2. These results strongly suggested that the $(Ni_{0.8}Cu_{0.2})_3Ga$ pseudo-binary alloy with an $L1_2$ structure was formed as nanoparticles on a TiO_2 support. The crystallite size of the alloy phase was also estimated using Scherrer's equation (10.6 nm, Table 3.1), which correlated with the mean particle size estimated from the HAADF–STEM images.

We also performed extended X-ray absorption fine structure (XAFS) analysis for insight into the electronic and geometric states. The X-ray absorption near edge structure (XANES) spectra confirmed that Ni, Cu, and Ga in Ni_3Ga/TiO_2 and $(Ni_{0.8}Cu_{0.2})_3Ga/TiO_2$ were all in the metallic states (Figures 3.1k–3.1l, see Figure 3.3b for Cu K-edge). In addition, only a minimal difference was observed in the electronic states of Ni and Ga when Cu was doped, indicating that the ligand effect of Cu was extremely minor. The Ni and Cu K-edge EXAFS spectra of $(Ni_{0.8}Cu_{0.2})_3Ga/TiO_2$ exhibited oscillation features similar to those of the Ni K-edge EXAFS of Ni_3Ga/TiO_2 (Figure 3.1m), suggesting that Ni and Cu were present at crystallographically similar sites, i.e., Cu doping to the Ni site. The similarity in the oscillation features was also observed in the Ga K-edge EXAFS spectra, indicating that the original intermetallic structure was retained. Interestingly, the period of the EXAFS oscillation in each edge slightly reduced after Cu doping (Figure 3.1m, vertical dotted line). This correlated with the lattice expansion by Cu doping as indicated by STEM and XRD. We also performed EXAFS curve-fitting analysis to obtain structural information (Table 3.2 and Figures 3.4–3.6). For Ni_3Ga/TiO_2, Ni–Ni, Ni–Ga, and Ga–Ni scatterings were assigned, in which the coordination number (CN) ratio of Ni–Ga and Ni–Ni was 2.0. This correlated with the $L1_2$ intermetallic structure of Ni_3Ga. A small contribution of Ga–O (CN = 2.28) was observed, probably due to the interaction with the

lattice oxygen of the TiO_2 support rather than the presence of Ga oxide because Ga is metallic, as evidenced by XANES. For $(Ni_{0.8}Cu_{0.2})_3Ga/TiO_2$, Ni–Ga, Ni–Ni (Cu), and Ga–Ni (Cu), and Ga–O scatterings were observed similarly to Ni_3Ga/TiO_2. In addition, Cu–Ga and Cu–Cu (Ni) scatterings were detected in its Cu K-edge spectra with CNs similar to those of Ni–Ga and Ni–Ni (Cu), which correlated with the Cu doping to the Ni site. Furthermore, the interatomic distances of Ni–Ga, Ni–Ni (Cu), and Ga–Ni (Cu) were slightly elongated by Cu doping (+0.01 Å for each, Table 3.2). This corresponded to a 0.4% expansion and agreed with that estimated from the peak shift in the XRD pattern (0.5%). Thus, we concluded that the nanoparticulate pseudo-binary alloy of $(Ni_{0.8}Cu_{0.2})_3Ga$ was formed on TiO_2.

The $(Ni_{1-x}Cu_x)_3Ga/TiO_2$ catalysts with other Cu contents were analyzed by XRD, where peak shifts at lower angles corresponding to the doped Cu content were observed (Figure 3.8). Thus, we successfully prepared a series of $(Ni_{1-x}Cu_x)_3Ga/TiO_2$ catalysts with the pseudo-binary alloy structure with a wide range of Cu contents (x = 0, 0.2, 0.25, 0.33, 0.5, 0.6, 0.75).

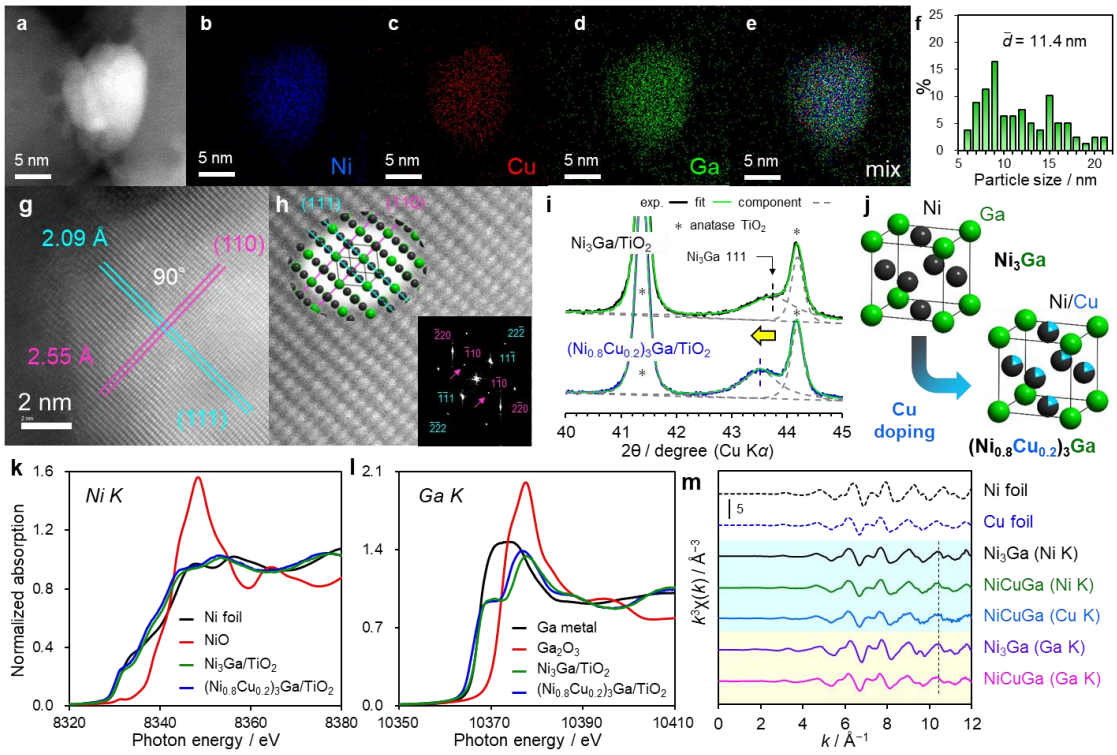

Figure 3.1. Characterization of $(Ni_{0.8}Cu_{0.2})_3Ga/TiO_2$. (a) HAADF–STEM image and the corresponding elemental maps for (b) Ni, (c) Cu, (d) Ga, and (e) Ni + Cu + Ga. f Particle-size distribution. (g) High-resolution image and (h) its magnification overlapped with the Ni_3Ga crystal viewed along the [112] direction (upper left) and the corresponding FFT image (lower right). (i) XRD patterns with peak deconvolution. (j) Crystal structure of Ni_3Ga and $(Ni_{0.8}Cu_{0.2})_3Ga$ (k) Ni and (l) Ga K-edge XANES spectra. m k^3-Weighted EXAFS raw oscillations.

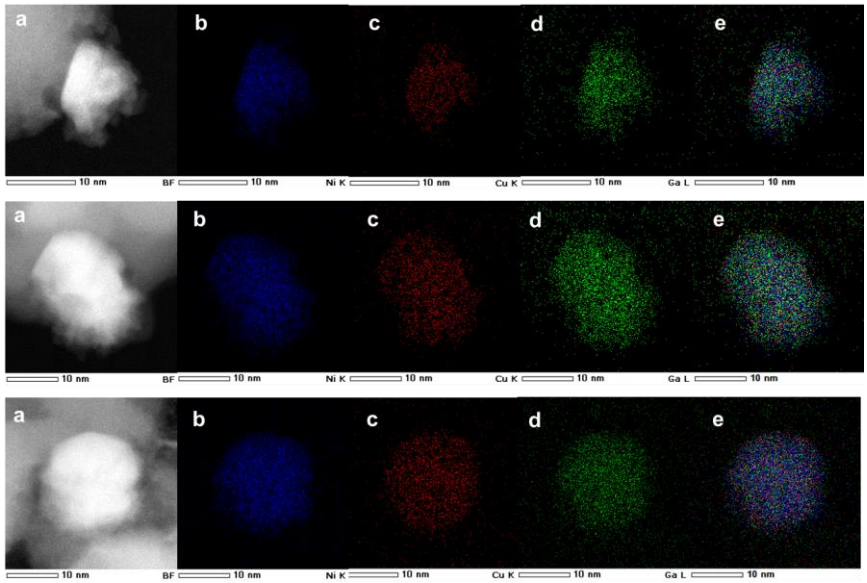

Figure 3.2. (a) HAADF–STEM image and the corresponding elemental maps for (b) Ni, (c) Cu, (d) Ga, (e) Ni+Cu+Ga (magnified for a few particles) for $(Ni_{0.8}Cu_{0.2})_3Ga/TiO_2$.

Table 3.1. Particle size of $(Ni_{0.8}Cu_{0.2})_3Ga/TiO_2$, $(Ni_{0.8}Cu_{0.2})_3Ga/SiO_2$ and Ni_3Ga/TiO_2 calculated according to Scherrer equation.

catalysts	Scherrer constant	half with / degree	center / degree	crystallite size / nm
$(Ni_{0.8}Cu_{0.2})_3Ga/TiO_2$		0.76	43.52	10.6
Ni_3Ga/TiO_2	0.849	1.03	43.74	7.8
$(Ni_{0.8}Cu_{0.2})_3Ga/SiO_2$		1.60	43.74	5.1

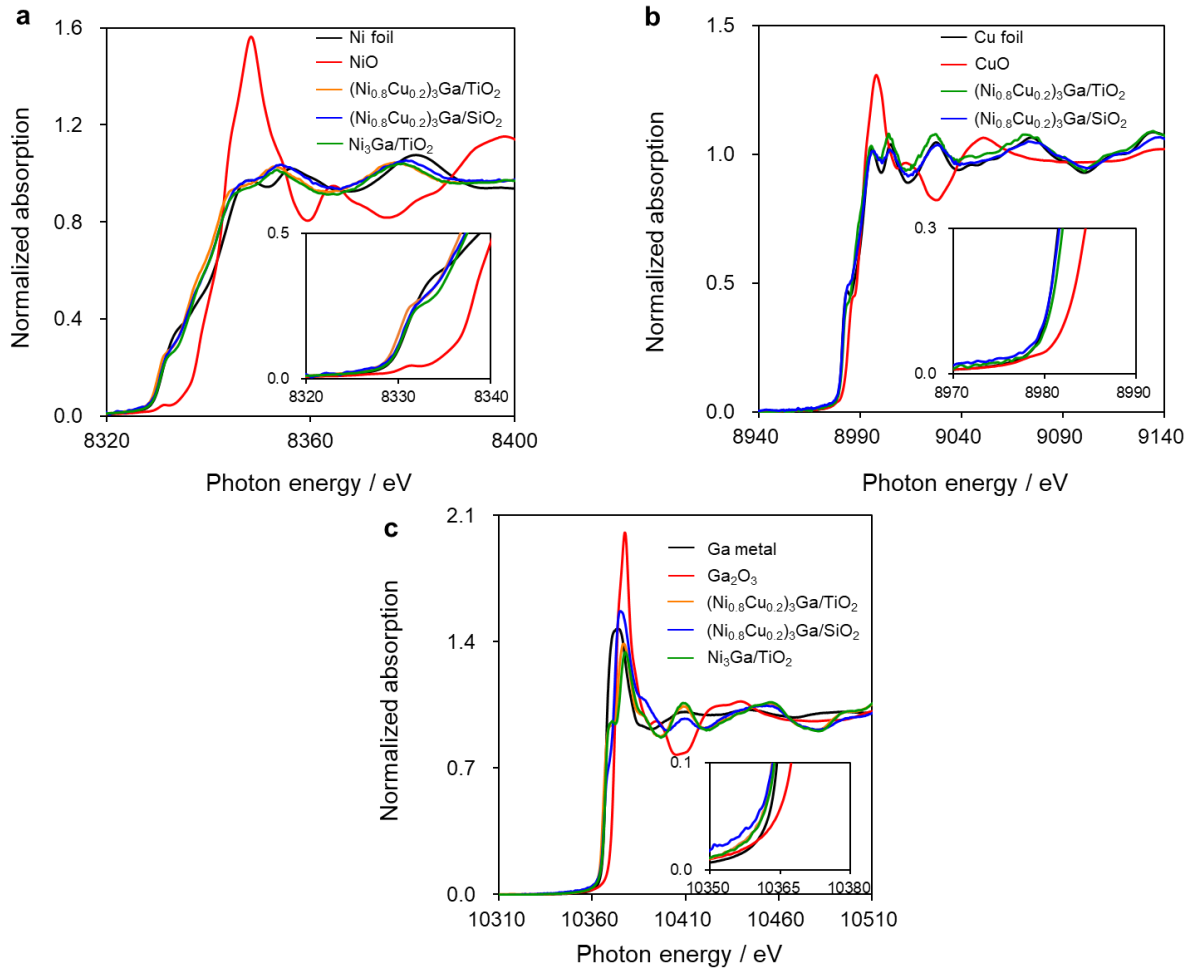

Figure 3.3. (a) Ni, (b) Cu, and (c) Ga K-edge XANES spectra of over $(Ni_{0.8}Cu_{0.2})_3Ga/TiO_2$, $(Ni_{0.8}Cu_{0.2})_3Ga/SiO_2$, Ni_3Ga/TiO_2 and reference compounds.

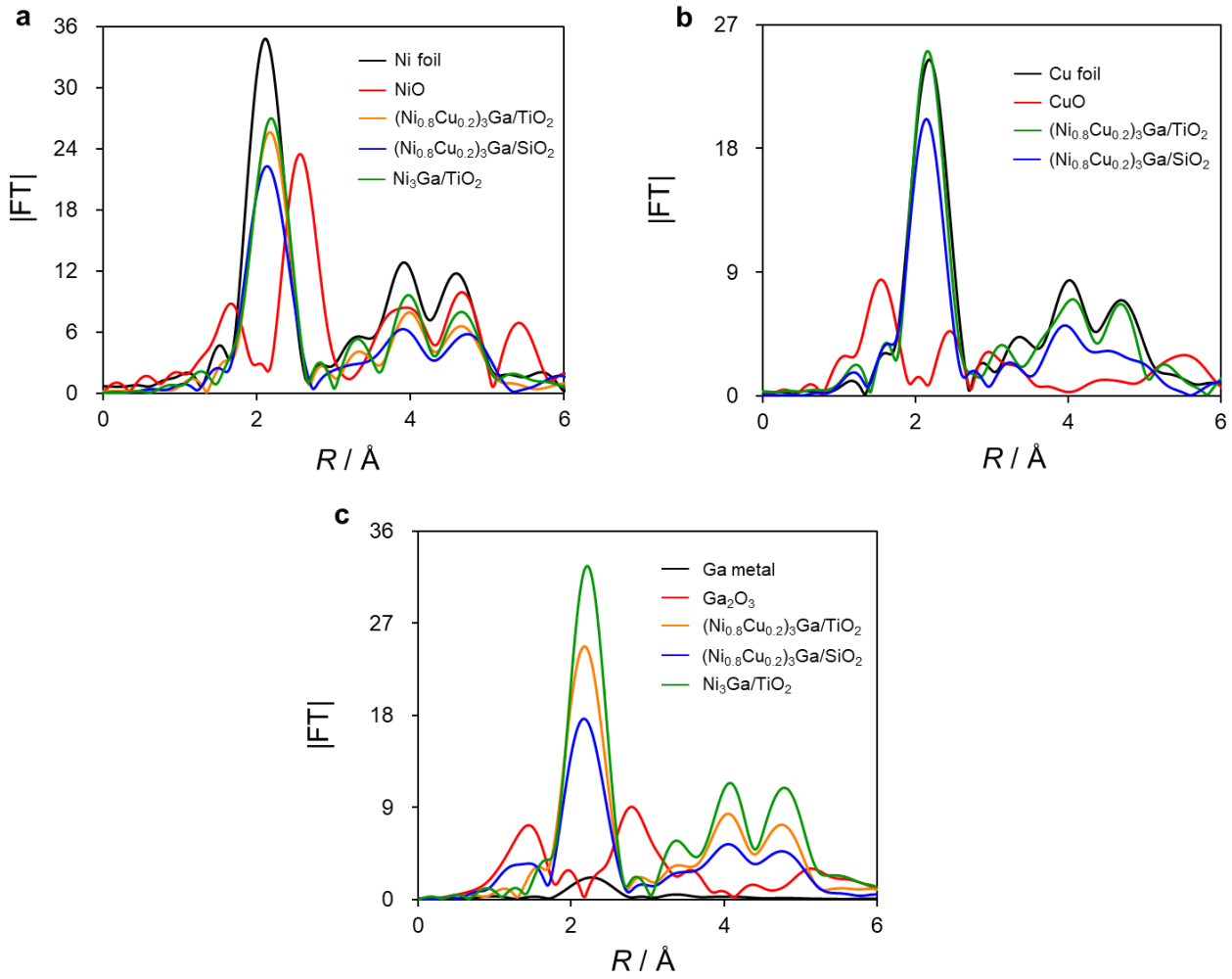

Figure 3.4. Fourier-transforms of EXAFS in (a) Ni, (b) Cu, and (c) Ga K-edge over $(Ni_{0.8}Cu_{0.2})_3Ga/TiO_2$, $(Ni_{0.8}Cu_{0.2})_3Ga/SiO_2$, Ni_3Ga/TiO_2. and reference compounds.

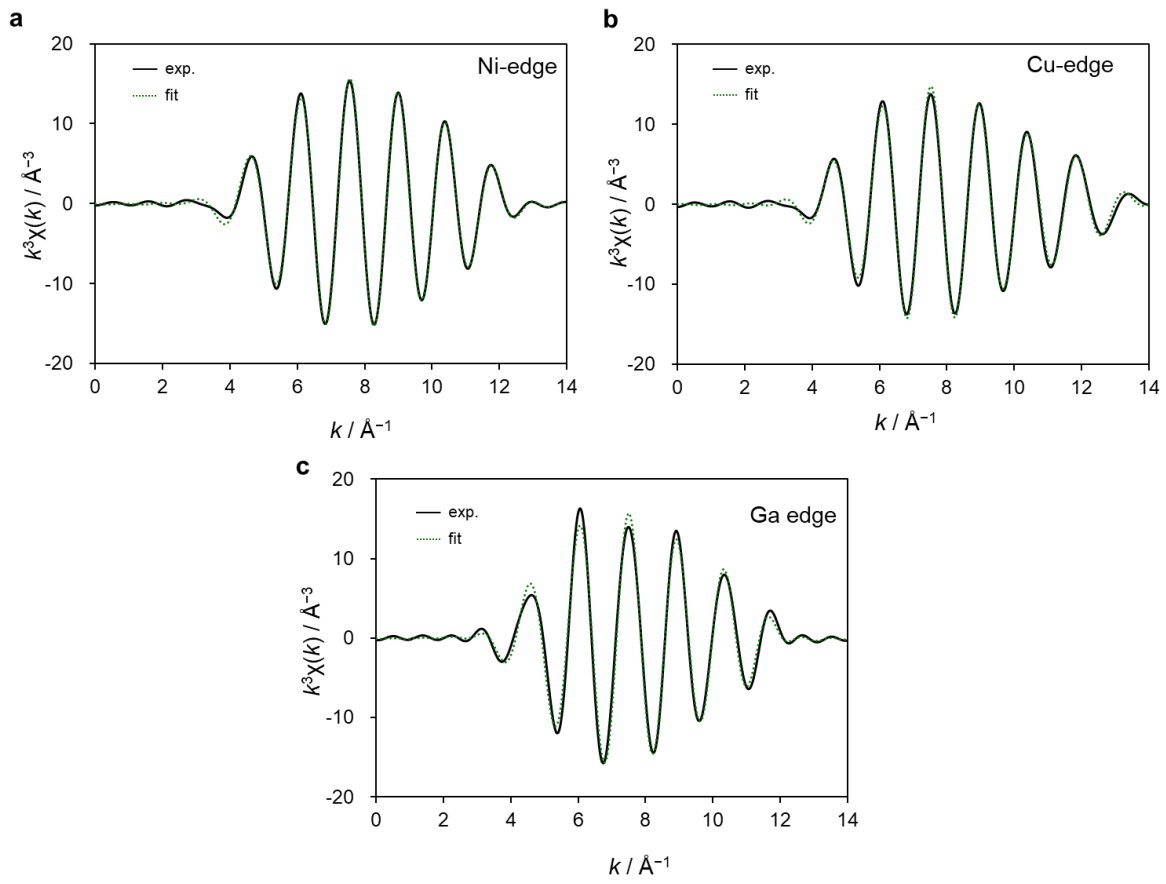

Figure 3.5. Curve-fitting results of (a) Ni (b) Cu and (c) Ga K-edge k^3-weighted EXAFS of $(Ni_{0.8}Cu_{0.2})_3Ga/TiO_2$. Solid and dashed lines indicate the results of simulation and experiment, respectively.

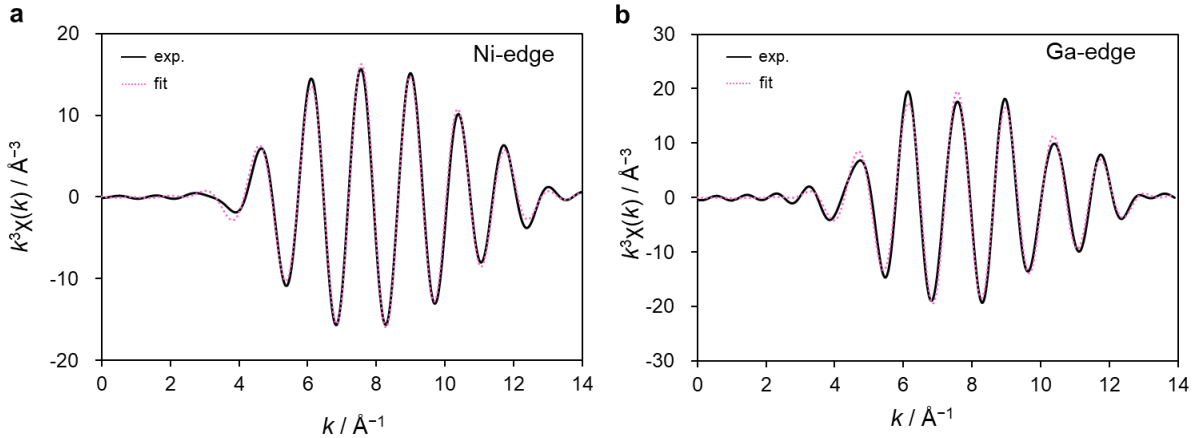

Figure 3.6. Curve-fitting results of (a) Ni and (b) Ga K-edge k^3-weighted EXAFS of Ni_3Ga/TiO_2. Solid and dashed lines indicate the results of simulation and experiment, respectively.

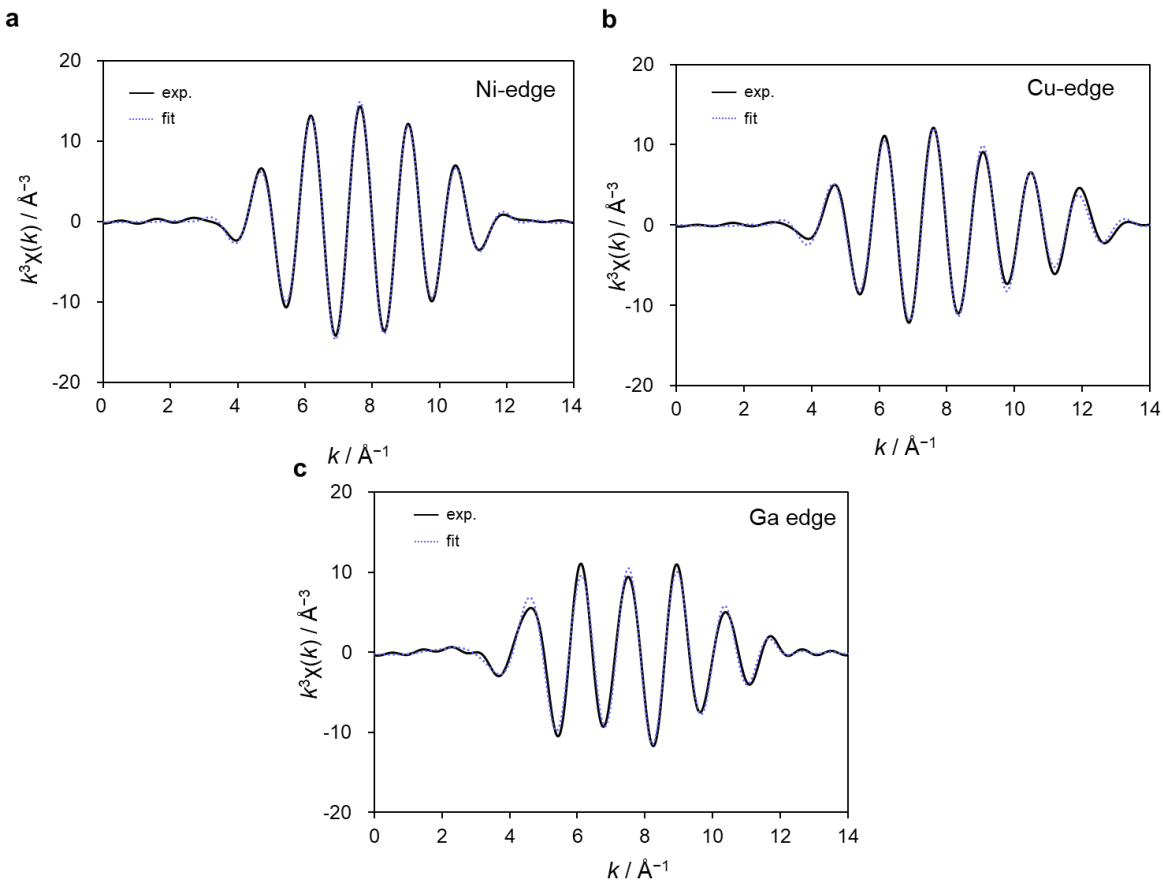

Figure 3.7. Curve-fitting results of (a) Ni (b) Cu and (c) Ga K-edge k^3-weighted EXAFS of $(Ni_{0.8}Cu_{0.2})_3Ga/SiO_2$. Solid and dashed lines indicate the results of simulation and experiment, respectively.

Table 3.2. Summary of the EXAFS curve fitting for $(Ni_{0.8}Cu_{0.2})_3Ga/TiO_2$, $(Ni_{0.8}Cu_{0.2})_3Ga/SiO_2$, Ni_3Ga/TiO_2 catalysts and reference.

Sample	Edge	Shell	S_o^2	CN	r (Å)	ΔE_o (eV)	σ^2 (Å^2)	R-factor
Ni foil	Ni k	Ni-Ni	0.846	12	2.48±0.01	5.43±0.7	0.00621	0.003
Cu foil	Cu k	Cu-Cu	0.918	12	2.54±0.02	6.26±0.9	0.0088	0.005
		Ga-O		3	1.91±0.09		0.00657	
Ga_2O_3	Ga k	Ga-O	1.316	1	2.12±0.25	6.84±1.8	0.00361	0.014
		Ga-Ga		2	3.05±0.01		0.00338	
$(Ni_{0.8}Cu_{0.2})_3Ga/TiO_2$	Ni k	Ni-Ga	0.846	3.50±0.99	2.46±0.07	5.40±1.5	0.00415	0.003
		Ni-Ni(Cu)		7.00±0.99	2.58±0.08		0.00472	
	Cu k	Cu-Ga	0.918	2.79±0.48	2.49±0.04	2.81±1.8	0.00275	0.008
		Cu-Cu(Ni)		8.38±0.48	2.60±0.04		0.00799	
	Ga k	Ga-O	1.316	2.11±0.29	2.03±0.20	0.65±1.7	0.0698	0.005
		Ga-Ni(Cu)		8.46±0.28	2.54±0.00		0.00914	
$(Ni_{0.8}Cu_{0.2})_3Ga/SiO_2$	Ni k	Ni-Ga	0.846	3.29±0.64	2.43±0.11	4.51±1.1	0.00185	0.018
		Ni-Ni(Cu)		6.58±0.64	2.57±0.04		0.00323	
	Cu k	Cu-Ga	0.918	3.59±0.93	2.29±0.24	9.38±2.3	0.02631	0.01
		Cu-Cu(Ni)		10.8±0.93	2.50±0.05		0.00953	
	Ga k	Ga-O	1.316	1.47±0.20	1.81±0.01	1.91±1.6	0.00796	0.02
		Ga-Ni(Cu)		5.89±0.20	2.54±0.00		0.00897	
Ni_3Ga/TiO_2	Ni k	Ni-Ga	0.846	3.51±1.22	2.45±0.09	6.27±1.9	0.00421	0.006
		Ni-Ni		7.03±1.23	2.57±0.04		0.00389	
	Ga k	Ga-O	1.316	2.28±1.10	1.79±0.04	5.20±1.5	0.13945	0.021
		Ga-Ni		9.11±1.12	2.53±0.00		0.00811	

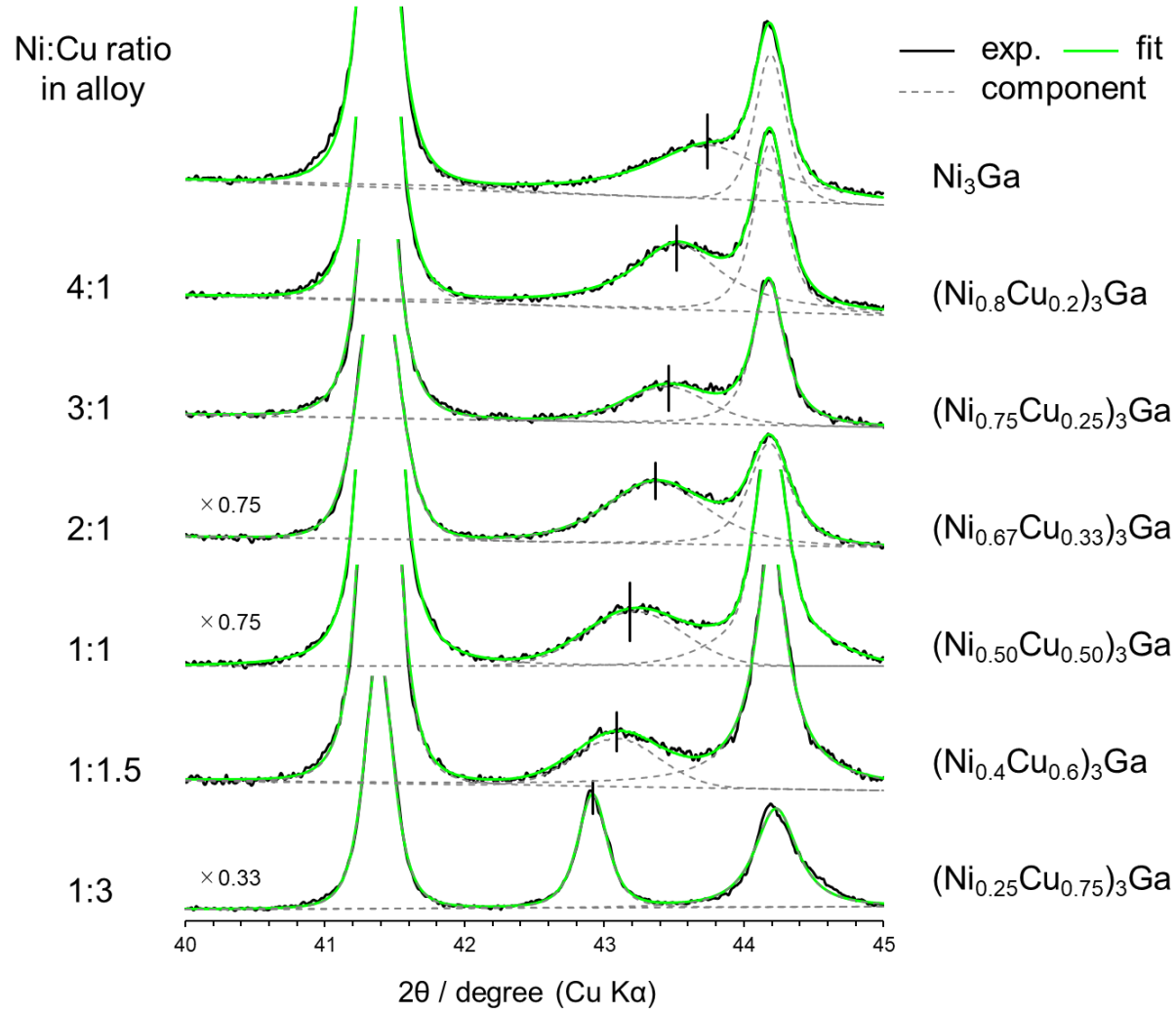

Figure 3.8. XRD analysis for $(Ni_{1-x}Cu_x)_3Ga/TiO_2$ (x = 0, 0.2, 0.25, 0.33, 0.5, 0.6, 0.75) catalysts. Vertical solid lines indicate the diffraction angles of the corresponding $(Ni_{1-x}Cu_x)_3Ga$ phases.

3.3.2 Catalytic performance in acetylene semi-hydrogenation

Next, the synthesized $(Ni_{1-x}Cu_x)_3Ga/TiO_2$ catalysts were tested in acetylene semi-hydrogenation in the absence of excess ethylene. Figure 3.9a summarizes their catalytic performances. As universal and standard scales for activity, apparent activation energy (E_a) and the temperature in which acetylene conversion reached 50% (T_{50}) were employed, respectively. The catalytic activity exhibited a volcano-type trend with respect to the Cu content with x = 0.25–0.33 as the best. Figures 3.9b and 3.9c show the temperature dependence of acetylene conversion and ethylene selectivity, respectively, using the representative catalysts, Ni_3Ga/TiO_2, $(Ni_{0.8}Cu_{0.2})_3Ga/TiO_2$, and $(Ni_{0.67}Cu_{0.33})_3Ga/TiO_2$. Owing to the remarkable

enhancement in catalytic activity by Cu doping, the temperature required for the complete conversion drastically decreased from 230°C to 150°C and 120°C, respectively. Moreover, ethylene selectivity was improved by Cu doping, particularly in a low-temperature region (<150°C; i.e., 90.5% → 96.2% at 150°C for $x = 0.2$). We also checked the carbon balance (C_b) in the reaction (the temperature dependencies of acetylene conversion, ethylene selectivity, and carbon balance are shown in Figure 3.10). Importantly, a significant decrease in C_b was observed when $x \geq 0.25$ (Figure 3.9a), probably because extra Cu caused oligomerization to form green oil. Therefore, we chose $x = 0.2$ as the optimal Cu content because it afforded the satisfactorily high activity with minimum oligomerization.

A long-term stability test was conducted at the near-complete conversion of acetylene, revealing that rapid deactivation occurred for Ni_3Ga and $(Ni_{0.67}Cu_{0.33})_3Ga$, whereas no deactivation was observed for $(Ni_{0.8}Cu_{0.2})_3Ga$ after at least 60 h (Figure 3.9d). Thus, the activity, selectivity, and stability were significantly increased by the catalyst design based on the pseudo-binary alloy and the appropriate amount of Cu doping.

We also examined the catalytic performance in the presence of excess ethylene, a practical condition (C_2H_2:H_2:C_2H_4:He = 1:10:5:19 mLmin^{-1}), in which activity, selectivity, and stability (stable up to 100 h) trends similar to those in Figures 3.9b–3.9d were obtained (Figure 3.11–3.12). Figures 3.9e and 3.9f summarize the comparison of the catalytic performance in acetylene semi-hydrogenation at low temperatures (≤200°C) with reported systems using 3d transition metal-based catalysts[12-29] (see Table 3.3 and Figures 3.13–3.14 for details). The $(Ni_{0.8}Cu_{0.2})_3Ga/TiO_2$ catalyst exhibited outstandingly high specific activity and long-term stability while retaining excellent ethylene selectivity. It is known that catalytic activity and selectivity/stability are typically in tradeoff because excess activity tends to induce undesired side reactions. Therefore, satisfying the upper right region in Figures 3.9e and 3.9f is a challenging task. In this context, the development of a Ni-based catalyst efficiently working within a low-temperature region is highly innovative.

As a control experiment, we prepared $(Ni_{0.8}Cu_{0.2})_3Ga/SiO_2$ to investigate the suitability of supports for this catalysis. XRD and XAFS confirmed the formation of a pseudo-binary alloy structure in a similar way, as mentioned above (Table 3.2 and Figures 3.3–3.4, 3.7, and 3.15).

The Ni K-edge XANES spectra revealed a slight decrease in the electron density of Ni changing from TiO_2 to SiO_2 (Figure 3.3a). Using a SiO_2 support, the catalytic activity in acetylene semi-hydrogenation increased (100% conversion at 130°C), whereas ethylene selectivity significantly decreased (50%–75%, Figure 3.16). This trend was more prominent in the presence of excess ethylene, where over-hydrogenation to ethane markedly proceeded (the selectivity was −18% at the lowest, Figure 3.17). Thus, SiO_2 was unsuitable for selective hydrogenation presumably owing to the reduction in the electron density of Ni. A plausible interpretation is that the low electron density of Ni renders it cationic and strengthens the adsorption of acetylene and ethylene, resulting in high activity but low selectivity. In addition, a series of $(Ni_{0.8}M_{0.2})_3Ga/TiO_2$ catalysts using 3d transition metals other than Cu (M = Fe, Co, Zn) were prepared and similarly tested (Figure 3.18). However, no catalyst showed superior performance to that of $(Ni_{0.8}Cu_{0.2})_3Ga/TiO_2$, confirming the suitability of Cu as a modifier for Ni.

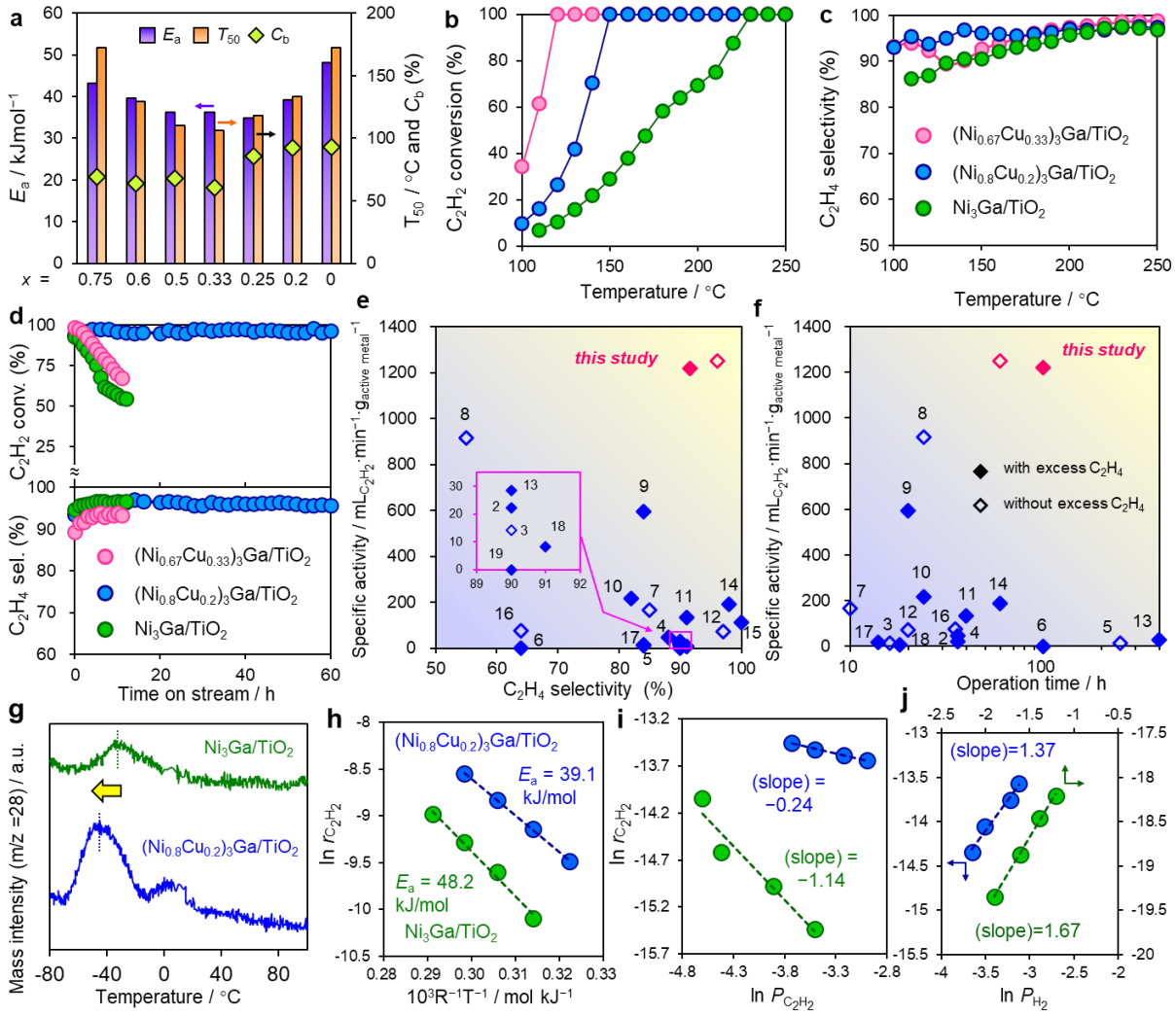

Figure 3.9. Catalytic performance and mechanistic studies. (a) E_a, T_{50}, and C_b obtained in acetylene semi-hydrogenation over a series of $(Ni_{1-x}Cu_x)_3Ga/TiO_2$ catalysts. (b) C_2H_2 conversion and (c) C_2H_4 selectivity as a function of the reaction temperature in the absence of ethylene (C_2H_2:H_2:He = 1:10:39 mLmin^{-1}). (d) Long-term stability test (Ni_3Ga, 220°C; $(Ni_{0.8}Cu_{0.2})_3Ga$, 150°C; $(Ni_{0.67}Cu_{0.33})_3Ga$, 145°C) in the absence of ethylene. (e,f) Comparison with reported systems using 3d transition metal-based catalysts (<200°C): specific activity at high acetylene conversion (>80%) vs. (e) ethylene selectivity and (f) operation time (numbers correspond to the entries in Table 3.3 and Figures 3.13–3.14). (g) C_2H_4-TPD profiles. (h) Arrhenius-type plots. (i,j) Reaction orders of (i) acetylene (P_{C2H2}) and (j) hydrogen partial pressures.

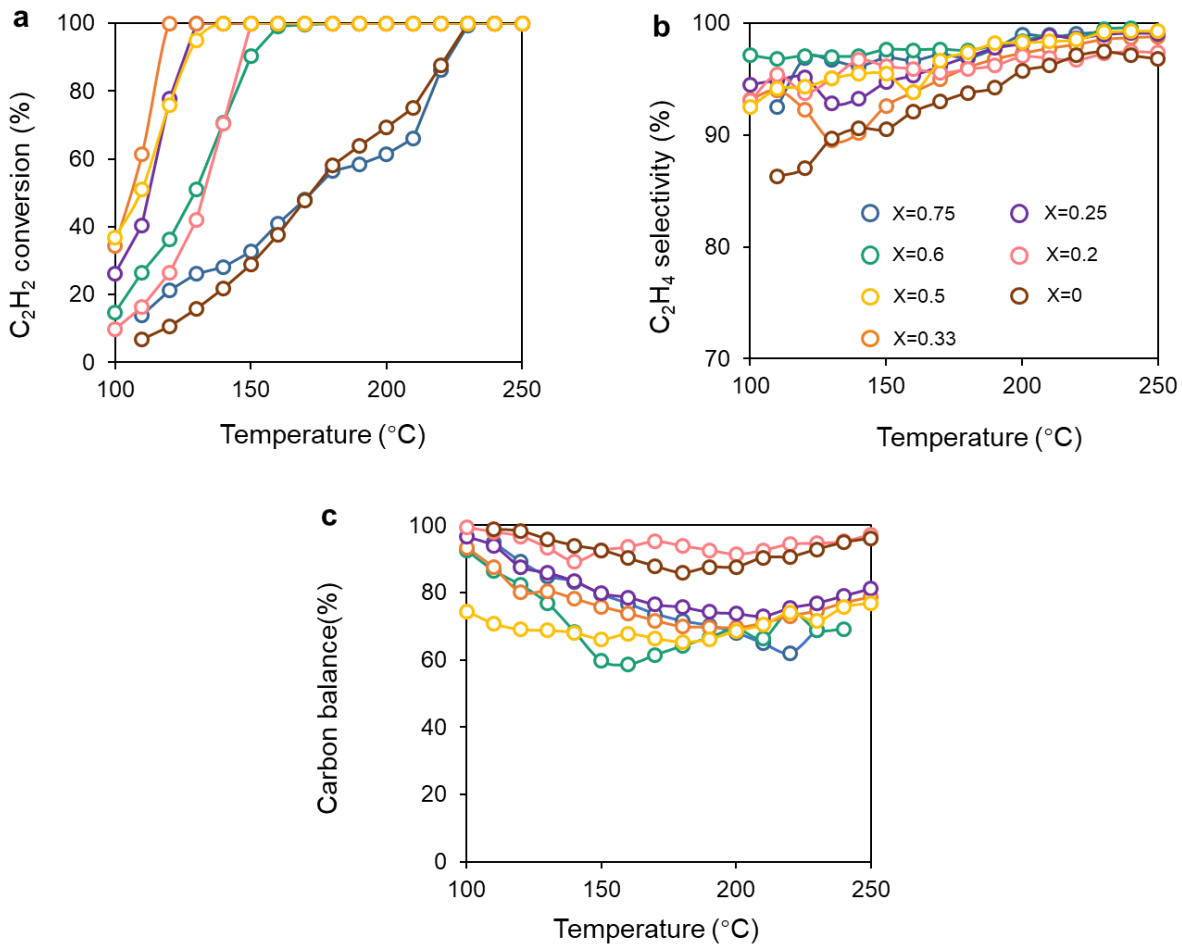

Figure 3.10. (a) C_2H_2 conversion, (b) C_2H_4 selectivity and (c) carbon balance as a function of reaction temperature over $(Ni_{1-x}Cu_x)_3Ga/TiO_2$.

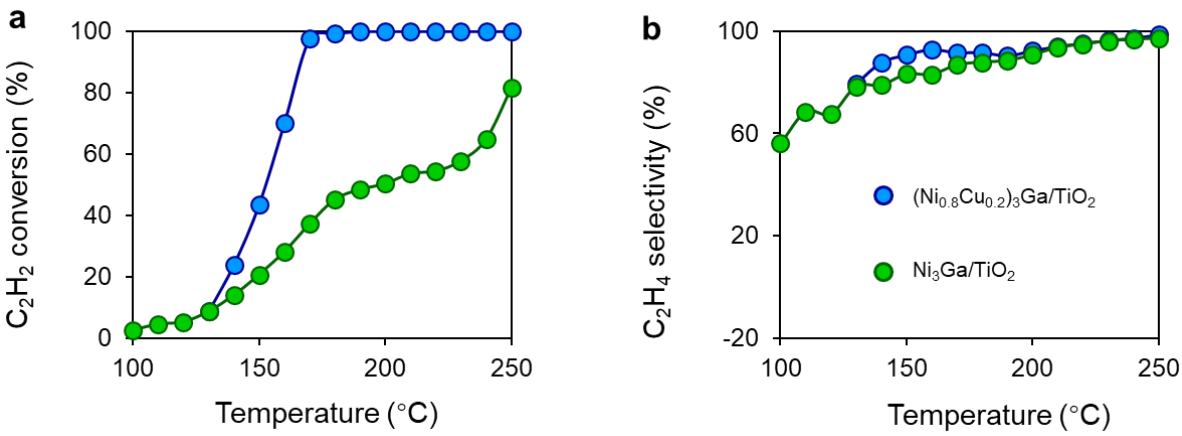

Figure 3.11. (a) C_2H_2 conversion and (b) C_2H_4 selectivity as a function of reaction temperature in the presence of ethylene (C_2H_2:H_2:He:C_2H_4 = 1:10:39:5 $mLmin^{-1}$) over $(Ni_{0.8}Cu_{0.2})_3Ga/TiO_2$ and Ni_3Ga/TiO_2.

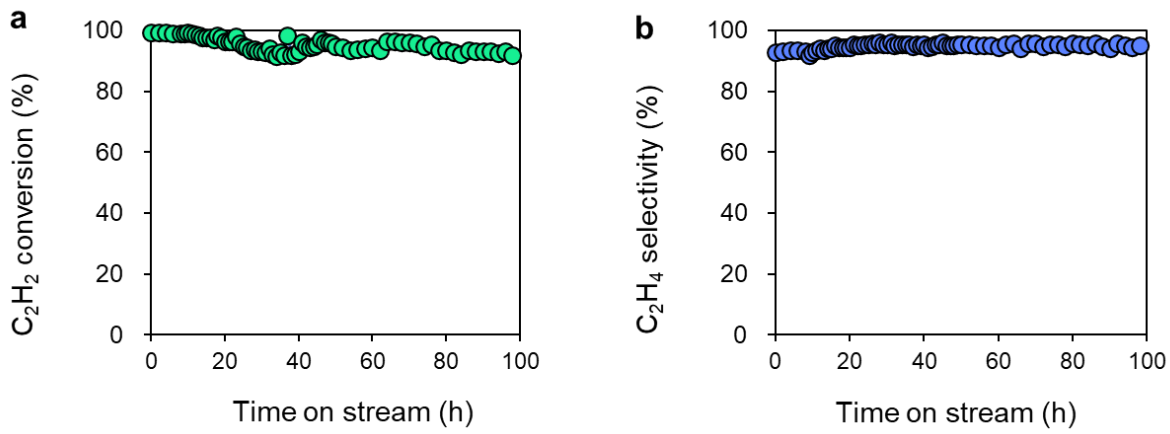

Figure 3.12. Long-term stability test using $(Ni_{0.8}Cu_{0.2})_3Ga/TiO_2$ in the presence of excess ethylene (C_2H_2:H_2:He:C_2H_4 = 1:10:39:5 mLmin^{-1}) at 180°C. (a) C_2H_2 conversion and (b) C_2H_4 selectivity.

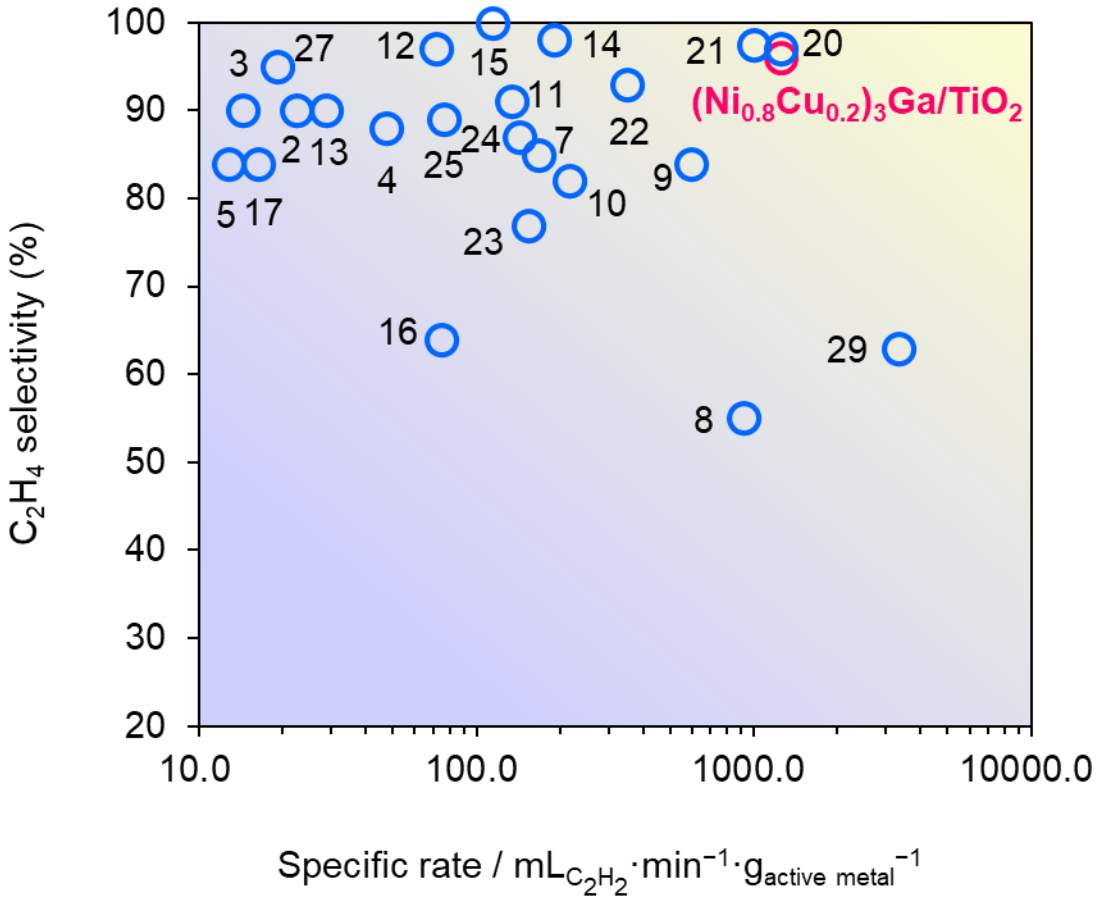

Figure 3.13. Relationship between the specific activity and ethylene selectivity at high acetylene conversion (>80%) for 3d transition metal-based catalysts that were reported in literature and developed in this study. Numbers correspond to the entries in Table 3.3.

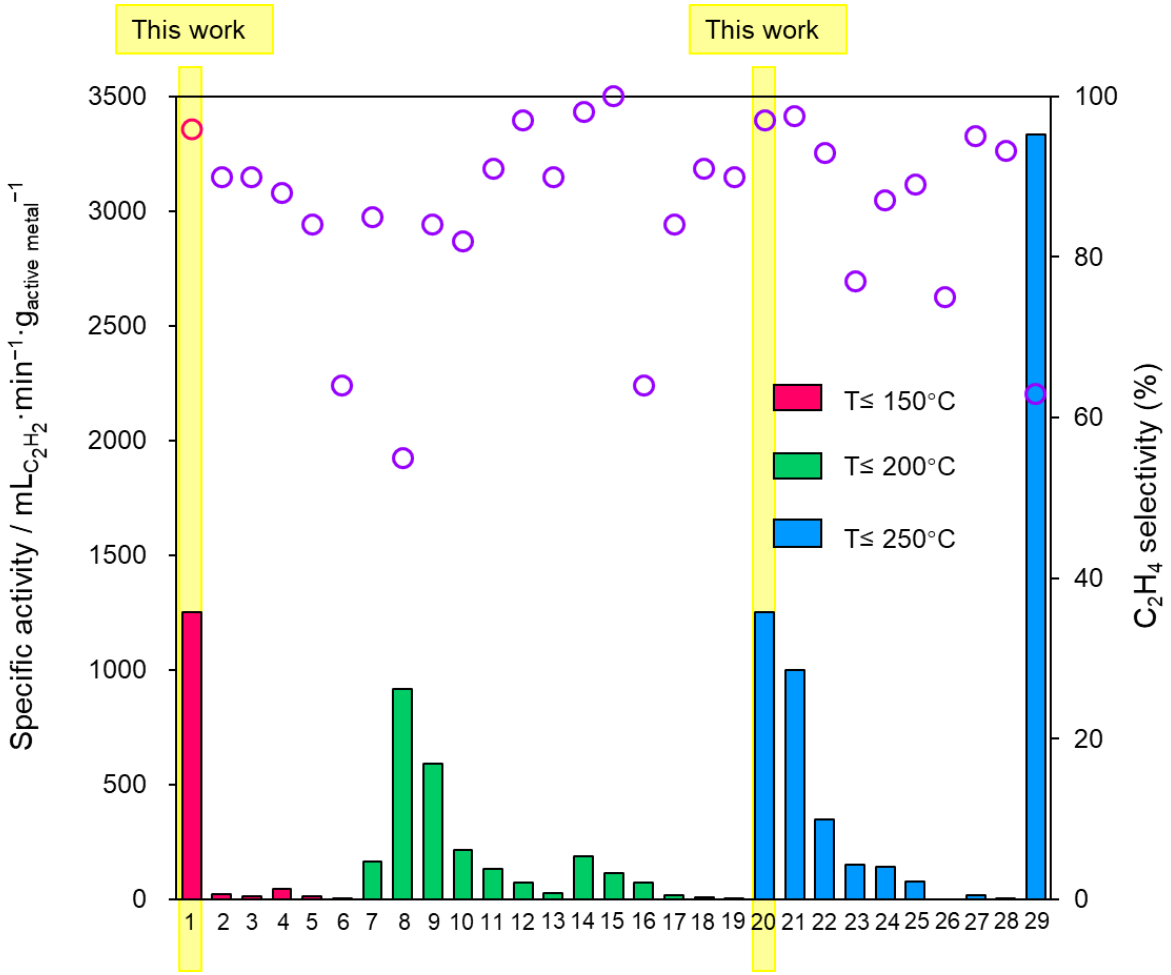

Figure 3.14. Relationship between the specific activity and ethylene selectivity at high acetylene conversion (>80%) at different reaction temperature for 3d transition metal-based catalysts that were reported in literature and developed in this study. Numbers correspond to the entries in Table 3.3.

Table 3.3. Summary of reaction conditions and catalytic performances in acetylene semi-hydrogenation using 3d transition metal-based catalysts that were reported in literature and developed in this study.

entry	catalyst	loading (wt%)	amount / mg	C_2H_2 flow /mLmin^{-1}	C_2H_2 : H_2 : C_2H_4	total flow /mLmin^{-1}	GHSV mLg^{-1}h^{-1}	/ conv. (%)	sel. (%)	temp. / °C	specific rate mL$_{C2H2}$min^{-1}g$_M^{-1}$	/ Operation time (h)	ref
1	$(Ni_{0.8}Cu_{0.2})_3Ga/TiO_2$	1	80	1	1 : 10 : 0	50	37500	100	96	150	1250.0	60	This work
2	$Ni_3GaC_{0.5}$/MgAl LDH	14.88	150	0.5	0.5:2.5:10	100	40000	100	90	110	22.4	36	[30]
3	Ni_1MoS/Al_2O_3	3.5	500	0.2475	1:20:0	165	19800	100	90	125	14.1	16	[31]
4	NiCu/MgAl-MMO	9.58	100	0.558	1 : 2 : 103	166	100500	81	88	140	47.2	36	[322]
5	$Cu(OH)_2$	78.9	100	1	1 : 9 : 0	10	6000	100	84	110	12.7	250	[33]
6	Cu_2O	88.8	100	0.045	1 : 22 : 197	10	6000	100	64	120	0.5	100	[34]
7	$Ni_3ZnC_{0.7}$/C	12	50	1	1:15:0	100	120000	100	85	165	166.7	10	[35]
8	$AgNi_{0.5}/SiO_2$	1.09	30	0.3	1:20:0	30	60000	100	55	180	917.4	24	[36]
9	Ni/g-C_3N_4-T	1	50	0.3	1:10:20	30	36000	99	84	175	594.0	20	[37]
10	NiGa/MgAl-LDH	10	50	1.2	1 : 10 : 20	120	144000	90	82	190	216.0	24	[38]
11	$0.5Cu/Al_2O_3$	0.5	300	0.2	1 : 10 : 50	20	4000	100	91	188	133.3	40	[39]
12	Na-Ni/CHA	3.5	200	0.5	1 : 16 : 0	50	15000	100	97	170	71.4	20	[40]
13	Ni_1Cu_2/g-C_3N_4	3.5	150	0.15	1 : 10 : 50	30	12000	100	90	160	28.6	400	[41]
14	Cu_1/ND	0.25	200	0.1	1 : 10 : 20	10	3000	95	98	200	190.0	60	[42]
15	Ni–CeO_2	1.54	200	0.35	1 : 70 : 4	70	21000	100	100	200	113.6	3	[43]
16	Ni_6In/SiO_2	8	500	3	1 : 10 : 0	300	36000	100	64	200	75.0	35	[44]
17	$Al_{13}Fe_4$	38.9	20	0.15	1 : 10 : 100	30	90000	85	84	200	16.4	14	[45]
18	Ni-SAs/N-C	5.67	400	0.2	1 : 20 : 100	40	6000	96	91	200	8.5	18	[46]
19	Co_2FeGe	47.8	400	0.03	1 : 400 : 100	30	4500	91	90	200	0.1		[47]
20	Ni_3Ga/TiO_2	1	80	1	2 : 10 : 0	50	37500	100	97	230	1250.0	1	This work
21	NiCuFeGaGe/SiO_2	1	100	1	1 : 10 : 0	50	30000	100	98	220	1000.0	28	[48]
22	NiCu/ZrO_2	4.6	25	0.4	1:10:20	40	96000	100	93	220	347.8	15	[49]
23	$Ni_3Ga/MgAl_2O_4$	2	100	0.33	1 : 20 : 100	67	144000	92	77	220	153.3	24	[50]
24	Ni/MCM-41	25	100	3.7	1 : 2 : 0	66.6	40000	96	87	240	142.2	10	[51]
25	Ni_3Ge/MCM-41	3.2	1500	3.9	1 : 2.1 : 0	29	1160	94	89	250	76.4		[52]
26	$Cu_{2.75}Ni_{0.25}Fe$	-	150	0.63	1.5:4.5:8.1	42	16800	100	75	250		30	[53]
27	$Cu/Fe_{0.16}MgO_x$	18.0	200	0.69	1 :100 : 3	209	62700	100	95	215	19.2	40	[54]
28	NiSb/MgAl LDH	8.58	300	0.15	0.5:2.5:30	30	6000	100	93.2	260	5.8	48	[55]
29	$NiCu_{0.125}$/MCM-41	1	100	3.3	1 : 3 : 0	13.3	8000	100	63	250	3333.3	9	[56]

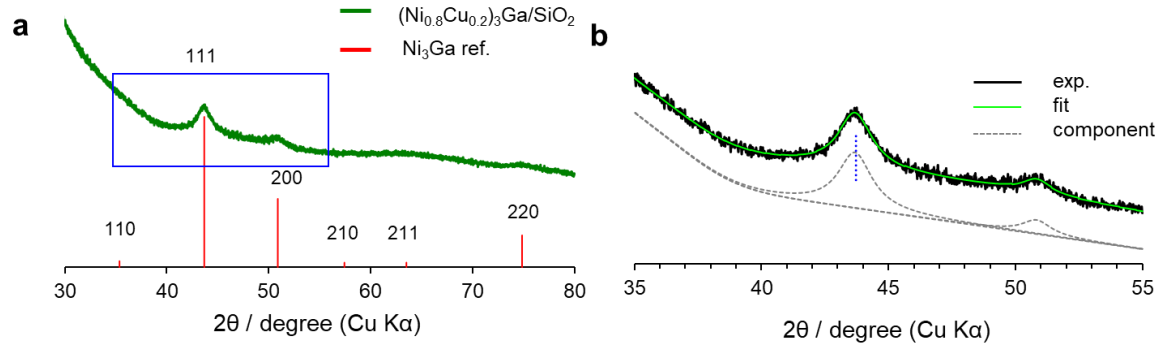

Figure 3.15. (a) XRD pattern of $(Ni_{0.8}Cu_{0.2})_3Ga/SiO_2$ and (b) its magnification indicated as the bule square. The center of 111 diffraction was at 43.72° (blue dotted line), which agreed with that of $(Ni_{0.8}Cu_{0.2})_3Ga/TiO_2$ (43.74°).

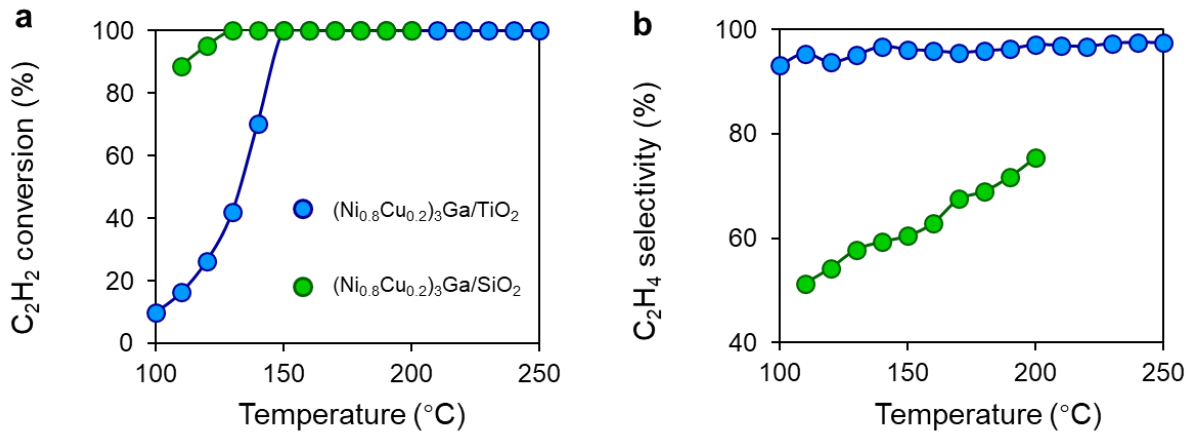

Figure 3.16. (a) C_2H_2 conversion and (b) C_2H_4 selectivity as a function of reaction temperature in the absence of ethylene (C_2H_2:H_2:He = 1:10:39 mLmin^{-1}) over $(Ni_{0.8}Cu_{0.2})_3Ga/TiO_2$ and $(Ni_{0.8}Cu_{0.2})_3Ga/SiO_2$.

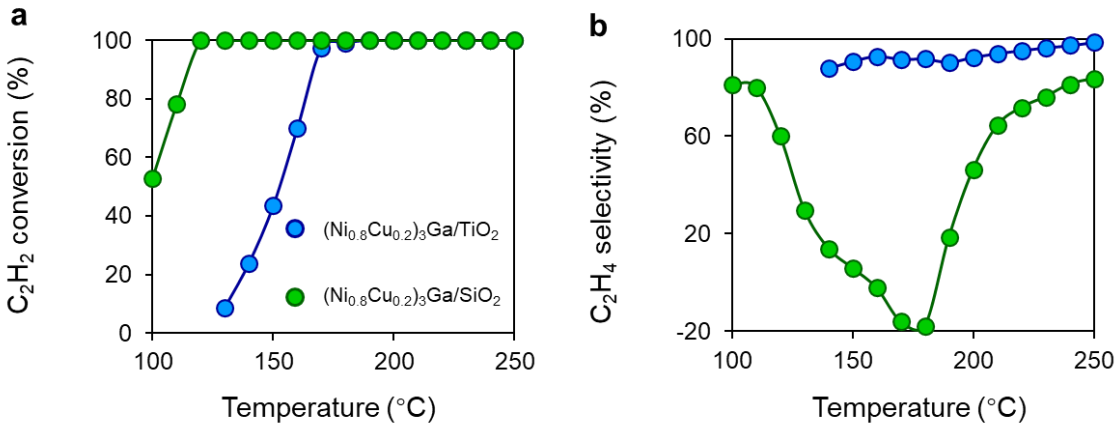

Figure 3.17. (a) C_2H_2 conversion and (b) C_2H_4 selectivity as a function of reaction temperature in the presence of ethylene (C_2H_2:H_2:He:C_2H_4 = 1:10:39:5 mLmin^{-1}) over $(Ni_{0.8}Cu_{0.2})_3Ga/TiO_2$ and $(Ni_{0.8}Cu_{0.2})_3Ga/SiO_2$.

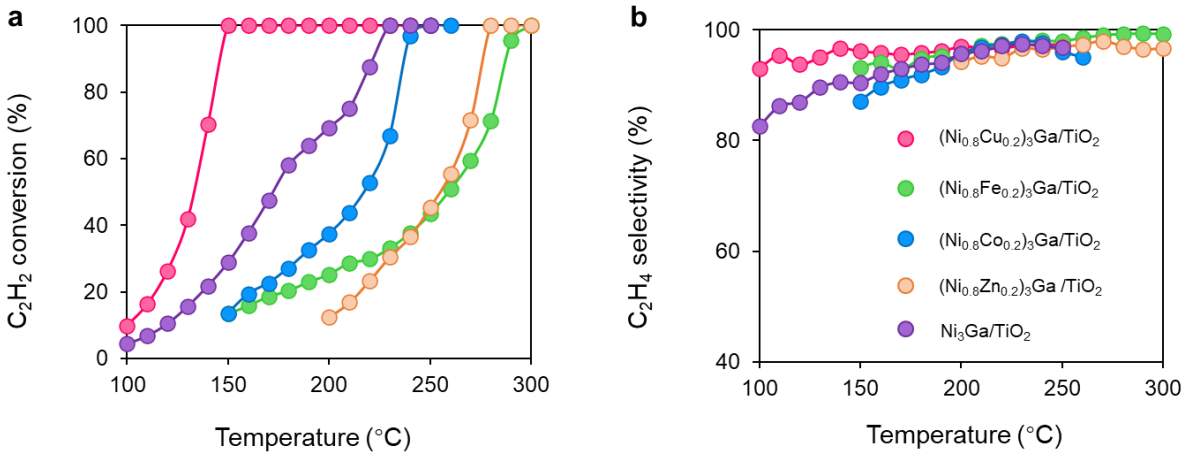

Figure 3.18. (a) C_2H_2 conversion and (b) C_2H_4 selectivity as a function of reaction temperature over $(Ni_{0.8}M_{0.2})_3Ga/TiO_2$ (M = Cu, Fe, Co, Zn) and Ni_3Ga/TiO_2.

3.3.3 Mechanistic study

To understand the role of Cu doping in enhanced catalysis, we conducted a mechanistic study. First, the temperature-programmed desorption of ethylene (C_2H_4-TPD) was performed using Ni_3Ga/TiO_2 and $(Ni_{0.8}Cu_{0.2})_3Ga/TiO_2$. As shown in Figure 3.9g, Ni_3Ga showed an ethylene desorption peak centered at −32°C, whereas that of $(Ni_{0.8}Cu_{0.2})_3Ga$ was observed at −45°C. This indicated that ethylene adsorption was weakened by Cu doping, which correlated with enhanced ethylene selectivity. Figure 3.9h shows the Arrhenius plots obtained during acetylene semi-hydrogenation and the corresponding E_a (corresponding to those in Figure 3.9a), suggesting that the energy barrier of acetylene hydrogenation to ethylene was lowered by doping an appropriate amount of Cu. The reaction orders of acetylene and hydrogen's partial pressures ($P_{C_2H_2}$ and P_{H_2}, respectively) on the overall conversion rate of acetylene were also estimated ($r = kP_{C_2H_2}{}^{\alpha}P_{H_2}{}^{\beta}$, Figures 3.9i and 3.9j). For Ni_3Ga/TiO_2, α and β were largely negative (−1.14) and positive (1.67), respectively. This indicated that the strong adsorption of acetylene on Ni competes with H_2 adsorption and/or activation, which is a typical trend in acetylene semi-hydrogenation. Conversely, for $(Ni_{0.8}Cu_{0.2})_3Ga/TiO_2$, α significantly increased to near zero (−0.24), while β slightly decreased (1.37). Therefore, it was likely that Cu doping to Ni markedly weakened acetylene adsorption, thereby facilitating H_2 adsorption/activation. This may have been due to the moderate dilution of the Ni–Ni ensembles (i.e., Ni_3 hollow sites

on the (111) plane) by Cu. Considering these results, a possible interpretation for the significant enhancement in catalytic activity is the double promotion of the reaction rate by increasing the rate constant (lower E_a) and the hydrogen coverage.

Next, we investigated the origin of the side reaction yielding ethane using the temperature-programmed surface reaction of ethylene hydrogenation (C_2H_4/H_2-TPSR) (Figure 3.19a). Unexpectedly, no ethane evolved from 30°C to 280°C for Ni_3Ga/TiO_2 and $(Ni_{0.8}Cu_{0.2})_3Ga/TiO_2$, implying that the over-hydrogenation of product ethylene hardly occurred on these catalysts. Therefore, the small amount of byproduct ethane observed in acetylene semi-hydrogenation appeared to be directly generated from acetylene, as often proposed as a side pathway via an ethylidene intermediate. Thus, the selectivity enhancement shown in Figure 3.9c may be attributed to the inhibition of this pathway by Cu doping. The C_2H_2-TPD experiment revealed that strongly adsorbed acetylene (assignable to di-σ-C_2H_2) observed on Ni_3Ga/TiO_2 disappeared when Cu was doped (Figure 3.19b). These results demonstrated that the active site tuning by Cu substitution accelerated the desired reaction and minimized the undesired side pathway owing to the change in adsorption behavior.

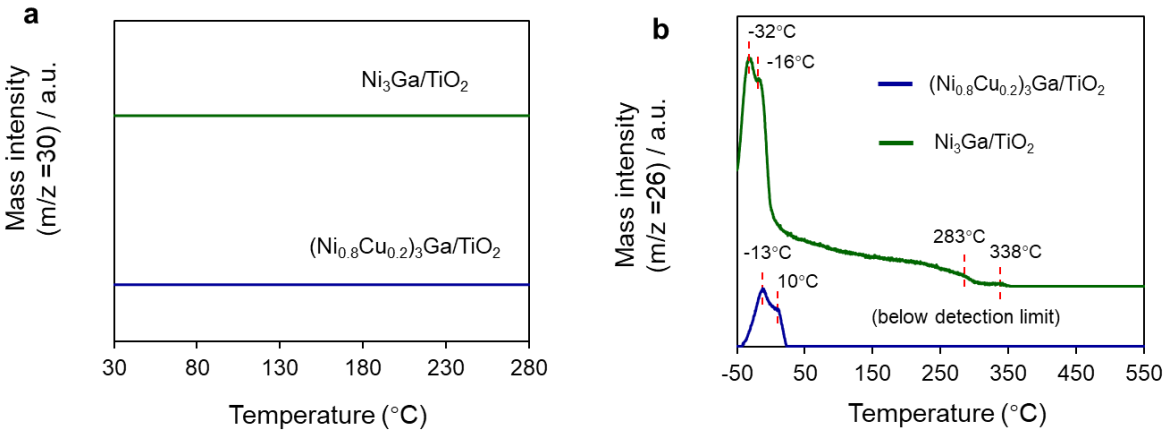

Figure 3.19. (a) Ethylene temperature programmed surface reaction profiles (TPSR) of the $(Ni_{0.8}Cu_{0.2})_3Ga/TiO_2$ and Ni_3Ga/TiO_2 catalysts for ethylene hydrogenation. (b) C_2H_2-TPD profiles of the $(Ni_{0.8}Cu_{0.2})_3Ga/TiO_2$ and Ni_3Ga/TiO_2 catalysts.

3.3.4 DFT calculation

Finally, we performed density functional theory (DFT) calculations to elucidate the roles of Cu substitution in the geometry and energetics of acetylene hydrogenation over the Ni-based catalysts. The Ni_3Ga (111) surface was considered as the parent reaction environment for the Cu substitution. As a model of $(Ni_{0.8}Cu_{0.2})_3Ga$ (111), a part of the Ni atoms in the two surface layers was randomly replaced with Cu so that the Ni/Cu ratio in the two layers was 4 (hereinafter referred to as Ni_3Ga(111)–Cu). The resulting Ni_2Cu ensembles were considered active sites for the stepwise hydrogenation of acetylene to ethylene and ethane (Figure 3.20a, see Figures 3.21–3.22 for details). Figure 3.20b summarizes the energy landscapes of the stepwise hydrogenation over the Ni-based catalysts. Overall, the adsorbate states were destabilized upon Cu substitution. However, the degree of destabilization differed depending on the conformation of the adsorbates. The higher the CN (atop, 1; bridge, 2; hollow, 3), the higher the destabilization. For example, the vinyl (C_2H_3) on the hollow and di-σ-C_2H_2 (C_2H_4) exhibited increases of 0.39 eV and 0.19 (0.21) eV, respectively, whereas the vinyl and ethyl on the top only exhibited minimal changes.

For the vinyl on the hollow, the coordinating carbon atom was off-centered to be slightly far from the Cu atom, resulting in a "2.5-fold-like" state and significant destabilization. This trend indicated that the ensemble effect by Cu efficiently tuned the adsorptivity[57]. Moreover, the minute energy change for the on-top adsorption on Ni suggested that the contribution of the ligand effect of Cu on Ni was extremely minor. For the transition states (TSs), the degree of destabilization was typically intermediate between the initial and final states. Consequently, the energy barrier of the hydrogen attack toward vinyl to form ethylene, i.e., the highest barrier from acetylene to ethylene (the rate-determining step in acetylene semi-hydrogenation), is decreased. The activation energies calculated for Ni_3Ga and Ni_3Ga–Cu (electronic and free energies) correlated with those obtained experimentally (Figure 3.20c). These results support the validity of the DFT model and reaction pathways/configurations considered for this study.

For the over-hydrogenation of ethylene, the difference in energy barriers of its desorption and over-hydrogenation (ΔE or ΔG) has been typically considered as a scale. Although the changes in the electronic energy of desorption exceeded those of over-hydrogenation, they significantly reduced when free energy was considered (Figure 3.20d) because desorption can

gain a large contribution of translational entropy. Owing to the large ΔG (>0.55 eV), ethylene over-hydrogenation appeared to hardly occur over Ni_3Ga and Ni_3Ga–Cu, correlating with the C_2H_4/H_2-TPSR results and again suggesting the involvement of direct hydrogenation to ethane via the ethylidene intermediate. The DFT calculation also revealed that the adsorbate states of ethylidene on the Ni_2Cu site of Ni_3Ga–Cu were considerably higher than those on the Ni_3 site of Ni_3Ga owing to the similar ensemble effect (Figure 3.23). This correlated with the C_2H_2-TPD results (the absence of strongly adsorbed C_2H_2) and probably contributed to the enhancement in ethylene selectivity by Cu doping.

Thus, the DFT study adequately explained the roles of Cu doping to Ni in tuning the active site geometry and the resulting catalytic performance, which was consistent with the experimental results. Based on the insights from the DFT calculation, the best x ratio to maximize the fraction of Ni_2Cu ensemble sites was 0.33. This also agrees with the highest activity obtained with this ratio. However, to retain the highest C_b for better stability, we chose an x of 0.2 as the optimal value for active site tuning as mentioned above.

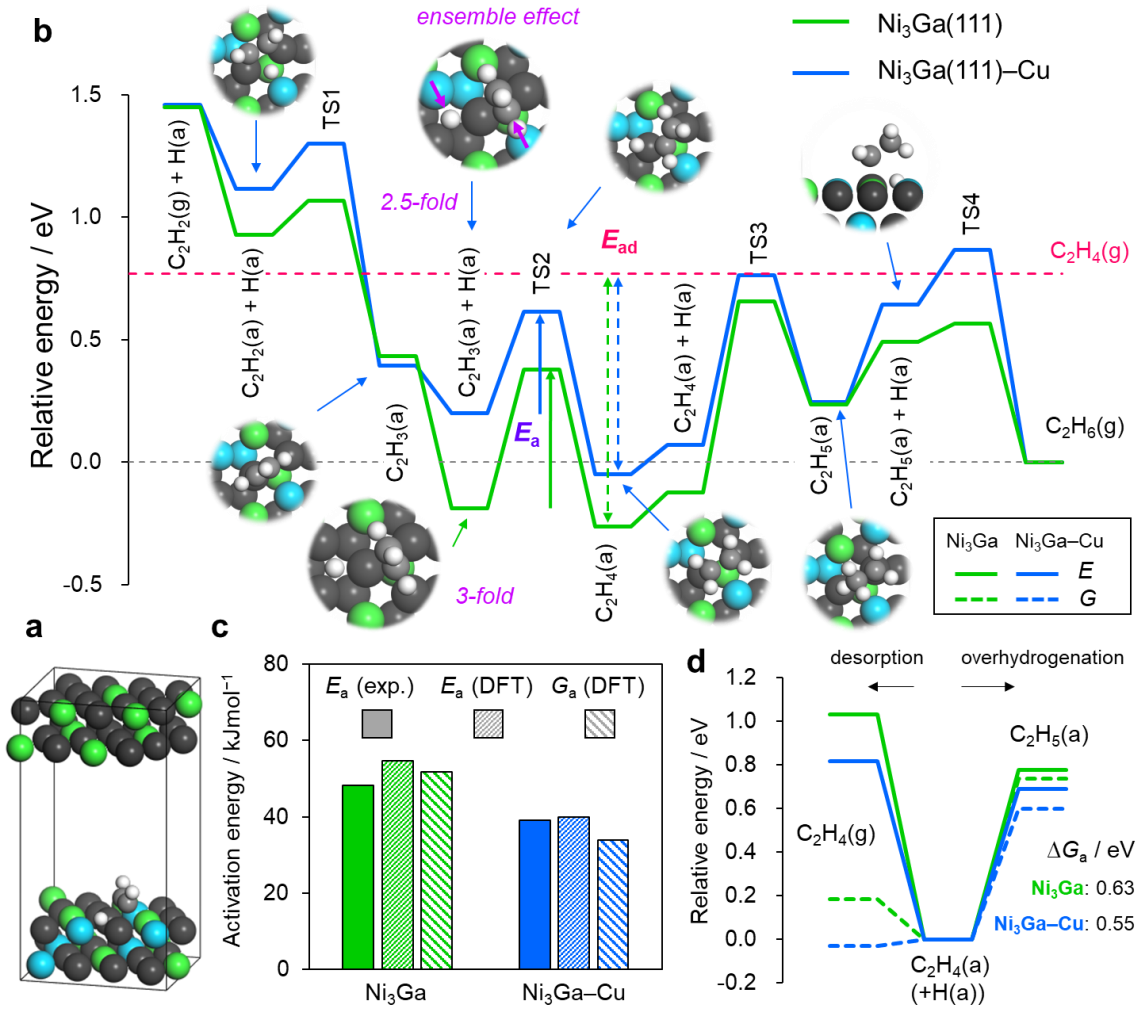

Figure 3.20. DFT calculations for acetylene hydrogenation. (a) Example of the optimized structure in the slab model: C_2H_2(a)+H(a) on Ni_3Ga (111)–Cu. (b) Energy landscapes of the stepwise hydrogenation from acetylene to ethane. Sum of the bare slab and gas-phase C_2H_6 was set to zero in energy. (c) Comparison of activation energies. d Energy diagrams of ethylene desorption and over-hydrogenation.

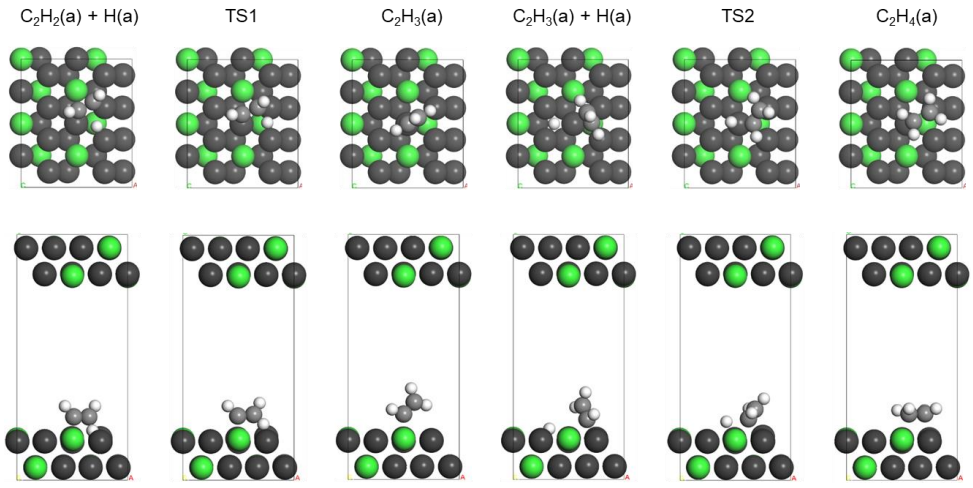

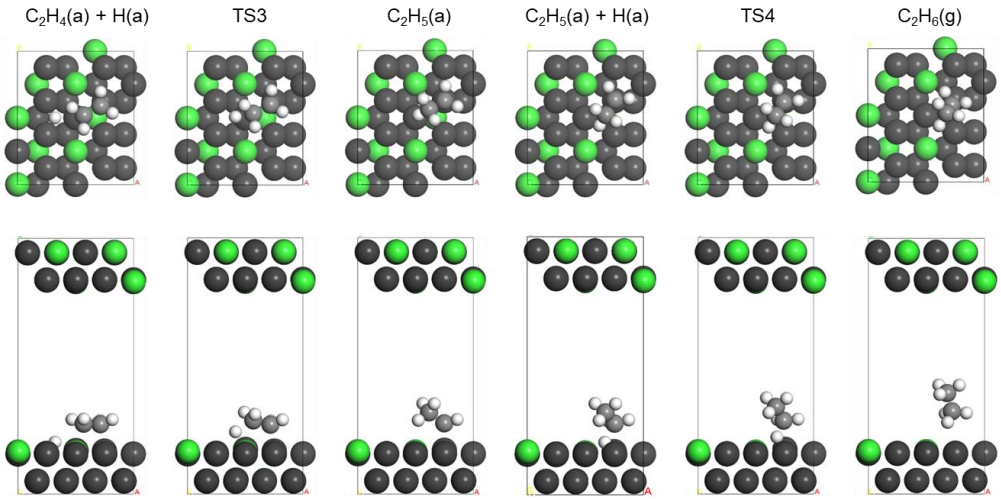

Figure 3.21. Optimized structures of the slab and adsorbates in acetylene hydrogenation to ethane over $Ni_3Ga(111)$.

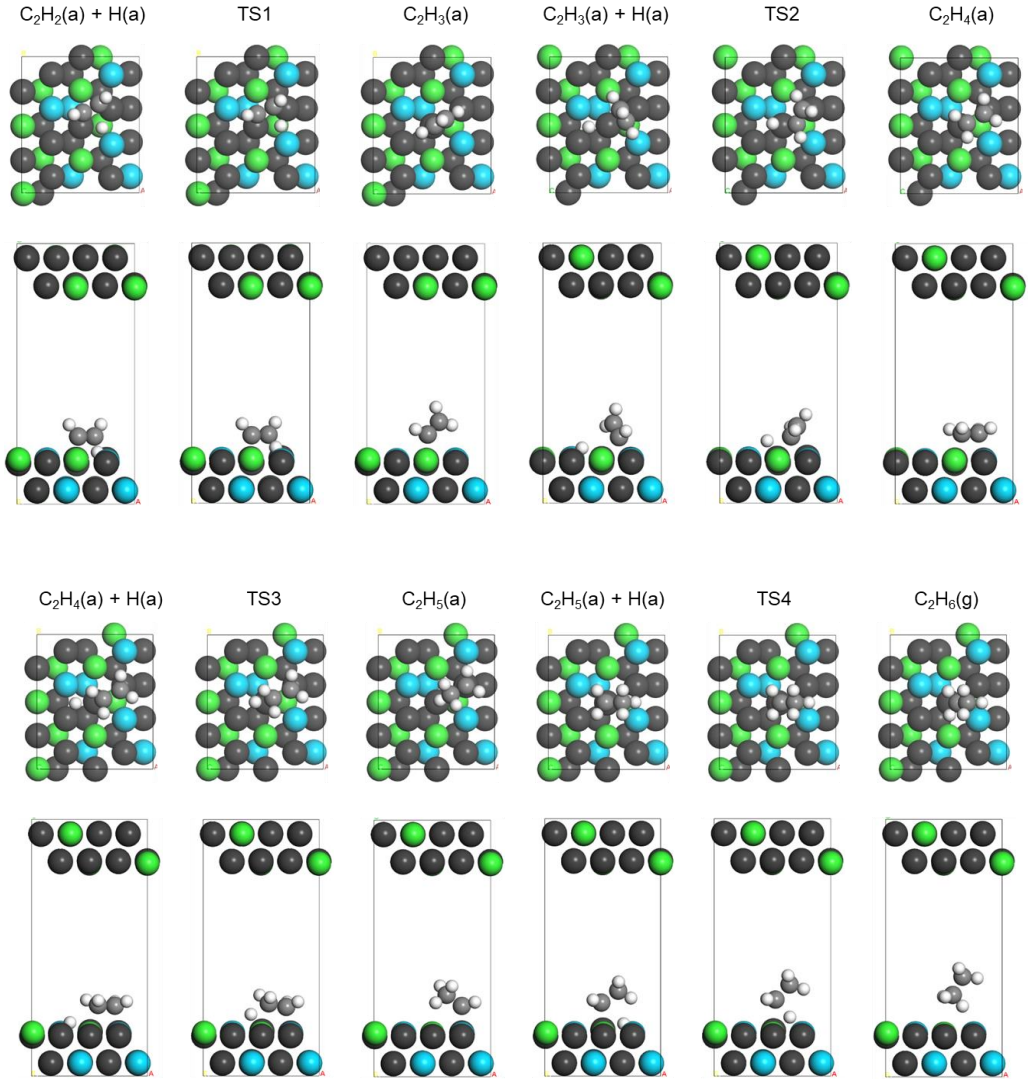

Figure 3.22. Optimized structures of the slab and adsorbates acetylene hydrogenation to ethane over $(Ni_{0.8}Cu_{0.2})_3Ga(111)$.

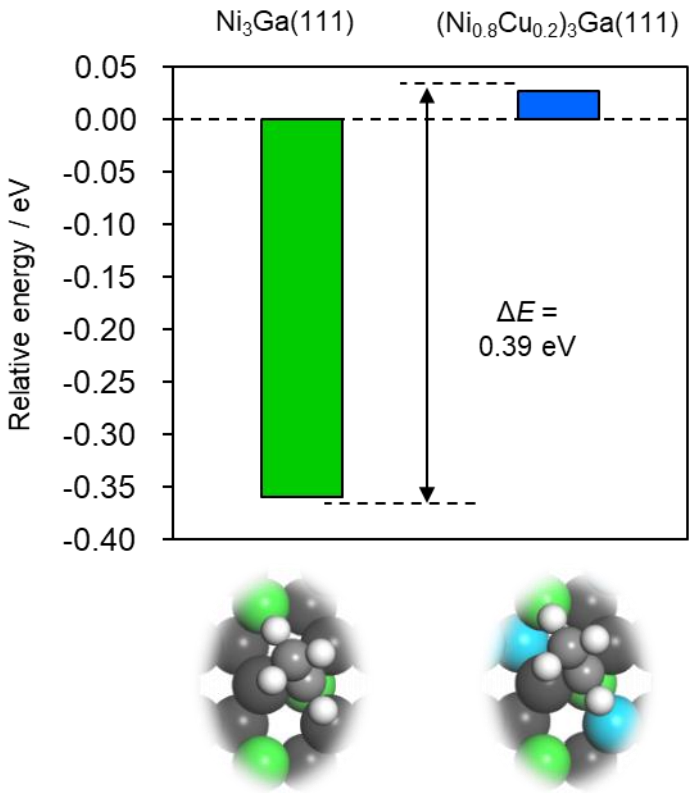

Figure 3.23. Relative energy of ethylidene intermediate on Ni_3Ga (111) and $(Ni_{0.8}Cu_{0.2})_3Ga$(111). Sum of gas phase C_2H_6 and the clean slab was set to zero in energy as in Figure 3.20a.

3.4 Discussion

In summary, we successfully applied a catalyst design concept based on a pseudo-binary alloy for the fine-tuning of the active property and resulting catalytic performance in acetylene semi-hydrogenation. A part of the Ni sites in intermetallic Ni_3Ga was substituted with Cu to form a series of $(Ni_{1-x}Cu_x)_3Ga$ catalysts with various Cu contents (x = 0.2, 0.25, 0.33, 0.5, 0.6, and 0.75). The optimal catalyst, $(Ni_{0.8}Cu_{0.2})_3Ga/TiO_2$, exhibited outstandingly high catalytic activity among reported 3d transition metal-based systems (1250 $mL_{C_2H_2}{}^{-1}min^{-1}g^{-1}$), excellent ethylene selectivity (96%), and long-term stability (100 h) with near full conversion even at 150°C. The appropriate amount of Cu doping formed Ni_2Cu hollow sites on the stable Ni_3Ga (111) surface, which significantly destabilized the multifold coordination of adsorbates, such as 3-fold vinyl, thereby lowering the energy barrier of acetylene hydrogenation. This destabilization also weakened the strong adsorption of acetylene, which (1) further accelerated

the hydrogenation process by increasing hydrogen coverage and (2) improved ethylene selectivity by suppressing the direct hydrogenation pathway via the ethylidene intermediate. Owing to the combination of these enhancements, acetylene semi-hydrogenation at low temperatures can be performed using Ni-based materials. Thus, the wide tunability and expandability of this catalyst design concept are highly versatile for constructing innovative catalysts. The findings in this study provide a highly efficient catalytic system to produce polymer-grade ethylene and uncover a new field of catalyst design based on multinary alloys.

References

[1] J. K. N. Felix Studt, Frank Abild-Pedersen, Thomas Bligaard, Rasmus Z. Sørensen, Claus H. Christensen, *Science* **2008**, 1320.

[2] J. Osswald, R. Giedigkeit, R. E. Jentoft, M. Armbrüster, F. Girgsdies, K. Kovnir, T. Ressler, Y. Grin, R. Schlögl, *Journal of Catalysis* **2008**, *258*, 210.

[3] B. Lou, H. Kang, W. Yuan, L. Ma, W. Huang, Y. Wang, Z. Jiang, Y. Du, S. Zou, J. Fan, *ACS Catalysis* **2021**, *11*, 6073.

[4] Y. Liu, X. Liu, Q. Feng, D. He, L. Zhang, C. Lian, R. Shen, G. Zhao, Y. Ji, D. Wang, G. Zhou, Y. Li, *Advanced Materials* **2016**, *28*, 4747.

[5] Y. Chen, J. Chen, *Applied Surface Science* **2016**, *387*, 16.

[6] Segall, M. D. *et al.* First-principles simulation: Ideas, illustrations and the CASTEP code. *J. Phys. Condens. Matter* **14**, 2717–2744 (2002).

[7] Hammer, B., Hansen, L. B. & Nørskov, J. K. Improved adsorption energetics within density-functional theory using revised Perdew-Burke-Ernzerhof functionals. *Phys. Rev. B - Condens. Matter Mater. Phys.* **59**, 7413–7421 (1999).

[8] Tkatchenko, A. & Scheffler, M. Accurate molecular van der Waals interactions from ground-state electron density and free-atom reference data. *Phys. Rev. Lett.* **102**, 6–9 (2009).

[9] Hu, K. *et al.* Boosting electrochemical water splitting: via ternary NiMoCo hybrid nanowire arrays. *J. Mater. Chem. A* **7**, 2156–2164 (2019).

[10] Govind, N., Petersen, M., Fitzgerald, G., King-Smith, D. & Andzelm, J. A generalized synchronous transit method for transition state location. *Comput. Mater. Sci.* **28**, 250–258 (2003).

[11] Halgren, T. A. & Lipscomb, W. N. The synchronous-transit method for determining reaction pathways and locating molecular transition states. *Chem. Phys. Lett.* **49**, 225–232 (1977).

[12] Ge, X. *et al.* Enhanced acetylene semi-hydrogenation on a subsurface carbon tailored Ni-Ga intermetallic catalyst. *J. Mater. Chem. A* 19722–19731 (2022).

[13] Fu, B. *et al.* Highly Selective and Stable Isolated Non-Noble Metal Atom Catalysts for Selective Hydrogenation of Acetylene. *ACS Catal.* **12**, 607–615 (2022).

[14] Liu, Y. *et al.* Layered double hydroxide-derived Ni-Cu nanoalloy catalysts for semi-hydrogenation of alkynes: Improvement of selectivity and anti-coking ability via alloying of Ni and Cu. *J. Catal.* **359**, 251–260 (2018).

[15] Lu, C., Zeng, A., Wang, Y. & Wang, A. Copper-Based Catalysts for Selective Hydrogenation of Acetylene Derived from $Cu(OH)_2$. *ACS Omega* **6**, 3363–3371 (2021).

[16] Lu, C., Wang, Y., Zhang, R., Wang, B. & Wang, A. Preparation of an Unsupported Copper-Based Catalyst for Selective Hydrogenation of Acetylene from Cu_2O Nanocubes. *ACS Appl. Mater. Interfaces* **12**, 46027–46036 (2020).

[17] Wang, Y., Liu, B., Lan, X. & Wang, T. Subsurface Carbon as a Selectivity Promotor to Enhance Catalytic Performance in Acetylene Semi-hydrogenation. *ACS Catal.* **11**, 10257–10266 (2021).

[18] Liu, H. *et al.* Effect of IB-metal on Ni/SiO_2 catalyst for selective hydrogenation of acetylene. *Chinese J. Catal.* **41**, 1099–1108 (2020).

[19] Zhou, H. *et al.* Sulfur-Doped g-C_3N_4-Supported Ni Species with a Wide Temperature Window for Acetylene Semi-hydrogenation. *ACS Sustain. Chem. Eng.* **10**, 4849–4861 (2022).

[20] Cao, Y. *et al.* Adsorption Site Regulation to Guide Atomic Design of Ni–Ga Catalysts for Acetylene Semi-Hydrogenation. *Angew. Chemie* **132**, 11744–11749 (2020).

[21] Shi, X. *et al.* Copper Catalysts in Semi-hydrogenation of Acetylene: From Single Atoms to Nanoparticles. *ACS Catal.* **10**, 3495–3504 (2020).

[22] Chai, Y. *et al.* Acetylene-Selective Hydrogenation Catalyzed by Cationic Nickel Confined in Zeolite. *J. Am. Chem. Soc.* **141**, 9920–9927 (2019).

[23] Gu, J. *et al.* Synergizing metal–support interactions and spatial confinement boosts dynamics of atomic nickel for hydrogenations. *Nat. Nanotechnol.* **16**, 1141–1149 (2021).

[24] Huang, F. *et al.* Anchoring Cu_1 species over nanodiamond-graphene for semi-hydrogenation of acetylene. *Nat. Commun.* **10**, 4431 (2019).

[25] Riley, C. *et al.* Synthesis of Nickel-Doped Ceria Catalysts for Selective Acetylene Hydrogenation. *ChemCatChem* **11**, 1526–1533 (2019).

[26] Chen, Y. & Chen, J. Selective hydrogenation of acetylene on SiO_2 supported Ni-In bimetallic catalysts: Promotional effect of In. *Appl. Surf. Sci.* **387**, 16–27 (2016).

[27] Armbrüster, M. *et al.* Al13 Fe4 as a low-cost alternative for palladium in heterogeneous hydrogenation. *Nat. Mater.* **11**, 690–693 (2012).

[28] Dai, X. *et al.* Single Ni sites distributed on N-doped carbon for selective hydrogenation of acetylene. *Chem. Commun.* **53**, 11568–11571 (2017).

[29] Kojima, T., Kameoka, S., Fujii, S., Ueda, S. & Tsai, A. P. Catalysis-tunable Heusler alloys in selective hydrogenation of alkynes: A new potential for old materials. *Sci. Adv.* **4**, (2018)

[30] Ge, X. *et al.* Enhanced acetylene semi-hydrogenation on a subsurface carbon tailored Ni-Ga intermetallic catalyst. *J. Mater. Chem. A* 19722–19731 (2022).

[31] Fu, B. *et al.* Highly Selective and Stable Isolated Non-Noble Metal Atom Catalysts for Selective Hydrogenation of Acetylene. *ACS Catal.* **12**, 607–615 (2022).

[32] Liu, Y. *et al.* Layered double hydroxide-derived Ni-Cu nanoalloy catalysts for semi-hydrogenation of alkynes: Improvement of selectivity and anti-coking ability via alloying of Ni and Cu. *J. Catal.* **359**, 251–260 (2018).

[33] Lu, C., Zeng, A., Wang, Y. & Wang, A. Copper-Based Catalysts for Selective Hydrogenation of Acetylene Derived from $Cu(OH)_2$. *ACS Omega* **6**, 3363–3371 (2021).

[34] Lu, C., Wang, Y., Zhang, R., Wang, B. & Wang, A. Preparation of an Unsupported Copper-Based Catalyst for Selective Hydrogenation of Acetylene from Cu_2O Nanocubes. *ACS Appl. Mater. Interfaces* **12**, 46027–46036 (2020).

[35] Wang, Y., Liu, B., Lan, X. & Wang, T. Subsurface Carbon as a Selectivity Promotor to Enhance Catalytic Performance in Acetylene Semi-hydrogenation. *ACS Catal.* **11**, 10257–10266 (2021).

[36] Liu, H. *et al.* Effect of IB-metal on Ni/SiO_2 catalyst for selective hydrogenation of acetylene. *Chinese J. Catal.* **41**, 1099–1108 (2020).

[37] Zhou, H. *et al.* Sulfur-Doped g-C_3N_4-Supported Ni Species with a Wide Temperature Window for Acetylene Semi-hydrogenation. *ACS Sustain. Chem. Eng.* **10**, 4849–4861 (2022).

[38] Cao, Y. *et al.* Adsorption Site Regulation to Guide Atomic Design of Ni–Ga Catalysts for Acetylene Semi-Hydrogenation. *Angew. Chemie* **132**, 11744–11749 (2020).

[39] Shi, X. *et al.* Copper Catalysts in Semi-hydrogenation of Acetylene: From Single Atoms to Nanoparticles. *ACS Catal.* **10**, 3495–3504 (2020).

[40] Chai, Y. *et al.* Acetylene-Selective Hydrogenation Catalyzed by Cationic Nickel Confined in Zeolite. *J. Am. Chem. Soc.* **141**, 9920–9927 (2019).

[41] Gu, J. *et al.* Synergizing metal–support interactions and spatial confinement boosts dynamics of atomic nickel for hydrogenations. *Nat. Nanotechnol.* **16**, 1141–1149 (2021).

[42] Huang, F. *et al.* Anchoring Cu_1 species over nanodiamond-graphene for semi-hydrogenation of acetylene. *Nat. Commun.* **10**, 4431 (2019).

[43] Riley, C. *et al.* Synthesis of Nickel-Doped Ceria Catalysts for Selective Acetylene Hydrogenation. *ChemCatChem* **11**, 1526–1533 (2019).

[44] Chen, Y. & Chen, J. Selective hydrogenation of acetylene on SiO_2 supported Ni-In bimetallic catalysts: Promotional effect of In. *Appl. Surf. Sci.* **387**, 16–27 (2016).

[45] Armbrüster, M. *et al.* $Al_{13}Fe_4$ as a low-cost alternative for palladium in heterogeneous hydrogenation. *Nat. Mater.* **11**, 690–693 (2012).

[46] Dai, X. *et al.* Single Ni sites distributed on N-doped carbon for selective hydrogenation of acetylene. *Chem. Commun.* **53**, 11568–11571 (2017).

[47] Kojima, T., Kameoka, S., Fujii, S., Ueda, S. & Tsai, A. P. Catalysis-tunable Heusler alloys in selective hydrogenation of alkynes: A new potential for old materials. *Sci. Adv.* **4**, (2018).

[48] Ma, J., Xing, F., Nakaya, Y., Shimizu, K. ichi & Furukawa, S. Nickel-Based High-Entropy Intermetallic as a Highly Active and Selective Catalyst for Acetylene Semi-hydrogenation. *Angew. Chemie - Int. Ed.* **61**, (2022).

[49] Li, Z. *et al.* Unveiling the origin of enhanced catalytic performance of NiCu alloy for semi-hydrogenation of acetylene. *Chem. Eng. J.* **450**, 138244 (2022).

[50] Liu, Y. *et al.* Intermetallic NixMy(M = Ga and Sn) Nanocrystals: A Non-precious Metal Catalyst for Semi-Hydrogenation of Alkynes. *Adv. Mater.* **28**, 4747–4754 (2016).

[51] Zhao, J. *et al.* Preparation of MCM-41 supported nickel NPs for the high-efficiency semi-hydrogenation of acetylene. *New J. Chem.* **45**, 1054–1062 (2021).

[52] Komatsu, T., Kishi, T. & Gorai, T. Preparation and catalytic properties of uniform particles of Ni_3Ge intermetallic compound formed inside the mesopores of MCM-41. *J. Catal.* **259**, 174–182 (2008).

[53] Bridier, B. & Pérez-Ramírez, J. Coperative effects in ternary Cu-Ni-Fe catalysts lead to enhanced alkene selectivity in alkyne hydrogenation. *J. Am. Chem. Soc.* **132**, 4321–4327 (2010).

[54] Fu, F. *et al.* Interfacial Bifunctional Effect Promoted Non-Noble Cu/Fe_yMgO_x Catalysts for Selective Hydrogenation of Acetylene. *ACS Catal.* **11**, 11117–11128 (2021).

[55] Ge, X. *et al.* Mechanism driven design of trimer Ni_1Sb_2 site delivering superior hydrogenation selectivity to ethylene. *Nat. Commun.* **13**, 5534 (2022).

[56] Zhou, S., Kang, L., Zhou, X., Xu, Z. & Zhu, M. Pure acetylene semi-hydrogenation over Ni–Cu bimetallic catalysts: Effect of the Cu/Ni ratio on catalytic performance. *Nanomaterials* **10**, 509 (2020).

[57] Nakaya, Y. & Furukawa, S. Catalysis of Alloys: Classification, Principles, and Design for a Variety of Materials and Reactions. *Chem. Rev.* (2022).

Chapter Four

Silica–-decorated Ni-Zn alloy as a highly active and selective catalyst for acetylene semi-hydrogenation

4.1 Introduction

Precious metals, such as Pd and Pt, are highly active catalysts for hydrogenation and dehydrogenation. However, their high cost hampers the widespread application of large-scale chemical processes. Thus, it is essential to develop efficient catalytic systems based on cheap and earth-abundant elements.[1–8] Although Ni-based catalysts have been regarded as promising noble metal alternatives because of their much lower cost, the catalytic activity is unsatisfactory compared with those of Pt- and Pd-based materials.[9] Therefore, developing highly active Ni-based catalysts for (de)hydrogenation reactions is attractive in the field of pure and applied chemistry.

Chemical modification of Ni-based alloy has been a possible methodology for this purpose. For instance, the base-extraction of Al from Ni–Al alloy is a well-known method to afford porous and active Ni catalysts (Raney®-Ni) for hydrogenation reactions. Recently, Abe et al. reported that "Ni-based rooted catalyst" was obtained from Ni_3Y alloy by reaction with CO and O_2, which was stable for dry reforming of methane.[10]

We reported another efficient method, i.e., surface dealloying of Ni–Si intermetallics. The surface of Ni–Si intermetallics was transformed into a unique structure, where small Ni clusters (2–3 nm) were embedded in the SiO_2 matrix. This material was more active than monometallic Pd in benzene hydrogenation.[11] Recently, we extended these interesting Ni structures from the bulk material to supported system using additional silica decoration to conventional Ni nanoparticles on SiO_2 support. The silica-decoration changed the morphology of Ni nanoparticles from spherical to rough and anisotropic, where the number of step sites significantly increased (Figure 4.1, left) and the catalytic activities in alkane (de)hydrogenation and aromatic hydrogenation were enhanced.[12]

Next, we focused on developing a highly active and "selective" catalyst for semi-hydrogenation of alkynes. Activity and selectivity are in a tradeoff relationship for selective hydrogenation because higher activity tends to induce undesired over hydrogenation. Thus, achieving high activity and selectivity has been regarded as a challenging task in catalytic chemistry. As a model reaction, we focused on acetylene semi-hydrogenation since it is an industrially important process for purifying crude ethylene with trace acetylene for ethylene

polymerization;[13–15] it is also of interest to researchers on fundamental surface chemistry.[16–18] Ni–Zn alloy is a highly selective catalyst for acetylene semi-hydrogenation into ethylene because of the lowered d-band center, which promotes ethylene desorption.[19, 20] However, the catalytic activity of Ni–Zn alloy was much lower than precious-metal based catalysts such as Pd–Zn.[21, 22] In this study, we attempted to improve the catalytic activity of Ni–Zn alloy in acetylene semi-hydrogenation without lowering its selectivity using the silica-decoration method (Figure 4.1, right). We report a highly active and selective Ni-based catalyst for acetylene semi-hydrogenation and the synergy of alloying and the silica decoration effects on catalysis.

The catalyst preparation was simple; Ni–Zn alloy nanoparticles on silica support (Ni–Zn/SiO_2, Ni: 2 wt.%, Ni/Zn = 1) were prepared by a pore-filling co-impregnation method using a mixed aqueous solution of Ni and Zn nitrates, followed by drying (80°C), calcination (500°C), and reduction (500°C). Silica decorated Ni–Zn (Si–Ni–Zn/SiO_2, Ni/Si = 4) was prepared in a similar manner using thus-prepared Ni–Zn/SiO_2 and an ethanol solution of triphenylsilanol, $(C_6H_5)_3SiOH$ (see Supporting Information for details). Organic silanol is transformed into silica during the calcination process.

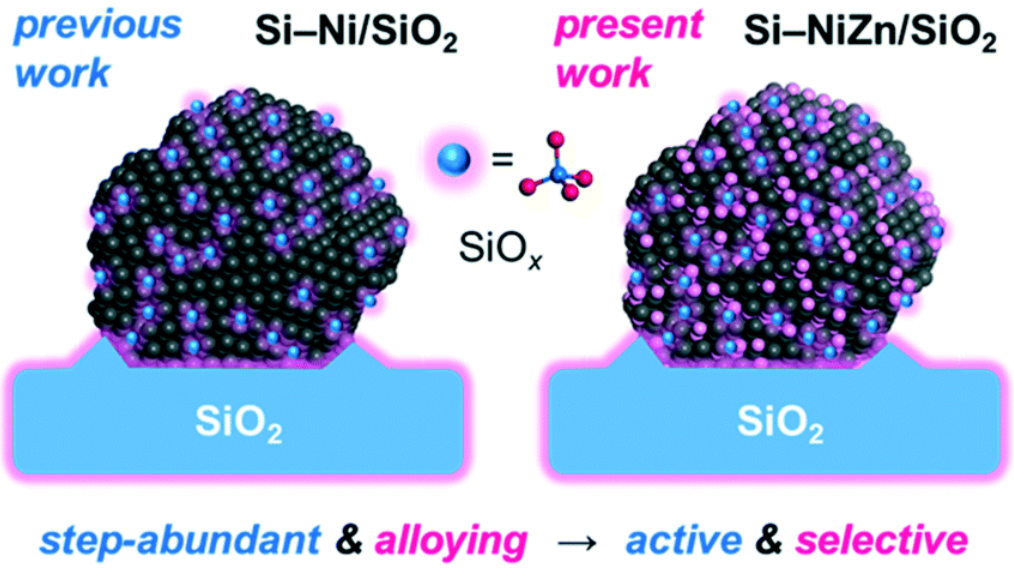

Figure 4.1. Catalyst design concepts in the previous (Si–Ni/SiO_2) and current studies (Si–Ni–Zn/SiO_2). The silica-decoration to Ni nanoparticles on SiO_2 makes the morphology rough and

anisotropic, where a substantial number of step sites are present. Gray: Ni, magenta: Zn, cyan: silica.

4.2 Experiment section

4.2.1 Catalysts preparation

Ni and Ni–Zn alloy nanoparticles supported on silica (Ni/SiO_2 and $Ni–Zn/SiO_2$, Ni loading: 2 wt%) were prepared by pore-filling impregnation method. Aqueous solution of Ni $(NO_3)_3 \cdot 6H_2O$ (Wako, 99%) alone or Ni $(NO_3)_3 \cdot 6H_2O$ and Zn $(NO_3)_2 \cdot 6H_2O$ (Wako, 99%) with molar ratio 1:1 was added to dried silica gel (CARiACT G-6, Fuji Silysia, S_{BET} = 470 m^2g^{-1}) so that the solutions filled the silica pores. The mixtures were sealed overnight at room temperature and dried over liquid nitrogen under vacuum overnight followed by drying at 90℃. The reduction under flowing H_2 at 600 ℃ for 1 h was then performed. Silica decorated Ni (Si–Ni/SiO_2) and Ni–Zn nanoparticles supported on silica (Si–Ni–Zn/SiO_2) were prepared by adding ethanol solution of $C_{18}H_{16}OSi$ (Mr = 276.40 g mol−1, Tokyo Chemical Industry Co., Ltd) and Ni $(NO_3)_3 \cdot 6H_2O$ (Wako, 99%) with Zn $(NO_3)_2 \cdot 6H_2O$ (Wako, 99%) in a similar fashion to that of Ni/SiO_2 or $Ni–Zn/SiO_2$ except drying over the hot plate. The specific surface area of the prepared catalysts was as follows: $Ni–Zn/SiO_2$, S_{BET} = 454 m^2g^{-1}; $Si–Ni–Zn/SiO_2$**,** S_{BET} = 451 m^2g^{-1}, indicating that the silica-decoration did not decrease the surface area.

4.2.2 Catalytic Reaction

The catalytic activities of the prepared catalysts were tested in hydrogenation of acetylene. The mixture of Ni-based catalysts (15 mg) and quartz sand (Miyazaki Chemical Co., 250 ~ 420 μm, 2 g) was filled into a quartz glass tube (internal diameter, 10 mm) and put in a fixed bed continuous reactor. Prior to the activity test, the catalyst was reduced under flowing H_2 (10 mL min^{-1}) at 500℃ for 0.5 h and the temperature was cooled down to the reaction temperature. The reaction was initiated by flowing the gas mixture: (C_2H_2:H_2:He = 2:20:10 mL min−1: GHSV = 128,000 mL h^{-1} g^{-1}). The gas phase was analyzed by an online thermal conductivity detector (TCD) gas chromatography (Shimadzu GC-8A) equipped downstream connected to the Unipack S packed column. The catalytic performance (C_2H_2 conversion and C_2H_4

selectivity) at 15 min on stream was reported. For the stability test, 60 mg of catalyst was used. C_2H_2 conversion and C_2H_4 selectivity were calculated using the following equations:

C_2H_2 conversion (%) = ($F_{C2H2,in} - F_{C2H2,out}$) / $F_{C2H2,in}$ × 100

C_2H_4 selectivity (%) = $F_{C2H4,out}$ / ($F_{C2H2,in} - F_{C2H2,out}$) × 100

4.2.3 Characterization

The crystal structure of the prepared catalyst was examined by powder X-ray diffraction (XRD) using a Rigaku MiniFlex II/AP diffractometer with Cu Kα radiation.

High-angle annular dark field scanning transmission electron microscopy (HAADF-STEM) was carried out using a JEOL JEM-ARM200 M microscope equipped with an energy dispersive X-ray (EDX) analyzer (EX24221M1G5T). STEM analysis was performed at an accelerating voltage of 200 kV. To prepare the TEM specimen, all samples were sonicated in ethanol and then dispersed on a Mo grid supported by an ultrathin carbon film.

Reduction properties of the as-prepared catalyst were analyzed by temperature programmed reduction method by H_2 (H_2-TPR) by using a BELCAT-II instrument. Prior to analysis, 30 mg of catalyst was pretreated at 150°C for 1 h under inert He flow to remove absorbed water, then the sample was heated under H_2 flow (5v% H_2 balanced with Ar 30 sccm) in the temperature from 50°C to 900°C at a ramping rate of 2°C/min^{-1}.

4.2.4 Computational details

Periodic density functional theory (DFT) calculations, except frequency calculations, were performed using the CASTEP code[23] with Vanderbilt-type ultrasoft pseudopotentials[24] and a revised Perdew–Burke–Ernzerhof exchange-correlation functional (RPBE)[25] based on the generalized gradient approximation (GGA). The plane-wave basis set was truncated at a kinetic energy of 370 eV. A Fermi smearing of 0.1 eV was utilized. The reciprocal space was sampled using a *k*-point mesh with a typical spacing of 0.04 Å^{-1} generated by the Monkhorst–Pack scheme.[26] Geometry optimizations were performed in supercell structures using periodic boundary conditions. Surfaces were modeled using 4 atomic layer-thick metallic slabs. An L12-type Ni_3Zn structure was considered as the model of the $Ni_{0.75}Zn_{0.25}$ alloy. The surface

was modeled using $Ni_3Zn(111)$ and $Ni_3Zn(211)$ planes for the terrace and step sites of Ni–Zn, respectively, with a 13 Å vacuum region. Convergence criteria comprised a) a self-consistent field (SCF) tolerance of 1.0×10^{-6} eV/atom, b) an energy tolerance of 1.0×10^{-5} eV/atom, c) a maximum force tolerance of 0.05 eV $Å^{-1}$, and d) a maximum displacement tolerance of 1.0×10^{-3} Å for structure optimization and energy calculation. Frequency calculations of adsorbed CO molecules were conducted by the DMol[25] code[27] based on the aforementioned optimized structures. These calculations involved the RPBE functional, a double-numeric quality basis set with polarization functions (DNP, comparable to Gaussian 6-311G**) [28] with a real-space cutoff of 4.2 Å, DFT semi-core pseudopotential core treatment, [29] and a Fermi smearing of 0.1 eV. The SCF convergence was accelerated using the iterative scheme proposed by Kresse and Furthmüller.[30] The partial Hessian matrix including C and O atoms was computed to evaluate the harmonic frequencies for adsorbed CO. All computed harmonic frequencies were scaled by an empirical factor of 1.056, which corresponds to the ratio of experimental [31] and computed values for gas-phase CO (2143 cm^{-1}/2028.7 cm^{-1}).

4.3 Results

4.3.1 Structure characterization of the catalysts

The X-ray diffraction (XRD) patterns of Ni–Zn/SiO_2 and Si–Ni– Zn/SiO_2 (Figure. 4.1) showed that the 3:1 Ni–Zn solid-solution alloy phase was formed for both catalysts. The crystallite size estimated from Scherrer's equation was about 3 nm in each case. This result showed that the silica-decoration did not change the size and degree of alloying of Ni–Zn nanoparticles. Then, we conducted high angle annular dark field scanning transmission electron microscopy–energy dispersive X-ray spectroscopy (HAADF-STEM-EDX) analysis for Si–Ni–Zn/SiO_2 catalyst. The particle size ranged from 2 to 6 nm, and the volume-weighted average was 3.9 nm (Figures. 4.2a–4.2c), which is consistent with the crystallite size estimated by XRD. The high resolution HAADF-STEM image of a single nanoparticle showed the atomic arrangement of an fcc crystal viewed along the [001] direction (Figure 4.2d). The elemental map indicates that the

nanoparticles consist of Ni and Zn (Figures 4.2e and 4.2f). Based on these results, it can be concluded that the 3:1 solid-solution alloy of Ni–Zn was formed as small nanoparticles on SiO_2.

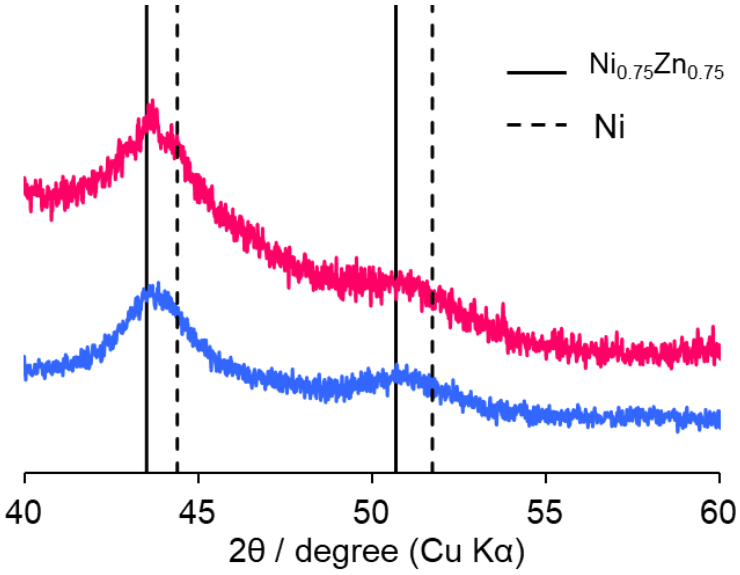

Figure 4.1. XRD patterns of Ni–Zn/SiO_2 and Si–Ni–Zn/SiO_2. References are shown as black vertical lines.

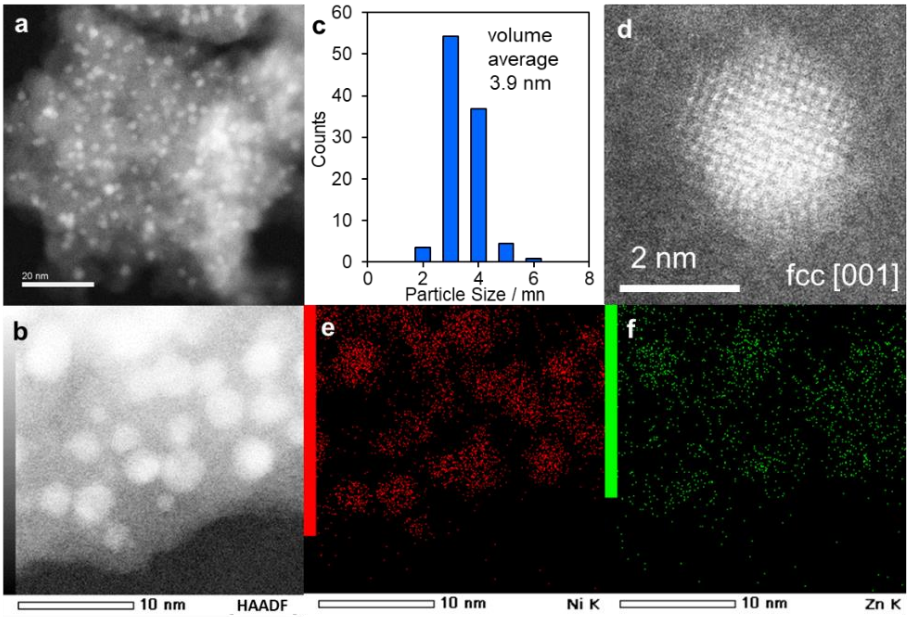

Figure 4.2. HAADF-STEM-EDX of Si–Ni–Zn on SiO_2 support. (a) and (b) HAADF-STEM image of Si–Ni–Zn/SiO_2 (Ni:Zn = 1:1) (c) size distribution of the nanoparticle (d) high resolution of HAADF-STEM and elemental maps of (e) Ni and (f) Zn acquired using EDX.

4.3.2 Mechanistic study

The temperature-programmed reduction by H_2 (H_2-TPR) was conducted for Ni–Zn/SiO_2 and Si–Ni–Zn/SiO_2 to compare the reducibility of each catalyst (Figure 4.3). For undecorated Ni–Zn, intense reduction peaks appeared at 246°C and 316°C, which is attributed to the reduction of Ni and Zn, respectively. [32-33] The reduction peaks appearing at more than 500°C may be assigned to Zn oxide species strongly bound on SiO_2. The appearance of this reduction indicates that not all the Zn species were reduced at 500°C (temperature for catalyst preparation and pretreatment) and the presence of Zn oxide on the catalyst. It is consistent with the 3:1 alloy phase formed even though the Ni/Zn fed ratio was 1. For Si–Ni–Zn, these reduction peaks shifted to higher temperatures (246°C→262°C, 306°C; 316°C→406°C; 541°C→763°C). It indicates that the reduction of Ni and Zn is inhibited by the additional silica species, and that there is some chemical interaction between metals (Ni and Zn) and additional silica species. This result also suggests that the Ni–Zn alloy nanoparticles have close contact with the additional silica species. Then, we performed Fourier-transform infrared (FT-IR) analysis with CO adsorption at −196°C to characterize the surface structure. As shown in Figure 4.4, Ni–Zn/SiO_2 and Si–Ni–Zn/SiO_2 showed adsorption bands at 2065 cm^{-1} and 2018 cm^{-1}, respectively, both of which are assignable to CO linearlyadsorbed on Ni alloyed with Zn.[34] We recently reported a similar deviation in the peak position of linear CO upon silica decoration for monometallic Ni/SiO_2, where a DFT calculation indicated that the band at lower wavenumber can be assignable to CO adsorbed on the step Ni site.11 Likewise, in this study, we calculated the theoretical vibrational frequency of adsorbed CO on Ni_3Zn(111) and Ni_3Zn(211) (see computational details).

The calculated frequency of linear CO on the step Ni sites was 2044 cm^{-1}, which was redshifted by 45 cm^{-1} to that on the terrace site (2089 cm^{-1}). Thus, the DFT calculation well reproduced the experimental redshift of 47 cm^{-1} and supports that step Ni sites are mainly present on the surface of Si–Ni–Zn/SiO_2. Ni–Zn/SiO_2 did not show bridge CO as reported in literature, which is due to the ensemble effect by Zn. In contrast, bridge CO was observed at 1892 cm−1 on Si–Ni–Zn/SiO_2. The DFT calculation for the bridge CO at the step Ni site

well reproduced the experimental value (1888 cm^{-1}), suggesting that the bridge adsorption mode is allowed for the step site even on Ni–Zn alloy surface.

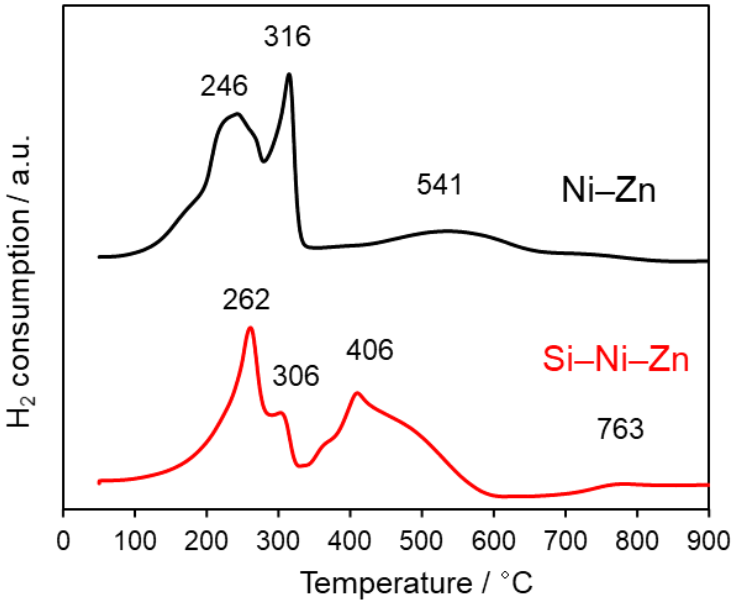

Figure 4.3. H_2-TPR profiles of Ni–Zn/SiO_2 and Si–Ni–Zn/SiO_2.

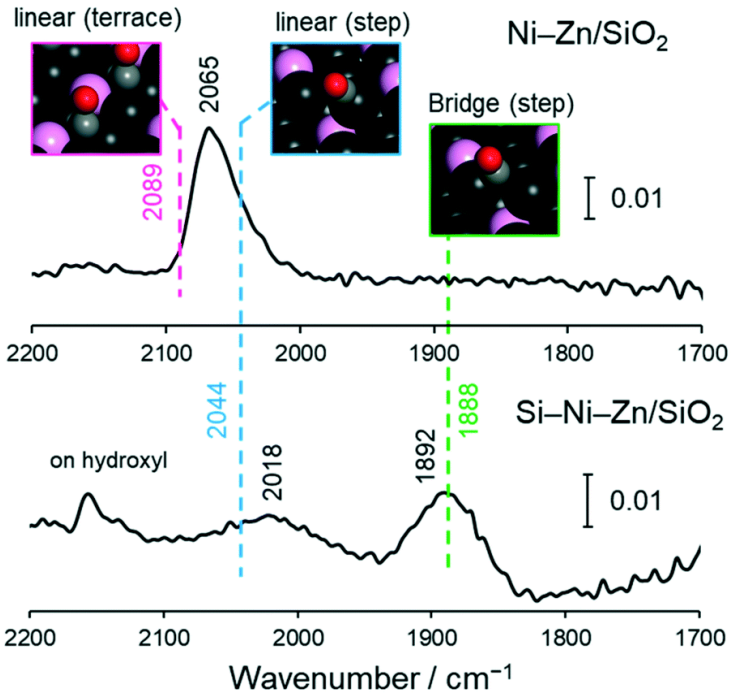

Figure 4.4. FT-IR spectra of CO adsorbed on Ni–Zn/SiO_2 and Si–Ni–Zn/SiO_2 measured at −196°C. Inset figures indicate the optimized structure of linear and bridge CO on the terrace site of Ni_3Zn(111) and the step site of Ni_3Zn(111) calculated by DFT. The corresponding theoretical frequencies of CO stretching vibration were indicated as vertical dashed lines and colored values.

4.3.3 Catalytic performance

Finally, we tested the catalytic performances of the prepared Ni-based catalysts in acetylene semi-hydrogenation. Figure 4.5 shows acetylene conversion and ethylene selectivity for the tested catalysts. For better comparison, control experiments using monometallic Ni with and without silica-decoration (Ni/SiO_2 and Si–Ni/SiO_2) were also conducted. Conventional Ni/SiO_2 showed good selectivity at a low conversion level. The silica-decoration to monometallic Ni significantly improved the acetylene conversion from 37% to 100% (130°C). However, no ethylene was obtained due to excess over hydrogenation to ethane, which is widely known for monometallic Ni. Thus, the silica decoration methodology alone does not apply to selective hydrogenation systems. Ni–Zn/SiO_2 showed high ethylene selectivity as reported in the literature,[19] much higher temperature (200°C) was needed to obtain an acetylene conversion comparable to that for Ni/SiO_2. However, Si–Ni–Zn/SiO_2 exhibited much higher acetylene conversion (97%) and good ethylene selectivity (80%). Thus, the acetylene conversion was excellently improved without lowering ethylene selectivity.

We also confirmed that Si–Ni–Zn/SiO_2 showed much higher acetylene conversion than Ni–Zn/SiO_2 at various temperatures (150°C–200°C, Figure 4.6) and its catalytic performance was stable at least for 6 h (Figure 4.7). These results showed that the silica decoration method applies to alkyne hydrogenation and is compatible with the alloying effect on high selectivity. Figure 4.8 summarizes the catalytic performances of various Ni-based catalyst for acetylene semi-hydrogenation (see Table 4.1 for more details).

Si–Ni–Zn/SiO_2 exhibited twice higher specific activity (mL acetylene converted per min per gram Ni) than the highest ever reported, [35] which highlights the outstanding high catalytic activity and promotion effect of silica-decoration. In the previous study, we demonstrated that silica-decoration methodology was valid for alkane dehydrogenation and aromatic hydrogenation. We showed that this catalyst design concept might be valid for various catalytic systems. Besides, we obtained the Arrhenius-type plots for this reaction, where the apparent activation energy was almost similar with and without silica-decoration (Figure 4.9). It indicates that the hydrogenation ability (apparent activation energy and the resulting reaction rate) of one active site is not changed by silica-decoration. Thus, the enhanced catalytic activity

may be due to the increase in the number of active sites (probably, step sites) induced by silica-modification. Here, one may think that the silica decoration may decrease the number of active step sites. However, note that there is almost no active step site on unmodified Ni–Zn/SiO_2, whereas the step sites remain as active sites on Si–Ni–Zn/SiO_2, as evidenced by the FT-IR study. Therefore, the number of active step sites on Si–Ni–Zn/SiO_2 should be larger than that on Ni–Zn/SiO_2, which is the origin of the enhanced catalytic activity. What is important is that the step site cannot be present alone because it is unstable in the absence of the silica-decoration. Although some of the step sites are needed to be occupied with the additional silica for the stabilization of the step-abundant structure, there is no need to completely cover all the step sites. One may also think that why high selectivity was retained even with the significantly improved catalytic activity, because higher activity typically results in lower selectivity due to over hydrogenation. A possible interpretation might be the geometric effect of the step site on selectivity. Compared with C_2H_2, C_2H_4 molecule has larger steric hindrance. Besides, hydrogen diffusion is regulated at the step site. Therefore, hydrogen attack to C_2H_4 at the step site may be more geometrically suppressed compared with that to C_2H_2. Thus, the combination of the high activity and geometric restriction of the step site may enable the highly active and selective semi-hydrogenation of acetylene.

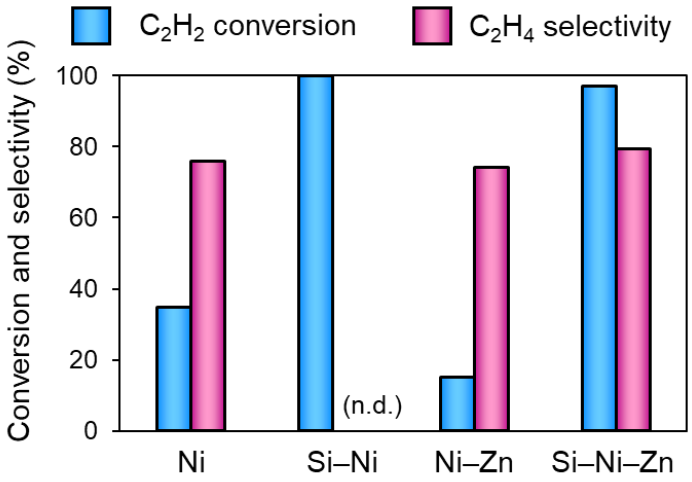

Figure 4.5. Catalytic performance of Ni-based catalysts in acetylene semi-hydrogenation (Ni loading: 2wt%, Ni:Si = 1:4, T = 130°C for Ni and Si–Ni, 200°C for Ni–Zn and Si–Ni–Zn.

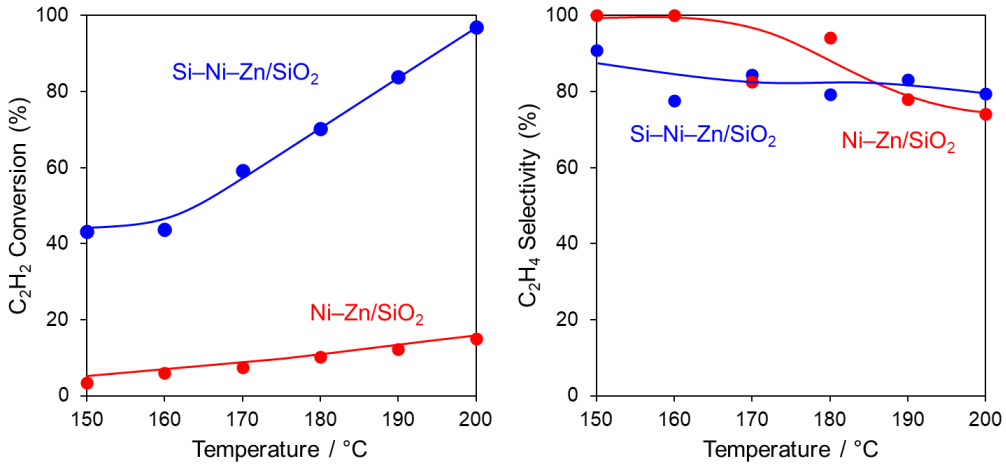

Figure 4.6. Temperature-dependences of C_2H_2 conversion and C_2H_4 selectivity for Ni–Zn/SiO_2 and Si–Ni–Zn/SiO_2 catalysts.

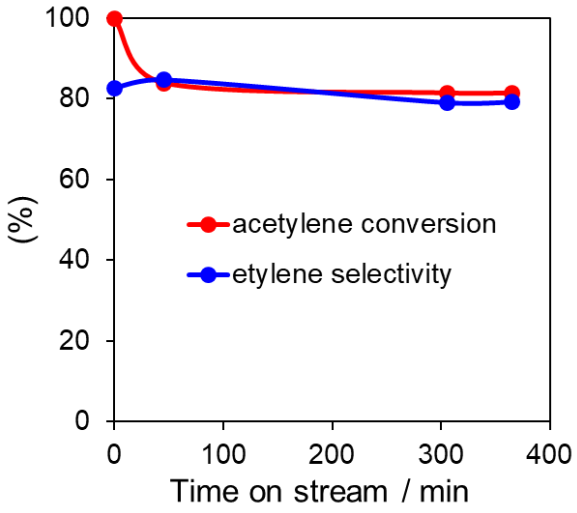

Figure 4.7. Stability test for acetylene semi-hydrogenation using Si–Ni–Zn/SiO_2.

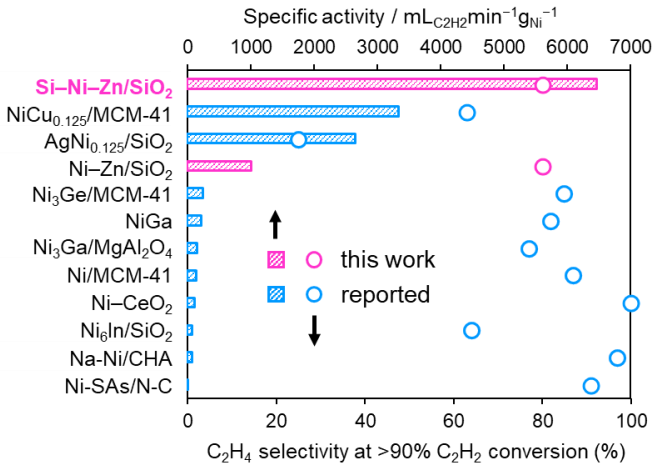

Figure 4.8. Summary of the catalytic performance of various Ni-based catalysts in acetylene semi-hydrogenation. For Ni_3Ge/MCM-41 and Ni–Zn/SiO_2, the specific activities at 30% and 15% conversions are shown, respectively.

Table S1. Summary of the catalytic performance of Ni-based catalyst in acetylene semihyderogenation.

entry	catalyst	Ni wt%	amount / mg	C_2H_2 flow /mLmin^{-1}	C_2H_2:H_2:C_2H_4:He(Ar) / mLmin^{-1}	GHSV / mLg^{-1}h^{-1}	conv. (%)	sel. (%)	temp. / °C	specific rate / mL$_{C2H2}$min^{-1}g$_{Ni}^{-1}$	ref
1	Si–Ni–Zn/SiO_2	2	15	2	2:20:0:10	128,000	97	80	200	6,467	this work
2	$NiCu_{0.125}$/MCM-41	1	100	3.3	3.3:10:0:0	8,000	100	63	250	3,333	[36]
3	$AgNi_{0.125}/SiO_2$	0.37	30	0.3	0.3:6:6:17.7	60,000	98	25	200	2,649	[37]
4	Ni–Zn/SiO_2	2	15	2	2:20:0:10	128,000	15	80	200	1,007	this work
5	Ni_3Ge/MCM-41	3	160	3.9	3.9:8.1:0:17	10,875	30	85	250	244	[38]
6	NiGa	10	50	1.2	1.2:12:24:82.5	144,000	90	82	190	216	[39]
7	$Ni_3Ga/MgAl_2O_4$	2	100	0.33	0.33:6.7:33.3:26.67	40,000	92	77	220	153	[40]
8	Ni/MCM-41	25	100	3.7	3.7:7.4:0:55.5	40,000	96	87	240	142	[41]
9	Ni–CeO_2	1.54	200	0.35	0.35:24.5:1.4:43.75	21,000	100	100	200	114	[42]
10	Ni_6In/SiO_2	8	500	3	3:30:0:267	36,000	100	64	200	75	[43]
11	Na-Ni/CHA	3.5	200	0.5	0.5:8:0:41.5	15,000	100	97	170	71	[44]
12	Ni-SAs/N-C	5.67 [a]	400	0.2	0.2:4:20:15.8	6,000	96	91	200	8	[45]

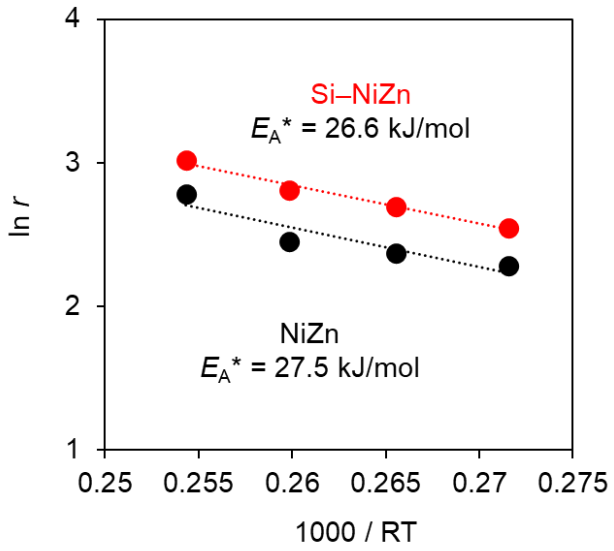

Figure 4.9. Arrhenius-type plots obtained in acetylene semi-hydrogenation on Ni–Zn/SiO_2 and Si–Ni–Zn/SiO_2.

4.4 Discussion

In summary, we applied the silica-decoration method to Ni–Zn alloy nanoparticles supported on silica. The silica-decoration significantly improved the catalytic activity of Ni–Zn alloy in acetylene semi-hydrogenation without lowering the ethylene selectivity. The catalyst design concept based on silicadecoration would apply to various catalytic systems to improve catalytic performance.

References

[1] S. A. Nikolaev, V. V. Smirnov, A. Y. Vasil'Kov, V. L. Podshibikhin, *Kinet. Catal.*, 2010, **51**, 375-379.

[2] M. Armbrüster, G. Wowsnick, M. Friedrich, M. Heggen, R. Cardoso-Gil, *J. Am. Chem. Soc.*, 2011, **133**, 9112-9118.

[3] X. Liu, Y. Li, J. W. Lee, C.-Y. Hong, C.-Y. Mou, B. W. L. Jang, *Appl. Catal. A*, 2012, **439**, 8-14.

[4] C. Ma, Y. Du, J. Feng, X. Cao, J. Yang, D. Li, *J. Catal.*, 2014, **317**, 263-271.

[5] Y. He, Y. Liu, P. Yang, Y. Du, J. Feng, X. Cao, J. Yang, D. Li, *J. Catal.*, 2015, **330**, 61-70.

[6] D. A. Lomeli-Rosales, M. D. Bernardos, S. Pèrez-Rodríguez, A. Gual, C. Claver, C. Godard, *Chem. Eur. J.*, 2019, **25**, 8321-8331.

[7] Y. Liu, J. Zhao, Y. He, J. Feng, T. Wu, D. Li, *J. Catal.*, 2017, **348**, 135-145.

[8] V. D. Stytsenko, D. P. Mel'nikov, O. P. Tkachenko, E. V. Savel'eva, A. P. Semenov, L. M. Kustov, *Russian Journal of Physical Chemistry A*, 2018, **92**, 862-869.

[9] B. Bridier, J. Perez-Ramirez. *J. Am. Chem. Soc.*, 2010, **132**, 4321-4327.

[10] S. Shoji, X. Peng, T. Imai, P. S. M. Kumar, K. Higuchi, Y. Yamamoto, T. Tokunaga, S. Arai, S. Ueda, A. Hashimoto, N. Tsubaki, M. Miyauchi, T. Fujita, H. Abe, *Chem. Sci.*, 2019, **10**, 3701-3705.

[11] W. F. Simanullang, H. Itahara, N. Takahashi, S. Kosaka, K. Shimizu, S. Furukawa, *Chem. Commun.*, 2019, **55**, 13999-14002.

[12] H. Ham. W.F. Simanullang, Y. Kanda, Y. Wen, A. Hashimoto, H. Abe, K. Shimizu,

[13] A. Borodziński, G. C. Bond, *Catal. Rev.: Sci. Eng.*, 2006, **48**, 91-144.

[14] M. Armbrüster, K. Kovnir, M. Friedrich, D. Teschner, G. Wowsnick, M. Hahne, P. Gille, L. Szentmiklósi, M. Feuerbacher, M. Heggen, F. Girgsdies, D. Rosenthal, R. Schlögl, Y. Grin, *Nat. Mater.*, 2012, **11**, 690-693.

[15] G. X. Pei, X. Y. Liu, A. Wang, A. F. Lee, M. A. Isaacs, L. Li, X. Pan, X. Yang, X. Wang, Z. Tai, K. Wilson, T. Zhang, *ACS Catal.*, 2015, **5**, 3717-3725.

[16] C. Burda, X. Chen, R. Narayanan, M. A. El-Sayed, *Chem. Rev*., 2005, **105**, 1025-1102.

[17] A. P. Alivisatos, *ACS Nano*, 2008, **2**, 1514-1516.

[18] C. T. Campbell and J. Sauer, *Chem. Rev*., 2013, **113**, 3859-3862.

[19] F. Studt, F. Abild-Pedersen, T. Bligaard, R. Z. Sorensen, C. H. Christensen, J. K. Norskov, *Science*, 2008, **320**, 1320-1322.

[20] J. Hornung, M. Muhr, C. Gemel, R. A. Fischer, *Dalton Trans.*, 2019, **48**, 11743-11748.

[21] H. Zhou, X. Yang, L. Li, Y. Huang, X. Pan, A. Wang, J. Li, T. Zhang, *ACS Catal.*, 2016, **6**, 1054-1061.

[22] M. Miyazaki, S. Furukawa, T. Takayama, S. Yamazoe, T. Komatsu, *ACS Appl. Nano Mater*., 2019, **2**, 3307-3314.

[23] M. D. Segall, P. J. D. Lindan, M. J. Probert, C. J. Pickard, P. J. Hasnip, S. J. Clark, M. C.Payne, *J. Phys. Condens. Matter* 2002, **14**, 2717–2744.

[24] D. Vanderbilt, *Phys. Rev. B* 1990, **41**, 7892–7895.

[25] B. Hammer, L. B. Hansen, J. K. Norskov, *Phys. Rev. B* 1999, **59**, 7413–7421.

[26] H. J. Monkhorst, J. D. Pack, *Phys. Rev. B* 1976, **13**, 5188–5192.

[27] B. Delley, *J. Chem. Phys.* 1990, **92**, 508–517.

[28] Y. Inada, H. Orita, *J. Comput. Chem.* 2008, **29**, 225–232.

[29] B. Delley, *Phys. Rev. B* 2002, **66**, 155125.

[30] G. Kresse, J. Furthmuller, *Phys. Rev. B* 1996, **54**, 11169–11186.

[31] D. Scarano, S. Bordiga, C. Lamberti, G. Spoto, G. Ricchiardi, A. Zecchina, C. O. Arean, *Surf.Sci.* 1998, **411**, 272–285.

[32] J. van de Loosdrecht, A. M. van der Kraan, A. J. van Dillen, J. W. Geus, *Journal of Catalysis*, 1997, **170**, 217-226.

[33] Z. Pan, R. Wang, J. Chen, *Appl. Cat. B: Environmental*, 2018, **224**, 88-100.

[34] X. Meng, L. Wang, L. Chen, M. Xu, N. Liu, J. Zhang, Y. Yang, M. Wei, *J. Catal.*, 2020, **392**, 69-79.

[35] S. Zhou, L. Kang, X. Zhou, Z. Xu, M. Zhu, *Nanomaterials*, 2020, **10**, 509.

[36] G. Xian, P. Xiao, Y. Liu, A. Wang, Y. Su, L. Li, T. Zhang, *Appl. Catal. A: Gen.*, 2017, **545**, 90–96.

[37] T. Komatsu, K. Sou, K. Ozawa, *J. Mol. Catal. A: Chem.*, 2010, **319**, 71–77.

[38] Y. Cao, H. Zhang, S. Ji, Z. Sui, Z. Jiang, D. Wang, Y. Li, *Angew. Chem. Int. Ed.*, 2020, **132**, 11744–11749.

[39] Y. Liu, X. Liu, Q. Feng, D. He, L. Zhang, C. Lian, R. Shen, G. Zhao, Y. Ji, D. Wang, G. Zhou, Y. Li, *Adv. Mater.*, 2016, **28**, 4747–4754.

[40] J. Zhao, L. He, J. Yu, Y. Shi, R. Miao, Q. Guan. P. Ning, *New J. Chem.*, 2021, **45**, 1054–1062.

[41] C. Riley , A. D. La Riva , S. Zhou , Q. Wan , E. J. Peterson , K. Artyushkova , M. D. Farahani , H. B. Friedrich , L. K. Burkemper and N. Atudorei , *ChemCatChem*, 2019, **11** , 1526–1533.

[42] Y. Chen, J. Chen, *Appl. Surf. Sci.*, 2016, **387**, 16-27.

[43] Y. Chai, G. Wu, X. Liu, Y. Ren, W. Dai, C. Wang, Z. Xie, N. Guan, L. Li, *J. Am. Chem. Soc.*2019, **141**, 9920–992.

[44] X. Dai, Z. Chen, T. Yao, L. Zheng, Y. Lin, W. Liu, H. Ju, J. Zhu, X. Hong, S. Wei, Y. Wu and Y. Li, *Chem. Commun.*, 2017, **53**, 11568–11571.

[45] R. Li, X. Ren, X. Feng, X. Li, C. Hu, B. Wang, *Chem. Commun.*, 2014, **50**, 6894-6897.

Chapter Five

Co-modification improves the stability of In_2O_3 catalyst in acetylene semi-hydrogenation

5.1 Introduction

Selective hydrogenation of the trace amount of acetylene in crude ethylene is an important process for polyethylene production in petrochemical industry.[124]) The concentration of acetylene must be decreased to a ppb level by hydrogenation because the polymerization catalyst is fatally poisoned even by a ppm level contamination of acetylene.[125]) Pd-based catalysts have been widely used for acetylene semi-hydrogenation.[71,72]) However, the use of noble metals has been raised the cost in industrial application. Therefore, attention has been placed on developing non-noble-metal catalysts. Bulk indium oxide (In_2O_3) has been known as a noble-metal-alternative catalyst for acetylene semi-hydrogenation.[29]) For higher efficiency, an ideal form should be nanoparticulate In_2O_3 stabilized on an oxide support with high surface area. Moreover, decorating the nanosized In_2O_3 with an appropriate metallic species may provide further enhancement in catalytic performance due to the modification of In_2O_3's property or bifunctional catalysis of the metal and In_2O_3.[126]) Motivated by this catalyst design concept, we tried to synthesize metal-In_2O_3 co-loaded silica catalyst for acetylene semi-hydrogenation. During the course of our attempt to develop the M/In_2O_3/SiO_2 catalysts, we discovered that Co modification significantly improved the catalytic performance of In_2O_3/SiO_2 in acetylene semi-hydrogenation. Interestingly, monometallic Co/SiO_2 showed little activity in this reaction, suggesting a certain concerted catalysis between Co and In_2O_3. Herein, we report a novel type of catalyst for acetylene semi-hydrogenation.

5.2 Experiment section

5.2.1 Catalysts preparation

In_2O_3/SiO_2 (In: 47 wt%) was prepared by a pore-filling co-impregnation method using silica (CARiACT G–6, Fuji Silysia, S_{BET} = 500 m^2 g^{-1}) as a support. An aqueous solution of $In(NO_3)_3 \cdot nH_2O$ (Furuya Metal Co. Ltd.) was added dropwise to SiO_2 so that the solution just fill the pore of silica. The resulting mixtures were sealed and aged overnight at room temperature. Then, the mixture was transferred to a round-bottom flask and frozen in liquid nitrogen and dried in a vacuum at ca. −5°C. Thereafter, the sample was dried overnight in an oven at 90°C, followed by calcination in air at 500 °C for 1 h.

Co/SiO_2 and $Co/In_2O_3/SiO_2$ (Co: 0.5 wt%) catalysts were prepared by a conventional impregnation method. An aqueous solution of $Co(NO_3)_3 \cdot 6H_2O$ (Wako, 98%) was added dropwise to SiO_2 or In_2O_3/SiO_2 and dried at 90 °C overnight, followed by calcination in air at 500 °C for 1 h. For the reduced catalyst, the as-calcined catalyst was treated under flowing hydrogen (20 mL min^{-1}) at 200°C, 250°C, or 600°C for 0.5 h.

5.2.2 Characterization

The XRD patterns of the catalysts were acquired by a MiniFlex 700+D/teX Ultra instrument using a Cu Kα X-ray source. H_2-TPR was conducted using BELCAT II (MicrostracBel). First, 30 mg of the as-calcined catalyst was pretreated under Ar flow (20 mL min^{-1}) at 200 °C for 30 min to remove adsorbed H_2O, then cooled to 100°C. The reduction was performed from 100 °C to 800 °C at a ramping rate of 2°C min^{-1} under flowing 5% H_2/Ar (20 mL min^{-1}). To quantify H_2 consumption, a thermal conductivity detector (TCD) placed downstream in the apparatus was used.

5.2.3 Characterization

Acetylene semi-hydrogenation was performed in a fixed-bed reactor with a 6 mm internal diameter at atmospheric pressure. The catalyst (100 mg) was diluted with quartz sand (total 2.0 g) and introduced into a quartz tube reactor. First, the catalyst was pretreated under flowing H_2 (20 mL min^{-1}) at a certain temperature for 0.5 h and cooled to 30°C under flowing He (20 mL min^{-1}) prior to the catalytic reaction. Then, the catalytic reaction was conducted by feeding the reactant gas mixture (C_2H_2:H_2: He = 2:20:10 mL min^{-1}) into the reactor at certain temperature. The outlet gas was analyzed and quantified using an online gas chromatograph (Shimadzu GC-8A with a column of Unipak S, GL Science) equipped with a TCD detector.

5.3 Results

In_2O_3/SiO_2 was prepared by a pore-filling impregnation method (see Experimental section). The X-ray diffraction (XRD) patter of the as prepared In_2O_3/SiO_2 (Figure 5.1, top) showed broad peaks assignable to cubic In_2O_3 (space group: Ia-3).[127]) The crystallite size estimated by Scherrer's equation was 11 nm, indicating that nanoparticulate In_2O_3 was formed on the surface

of SiO_2. First, we tested the structural property of In_2O_3 under a reducing atmosphere to understand its structural change under the condition of acetylene semi-hydrogenation. Figure 5.1 shows the changes in the XRD patterns of In_2O_3/SiO_2 under H_2 flow at elevated temperature. Metallic indium (space group: I4/mmm)[128]) appeared from 300°C, then dominated at 500°C, indicating stepwise reduction of In_2O_3 to In. At an intermediate temperature (370°C), In_2O_3 and In were observed with low intensities. This suggests that In_2O_3 was partially reduced with low crystallinity at this temperature. A recent study[29]) has reported that partial reduction of In_2O_3 is necessary to construct the active site of acetylene semi-hydrogenation, in which oxygen vacancy, In trimer, and oxygen atoms are adjacent. Therefore, we chose 370°C as the reaction temperature for acetylene semi-hydrogenation.

Next, we tested the catalytic performance of In_2O_3/SiO_2 with different pretreat conditions in acetylene semi-hydrogenation. In_2O_3/SiO_2 reduced at 370°C showed high initial C_2H_2 conversion (ca. 90%) and C_2H_4 selectivity (80%), followed by gradual decrease in the catalytic performance (Figure 5.2). Unreduced In_2O_3/SiO_2 showed a similar trend in the catalytic performance with that reduced at 370°C. This result indicates that In_2O_3 is immediately reduced to the partially reduced state also in the condition of acetylene semi-hydrogenation. Conversely, In_2O_3/SiO_2 reduced at 500°C did not show activity for hydrogenation at all, suggesting that excess reduction is fatal for catalytic hydrogenation of acetylene. Thus, the catalytic performance of In_2O_3 depended on the pretreat condition and the resulting oxidation state. However, the insufficient catalyst stability should be improved in view of practical application. Therefore, we then modified the In_2O_3/SiO_2 catalyst with a non-noble transition metal. In this paper, we show the results of Co-decoration because of catalyst survey. $Co/In_2O_3/SiO_2$ (Co: 0.5 wt%) was prepared by a conventional impregnation method using a Co nitrate solution and In_2O_3/SiO_2. The XRD pattern of the prepared $Co/In_2O_3/SiO_2$ showed a small broad peak assignable to metallic Co at 43.6° (fcc Co),[129]) indicating the formation of small Co nanoparticles on In_2O_3/SiO_2 (Figure 5.3). We also prepared Co/SiO_2 (Co: 0.5 wt%) as a control catalyst in a similar manner to that for $Co/In_2O_3/SiO_2$. Then, the catalytic performance of In_2O_3/SiO_2, $Co/In_2O_3/SiO_2$, and Co/SiO_2 was tested in acetylene semi-hydrogenation. As shown in Figure 5.4, $Co/In_2O_3/SiO_2$ retained acetylene conversion and ethylene selectivity at

least for 120 min unlike In_2O_3/SiO_2, indicating that the catalyst stability was significantly improved by Co loading. Conversely, Co/SiO_2 showed very low acetylene conversion with high ethylene selectivity. These results suggest that Co itself does not work as a main active species, but Co inhibits some side reactions forming poisonous species such as green oil. We also investigated the effect of reduction temperature on the catalytic performance of $Co/In_2O_3/SiO_2$. The catalyst reduced at 200°C and unreduced catalyst showed gradual deactivation, whereas that reduced at 250°C did not (Figure 5.5). This implies that (1) the reduction of Co is necessary for higher stability and (2) the Co can be reduced by H_2 alone (pretreatment) but cannot in the presence of acetylene (under the reaction condition: 370°C), probably due to strong adsorption of acetylene on the Co species. However, when the catalyst was reduced at 600°C, rapid deactivation occurred at the beginning of the reaction. The XRD pattern showed that In_2O_3 was partially transformed to metallic In (Figure 5.6). Therefore, the pretreatment temperature should not be too high to retain the cationic state of In. We also performed temperature-programmed reduction of the unreduced catalysts to understand the redox property of Co and In_2O_3 (Figure 5.7). For In_2O_3/SiO_2, small shoulder and an intense peak were observed at 200°C and 600–800°C, which are assignable to partial reduction of In_2O_3 to $In_2O_{3-\delta}$[130] and the further reduction to metallic In,[131] respectively. Co/SiO_2 showed a small peak at 300–400°C, which can be assigned to reduction of Co^{2+} to $Co^{(0)}$.[132] The corresponding reduction peak could be observed at 250–300°C for $Co/In_2O_3/SiO_2$, indicating that (1) the reduction of Co^{2+} was promoted in the presence of In_2O_3 and (2) Co species can be reduced by H_2 at 250°C and higher. These results are consistent with the trends in XRD patterns and the catalytic reaction.

Finally, we tested a series of $Co/In_2O_3/SiO_2$ with different Co content (0.1, 0.5, and 1.0 wt%). As shown in Figure 5.8, the catalyst with 0.1 wt% Co loading showed catalyst deactivation as observed for In_2O_3, suggesting that the amount of Co was not sufficient to successfully inhibit the undesired side reactions. Conversely, that with 1.0 wt% Co loading showed a similar trend in catalytic performance to that with 0.5 wt% loading. Therefore, we concluded that 0.5 wt% loading of Co is sufficient for enhanced catalysis.

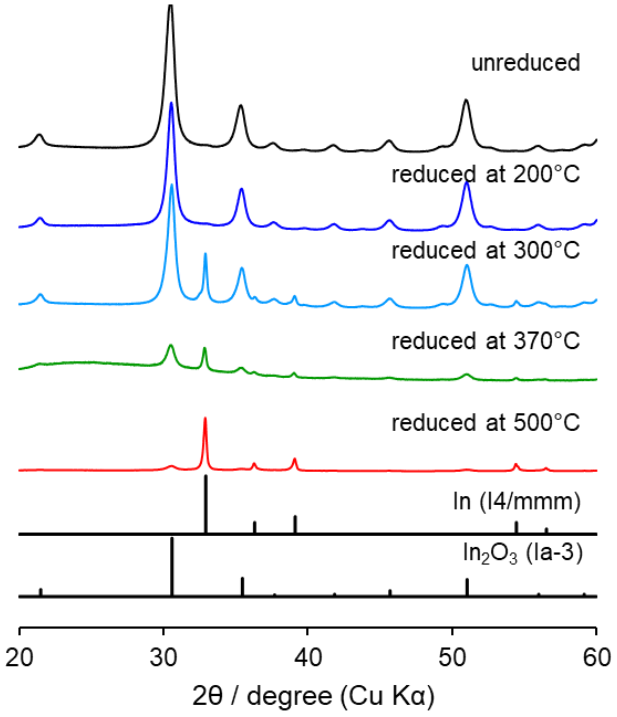

Figure 5.1 XRD patterns of In_2O_3/SiO_2 with and without H_2 reduction at various temperature.

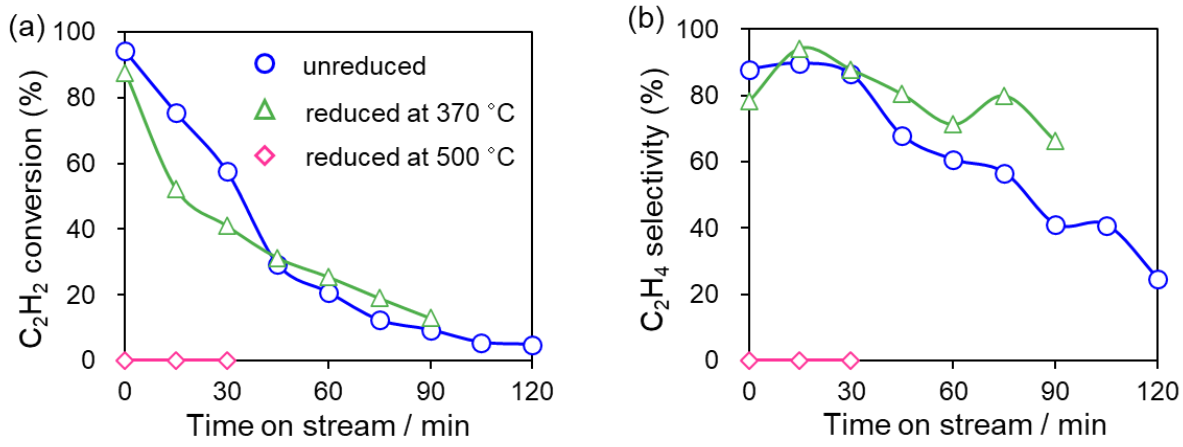

Figure 5.2. Changes in (a) acetylene conversion and (b) ethylene selectivity in acetylene semi-hydrogenation (reaction condition: 370°C, C_2H_2:H_2:He = 2:20:10 mLmin^{-1}) over In_2O_3/SiO_2 catalysts with and without H_2 reduction.

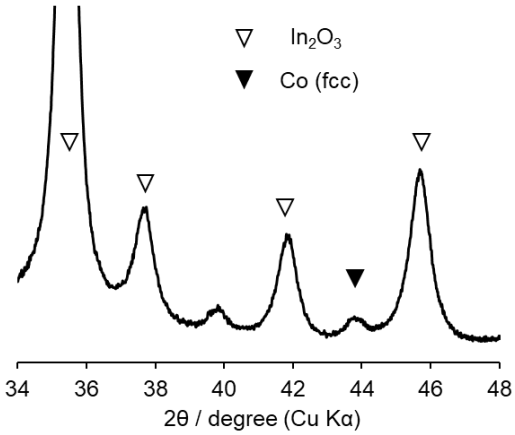

Figure 5.3. XRD patterns of $Co/In_2O_3/SiO_2$ reduced at 250°C.

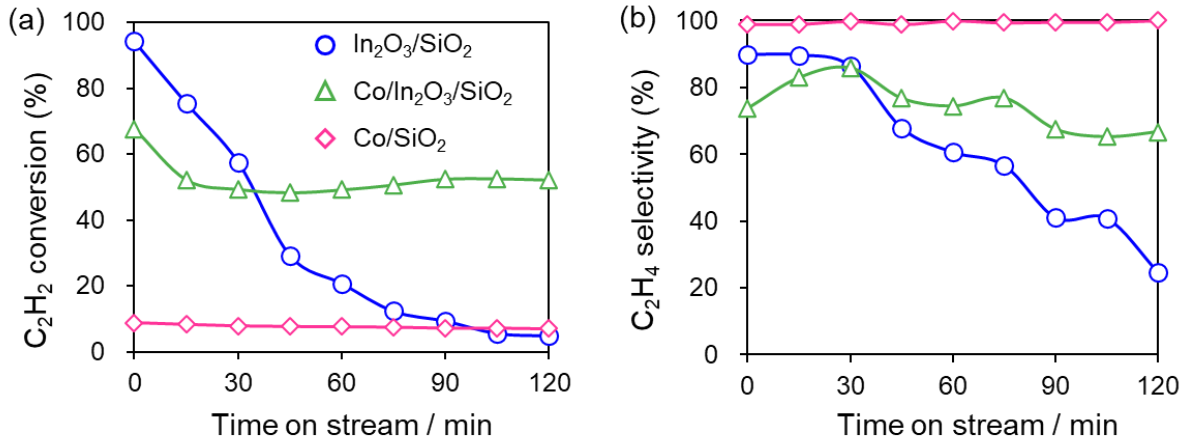

Figure 5.4. Changes in (a) acetylene conversion and (b) ethylene selectivity in acetylene semi-hydrogenation (reaction condition: 370°C, C_2H_2:H_2:He = 2:20:10 $mLmin^{-1}$) over In_2O_3/SiO_2, $Co/In_2O_3/SiO_2$, and Co/SiO_2 catalysts with and without H_2 reduction. Co-based catalysts (Co: 0.5 wt%) were pretreated by H_2 at 250°C for 0.5 h.

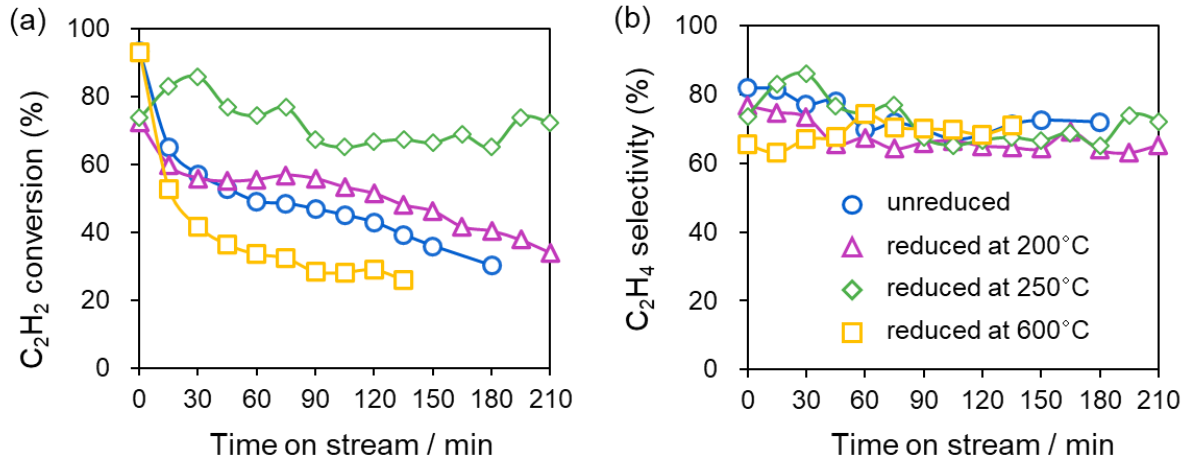

Figure 5.5. Changes in (a) acetylene conversion and (b) ethylene selectivity in acetylene semi-hydrogenation (reaction condition: 370°C, C_2H_2:H_2:He = 2:20:10 $mLmin^{-1}$) over

$Co/In_2O_3/SiO_2$ catalysts with and without H_2 reduction at various temperature.

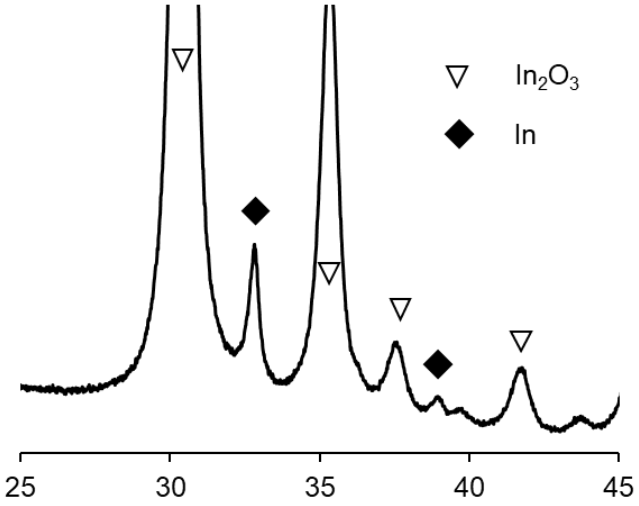

Figure 5.6. XRD patterns of $Co/In_2O_3/SiO_2$ reduced at 600°C.

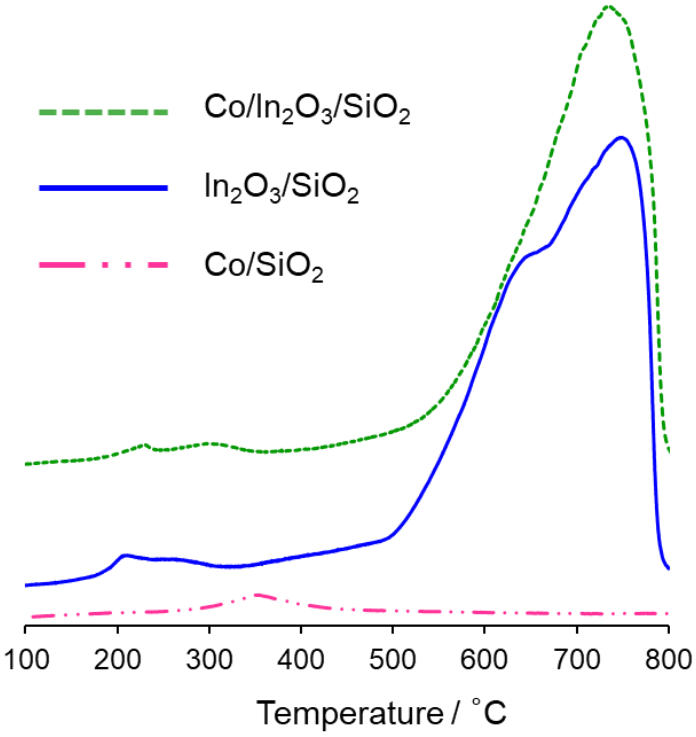

Figure 5.7. H_2-TPR profiles of $Co/In_2O_3/SiO_2$, In_2O_3/SiO_2, and Co/SiO_2.

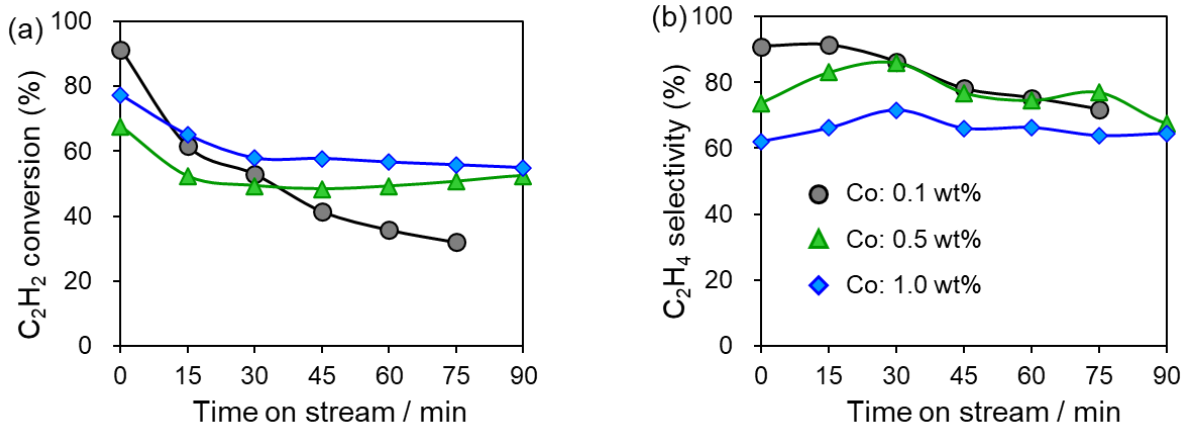

Figure 5.8. Changes in (a) acetylene conversion and (b) ethylene selectivity in acetylene semi-hydrogenation (reaction condition: 370°C, C_2H_2:H_2:He = 2:20:10 mLmin^{-1}) over Co/In_2O_3/SiO_2 catalysts with different Co loadings (pretreated by H_2 at 250° C for 0.5 h).

5.4 Discussion

In this study, we prepared a series of Co/In_2O_3/SiO_2 catalysts as noble-metal alternative materials for acetylene semi-hydrogenation. Although nanoparticulate In_2O_3 supported on silica (In_2O_3/SiO_2) acts as a catalyst for acetylene semi-hydrogenation, the catalytic performance decreases with time probably due to the formation of poisonous species by side reactions. Decorating In_2O_3/SiO_2 with a small amount of Co with H_2 pretreatment at appropriate temperature allows drastically increase the stability in acetylene semi-hydrogenation. Metallic Co may inhibit undesired side reactions that generate poisonous species to the catalyst.

References

[1] Wang, Y.; Wang, B.; Ling, L.; Zhang, R.; Fan, M. *Chem. Eng. Sci.*, **218**, (218), 115549 (2020).

[2] Kang, J. H.; Shin, E. W.; Kim, W. J.; Park, J. D.; Moon, S. H, *Catal. Today*, **63**, (2-4), 183 (2000).

[3] Armbrüster, M.; Kovnir, K.; Behrens, M.; Teschner, D.; Grin, Y.; Schlögl, R, *J. Am. Chem. Soc.*, **132**, (42), 14745 (2010).

[4] Pei, G. X.; Liu, X. Y.; Wang, A.; Lee, A. F.; Isaacs, M. A.; Li, L.; Pan, X.; Yang, X.; Wang,

X.; Tai, Z.; Wilson, K.; Zhang, T, *ACS Catal.*, **5**, (6), 3717 (2015).

[5] Albani, D.; Capdevila-Cortada, M.; Vilé, G.; Mitchell, S.; Martin, O.; López, N.; Pérez-Ramírez, J. *Angew. Chem. Int. Ed.*, **56**, (36), 10755 (2017).

[6] Furukawa, S.; Endo, M.; Komatsu, T, *ACS Catal.*, **4**, (10), 3533 (2014).

[7] Heald, S.; Alshammari, M. S.; Alfehaid, S.; Alotaibi, M.; Feng, Q.; Hakimi, A. M. H. R, *J. Phys.: Conf. Ser.*, **430**, (1), (2013).

[8] Wołcyrz, M.; Kubiak, R.; Maciejewski, S, *Phys. Stat. Solid. (B)*, **107**, (1), (1981).

[9] Singh, M.; Barkei, M.; Inden, G.; Bhan, S, *Phys. Stat. Solid.*, **87**, (1), 165 (1985).

[10]Martin, O.; Martín, A. J.; Mondelli, C.; Mitchell, S.; Segawa, T. F.; Hauert, R.; Drouilly, C.; Curulla-Ferré, D.; Pérez-Ramírez, J, *Angew. Chem. Int. Ed*, **55**, (21), 6261 (2016).

[11]Naberezhnyi, D.; Rumyantseva, M.; Filatova, D.; Batuk, M.; Hadermann, J.; Baranchikov, A.; Khmelevsky, N.; Aksenenko, A.; Konstantinova, E.; Gaskov, A, *Nanomaterials*, **8**, (10), 801 (2018).

[12]Li, X.; Nisa, M. U.; Chen, Y.; Li, Z, *Ind. Eng. Chem. Res.*, **58**, (8), 3459 (2019).

Chapter Six

General Conclusion

In this research, I focused on the development of highly efficient catalysts for acetylene semi-hydrogenation based on multinary non-noble alloys. To this end,

Chapter 2 concludes that HEI, where the Ni and Ga sites were partially substituted with Fe/Cu and Ge, respectively, exhibited excellent selectivity towards ethylene (97%) even at complete acetylene conversion, without altering the parent NiGa CsCl-type structure. The significant improvement of catalytic activity is related to the lower energy barrier of acetylene hydrogenation and facilitated the adsorption/activation of hydrogen. The drastic enhancement of ethylene selectivity can be attributed to the reduction in the surface energy of the most stable (110) plane resulting from surface relaxation, which remarkably promoted ethylene desorption. Thus, the NiFeCuGaGe/SiO_2 HEI catalyst completely exhibited five-times higher activity than other 3d-transition-metal-based catalysts. Furthermore, the role of multi-metallization in the enhancement was attributed to geometric effects rather than an electronic effect. This is the first report of the complete inhibition of ethylene over-hydrogenation, developing a highly efficient catalyst for semi-hydrogenation. Moreover, this is also the first time that HEI was applied to thermocatalysis so it provides novel design concept for other catalytic systems.

Chapter 3 reveals a fine-tuning pseudo-binary alloy for acetylene semi-hydrogenation, in which, Ni_3Ga and Cu as the parent intermetallic structure and the third element for active site tuning, respectively. The best catalyst $(Ni_{0.8}Cu_{0.2})_3Ga/TiO_2$ was obtained through optimizing the Cu contents, which exhibited outstandingly high catalytic activity among reported 3d transition metal-based systems (1250 $mL_{C_2H_2}{}^{-1}min^{-1}g^{-1}$), excellent ethylene selectivity (96%), and long-term stability (100 h) with almost full conversion even at 150°C. The improvement in catalytic activity was assigned to the low energy barrier of acetylene hydrogenation, which was highly associated with enormous destabilization of the multifold coordination of adsorbates which resulted from the formation Ni_2Cu hollow sites on the stable Ni_3Ga (111) surface when an appropriate amount of Cu was doped. Furthermore, the adsorption of acetylene was weakened so the hydrogenation process by increasing hydrogen coverage was further accelerated. Meanwhile, the ethylene selectivity was improved due to the direct hydrogenation pathway via the ethylidene intermediate. Thus, our goal of obtaining an active catalyst at low

temperature without lowering the ethylene selectivity was achieved, providing fresh insights into the precise tuning of catalytic performance to achieve defined properties.

Chapter 4 proposes that Ni–Zn alloy nanoparticles on SiO_2, further decorated with additional silica, can significantly increase the acetylene conversion (15%–97%) without lowering ethylene selectivity (ca. 80%) at 200°C. The drastic improvement in the handling capacity may be due to the increase in the number of active sites (probably, step sites) induced by silica modification. The high selectivity may originate from the geometric effect of the step sites. Besides, hydrogen attack to C_2H_4 at the step site was more likely to be inhibited than that to C_2H_2. Thus, the high activity and geometric restriction of the step site allowed the highly active and selective semi-hydrogenation of acetylene.

Chapter 5 presents a strategy to modify the catalytic performance. In_2O_3/SiO_2 decorated with a small amount of Co at a suitable H_2 pretreatment temperature, greatly increased the stability in acetylene semi-hydrogenation. A possible reason is that metallic Co may suppress undesirable side reactions in which products poisoned the catalysts. There is no doubt, this work verified the possibility of efficient acetylene hydrogenation metal oxide catalysts modified by metal doping, which brings new ideas for metal oxide modification for superior performance and offers further possibilities for the application of metal oxides in catalytic reaction systems.

To summarize, our work not only demonstrates non-noble catalysts with excellent acetylene semi-hydrogenation catalytic performance, but also opens a new window for the design of multi-metallic catalysts. Additionally, it greatly accelerated the further understanding of multi-metallic catalysts and their catalytic mechanisms. Meanwhile, it is a further step forward for non-noble metals from theory to practical application.

Acknowledgments

I would like to acknowledge the Hokkaido University Ambitious Doctoral Fellowship and Japan Society for the Promotion of Science for giving the precious opportunity and financial support for me to gain PhD degree in Institute for Catalysis, Faculty of Chemical Science and Engineering.

Firstly, I would like to express gratitude to my supervisor Professor Shinya Furukawa for supervising and supporting my research so that I can make great process. He not only imparted knowledge but also serves as a paragon, demonstrating the attitude of a true scientist. Meanwhile, he is a very humanitarian scientist. I really admire his ambition and dedication to scientific research. I think he has always been a role model for me on the road of scientific research.

In addition, I would like to thank Professor Shimizu for his help and support in my research. He is a person of extraordinary intelligence, and he is a very tolerant person. His enthusiasm and dedication to research always inspired me.

I am truly grateful to all the staff and members in Shimizu lab for their kind support. I would also like to thank the advisory committee members for their suggestions.

Last, but not means the least, I would like to thank my parents, my family members and all my friends who gave me a lot of support and help.

Wish you all the best!

Ma Jiamin

2023.06.09